Euler-Lagrange Modeling of Vortex Interaction with a Particle-Laden Turbulent Boundary Layer

by

Fernando Morales

A Thesis Presented in Partial Fulfillment
of the Requirements for the Degree
Master of Science

Approved May 2011 by the
Graduate Supervisory Committee:

Kyle D. Squires, Chair
Valana L. Wells
Ronald J. Calhoun

ARIZONA STATE UNIVERSITY

May 2011

ABSTRACT

Rotorcraft operation in austere environments can result in difficult operating conditions, particularly in the vicinity of sandy areas. The uplift of sediment by rotorcraft downwash, a phenomenon known as brownout, hinders pilot visual cues and may result in a potentially dangerous situation. Brownout is a complex multi-phase flow problem that is not unique and depends on both the characteristics of the rotorcraft and the sediment. The lack of fundamental understanding constrains models and limits development of technologies that could mitigate the adverse effects of brownout. This provides the over-arching motivation of the current work focusing on models of particle-laden sediment beds. The particular focus of the current investigations is numerical modeling of near-surface fluid-particle interactions in turbulent boundary layers with and without coherent vortices superimposed on the background flow, that model rotorcraft downwash. The simulations are performed with two groups of particles having different densities both of which display strong vortex-particle interaction close to the source location. The simulations include cases with inter-particle collisions and gravitational settling. Particle effects on the fluid are ignored. The numerical simulations are performed using an Euler-Lagrange method in which a fractional-step approach is used for the fluid and with the particulate phase advanced using Discrete Particle Simulation. The objectives are to gain insight into the fluid-particle dynamics that influence transport near the bed by analyzing the competing effects of the vortices, inter-particle collisions, and

gravity. Following the introduction of coherent vortices into the domain, the structures convect downstream, dissipate, and then recover to an equilibrium state with the boundary layer. The particle phase displays an analogous return to an equilibrium state as the vortices dissipate and the boundary layer recovers, though this recovery is slower than for the fluid and is sensitive to the particle response time. The effects of inter-particle collisions are relatively strong and apparent throughout the flow, being most effective in the boundary layer. Gravitational settling increases the particle concentration near the wall and consequently increase inter-particle collisions.

DEDICATION

Everything I have accomplished is due to the love and support of my family.

ACKNOWLEDGMENTS

I would like to thank Dr. Squires for the guidance provided throughout the completion of the thesis. I would also like to extend my gratitude to Dr. Vance for providing valuable knowledge on the inner workings of the simulation. Furthermore I would like to thank Dr. Piomelli and Dr. Naqavi for providing the flow solver for the simulation.

TABLE OF CONTENTS

LIST OF TABLES

LIST OF FIGURES

NOMENCLATURE

$\langle . \rangle^+$	indicates property in viscous units
$\langle . \rangle^c$	indicates collision property
$\langle . \rangle_f$	indicates fluid property
$\langle . \rangle_p$	indicates particle property
$\overline{\langle . \rangle}$	indicates nondimensional property
A_f	amplitude factor for desired vortex circulation
a_1, a_2	parameters to construct the radius of the vortex
C_D	coefficient of drag
d_p	particle diameter
f_i	body force used to introduce vortices into the flow
g	acceleration due to gravity
h_p	constraint for wall-normal position of particles
i, j	represent Cartesian coordiantes
k	relative distance between particles
L_y	length of domain in wall-normal dimension
M_{frac}	particle mass fraction
N_b	number of particles per bin
N_p	number of particles per group
N_s	number of times particle statistics have been sampled
N_y	number of segments along wall-normal direction
N_{procs}	number of processors
n_D	average number density
n_I	instantaneous number density
p	pressure

Re	fluid Reynolds number
Re_Γ	circulation Reynolds number
Re_p	particle Reynolds number
r	radius of vortex
r_1	radius of vortex during peak velocity
r_p	radius of particle
St	Stokes number
t	time
U_∞	free stream velocity
$\langle u_i' u_i' \rangle$	fluid root mean square velocity
$\langle u_i' v_j' \rangle$	fluid-particle correlation
u^*	flow shear velocity
u_f	fluid velocity
$\boldsymbol{V}$	vortex velocity
V_θ	tangential velocity of the vortex
V_{frac}	particle volume fraction
$\boldsymbol{v}_r$	slip velocity magnitude
$\langle v_2' v_2' v_2' \rangle$	particle velocity triple correlation
$\langle v_i' v_i' \rangle$	particle root mean square velocity
$\langle v_i' v_j' \rangle$	particle-particle correlation
v_p	particle velocity
v_r	relative velocity between fluid and particle
w	relative velocity between particles
w_s	particle settling velocity
x, y, z	position in streamwise, wall-normal, and spanwise directions
α	stretching factor for wall-normal grid

Γ	vortex circulation
Δ	difference between two successive grid points
δ	boundary layer thickness
$\delta_i 1$	Kronecker delta
ϵ	kinetic energy dissipation rate
η	Kolmogorov length scale
ν_f	fliud kinematic viscosity
ρ	density ratio, ρ_p/ρ_f
ρ_f	density of the fluid
ρ_p	density of the particle
τ_p	particle relaxition time
τ_w	wall shear stress
τ_{ij}	subgrid scale stresses
Ψ	statistical quantity for individual particle
ψ	mean statistical quantity for a bin

I. Introduction

In recent years the effects of rotorcraft brownout have become an increasingly hazardous byproduct of operating rotorcraft in austere environments. Rotorcraft brownout is the phenomenon that causes intense blinding dust clouds stirred by the helicopter rotor downwash during near-ground operations. The uplifted sediment may come into contact with the rotors and can also be ingested causing significant mechanical damage to rotorcraft components. The U.S. Army has estimated that brownout is responsible for three out of every four accidents involving rotorcraft [4]. These incidents have led to many fatalities and destruction of rotorcraft,

(a) V22 Osprey (b) EH 101 Merlin

Figure 1. Rotorcraft Brownout

and naturally several attempts have been made to decrease the negative impact of brownout. Some recent attempts include Lockheed Martin's Pathfinder, DARPA's Sandblaster, and PhLASH by the U.S. Air Force Research Laboratory. The aforementioned strategies attempt to alleviate brownout by enhancing the visual cues the pilot receives from onboard avionics. Clearly brownout poses a significant

challenge when operating or hovering close to the ground and even though these attempts can provide the pilot with a temporary solution, these strategies fail to provide fundamental insight into the underlying causes of the phenomenon which is known to differ substantially from rotorcraft to rotorcraft. These strategies fail to eradicate or even lessen the development of brownout instead opting to provide the pilot with visual cues of the terrain before the dust cloud evolution completely impedes visibility.

In order to shed some light on the brownout issue, it is necessary to study all the individual aspects that affect the dust cloud formation. At the most basic level the brownout cloud forms through the fluid-particle interactions that develop into a blinding dust cloud. The fluid in this case comes from the downwash created by the rotors operating near the ground. The structures present in the fluid are affected by the physical properties of the rotors such as disk loading, blade loading, number and placement of rotors, number of blades, blade twist, and blade tip shape. In addition to the aforementioned effects the airflow also interacts with the fuselage, the body of the rotorcraft, which may have a significant effect on the development of the brownout cloud. These factors characterize the airflow which proceeds to the ground and interacts with the sediment bed. The size and physical properties of the sediment can have a large role on the brownout evolution of a hovering rotorcraft. There are some clear implications such as smaller particles tend to be uplifted while larger particles roll along the sediment bed, but there are also some other characteristics such as cohesiveness, humidity, and shape whose effects are

not well understood in terms of brownout. It is important to determine which characteristics of the flow field and the particles are most significant to the evolution of the brownout cloud to mitigate this harmful consequence of rotorcraft operation in certain environments.

The brownout problem as a whole encompasses many different areas of interest such as the fundamental aerodynamics of the rotor and fuselage during ground operation as well as the near-surface dynamics of multiphase flow. It is for these reasons that a comprehensive study is necessary to provide insight and possible solutions to brownout that will not only identify the underlying causes but also provide the information to lessen or eradicate this hazardous issue. These diverse features of brownout led to a Multi University Research Initiative (MURI) to study and mitigate the effects of rotorcraft brownout. The MURI consists of collaboration between several institutions including the University of Maryland, Iowa State University, Dartmouth College, and Arizona State University [5]. Each institution is providing expertise in a very specific area to provide fundamental insights into the causes, development, and evolution of brownout through the use of both experimental and computational research. The project is divided into three primary research tasks each of which consists of several research subtasks. The following sections are a brief overview of the research tasks to provide the necessary context required for the present work.

A. Fundamentals of Rotorcraft in Ground Effect Operations

The brownout signature of a rotorcraft is not unique and depends on a number of properties which include both the rotorcraft and the type of sediment over which the rotorcraft is maneuvering. Furthermore the brownout signature of some rotorcraft is less severe than for others which may indicate that some intrinsic properties of the rotorcraft play an important role. Additionally, rotorcraft airloads are affected by ground surfaces and other close obstacles. As the rotors approach solid boundaries the velocities in the rotor flow are changed as shown on Figure 2 and the wake vortices go a through a series of complex interactions as they travel down to the surface [1]. These highly complex interactions can lead to blade tip vortices which may contain peak velocities that are much higher than the average flow velocity below the rotor. Naturally these wake tip vortices with high peak velocities interact with the sediment and ultimately uplift the sediment and form the brownout cloud. There are several key factors which include blade loading, tip shape, tip speed, blade twist amongst others but also the shape of the fuselage and its effect on the developing groundwash may be of importance.

The significance of the rotor on the cause and evolution of brownout is clear, however the significance of the airframe on the development of brownout is not fully understood. It is not known if the airframe of the rotorcraft is of equal consequence in the evolution the brownout cloud. On the other hand, it is known that the fuselage plays an important role in the performance and trim of a rotorcraft which

seems to lend credibility to the fuselage being a significant factor of brownout. In order to quantify the importance of both the rotor and the fuselage collaborators of the MURI are undertaking experimental measurements which include Digital Particle Image Velocimetry (DPIV) as well as Computational Fluid Dynamics (CFD).

B. Fundamentals of Particle Entrainment

The next logical step is to examine the interactions between the wake vortices present in the flow and the sediment bed. The fundamental process of particle suspension is not fully understood and is plagued by high levels of complexity. A sediment bed likely contains a poly-disperse mixture of particles which have several modes of transport. In addition to the multiple modes of transport the sediment also has inter-particle collisions and agglomeration of particles which further increases the difficulty of the problem. It is imperative to improve the understanding of the particle transport process to provide insight into the development and evolution of the brownout phenomena. In practice particle entrainment from uniform flow has

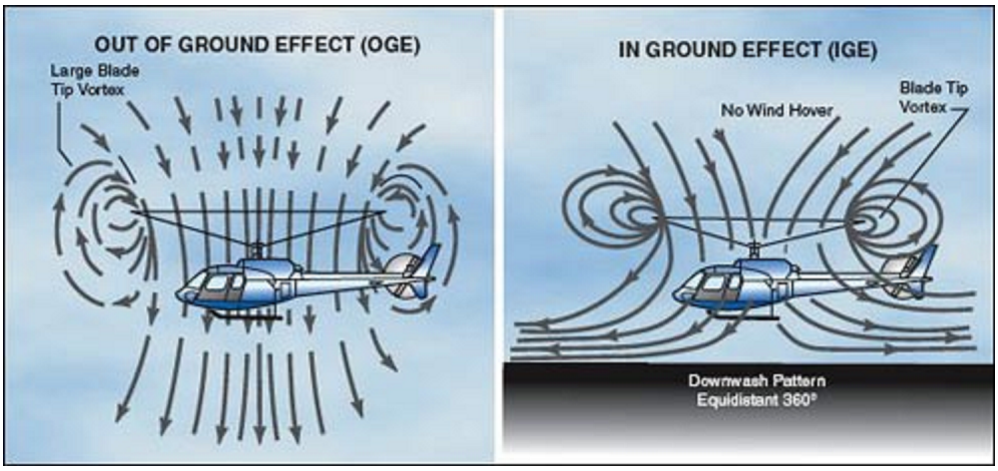

Figure 2. Rotorcraft OGE & IGE

been researched, however non-uniform flows have not received much attention and the entrainment mechanisms between these flows may be distinct, implying the need for further work on entrainment from non-uniform flows.

In order to advance the understanding of particle entrainment it is crucial to correctly asses the entrainment boundary conditions the particles experience when exposed to a rotor flow. However this assessment is complicated by the asymmetric nature of rotorcraft which has not been widely studied. A series of experiments are undertaken as part of the MURI to shed some light on the effect of the unsteady non-uniform flow over a poly-disperse mixture of particles with a particular interest on the cohesiveness of the sediment bed. These experiments are meant to provide the necessary conditions for the CFD simulations that aim to recreate the near-surface fluid-particle interactions. In addition to the proper boundary conditions, the CFD simulations also require a reliable and robust rotor wake model which can accurately predict the motion of the blade tip vortices. Furthermore a particle tracking model which incorporates a particulate uplift model that dictates how particles are entrained by the impinging vortices is also necessary. The development of these models depends on the increased understanding and insight into the fundamental process of particle entrainment from a sediment bed.

C. Objective of Thesis

The underlying physics leading to rotorcraft brownout are not yet fully understood. The driving principles of the fluid-particle interactions that lead to the evo-

lution of the dust cloud have not been extensively studied. Few simulations and experiments have been conducted on this particular issue plaguing rotorcraft. Even though many factors are involved in the process of rotorcraft brownout, a first principles approach to further the canonical knowledge of the two-fluid interaction near the sediment bed is of great significance in characterizing and recognizing the most significant elements governing brownout. To advance the understanding of the fundamental processes that inevitably lead to the formation of the dust cloud, a set of simulations was developed to study the near-surface two-phase interaction. The simulations are aimed at isolating and characterizing the competing effects of inter-particle collisions and vortex-particle interactions near the ground.

The focus of the current investigations is numerical modeling of fluid-particle interaction in turbulent boundary layers with and without coherent vortices superimposed on the background flow. Simulations are performed using an Euler-Lagrange method in which a fractional-step approach is used for the fluid and with the particulate phase advanced using Discrete Particle Simulation(DPS). The fluid phase employs a Direct Numerical Simulation(DNS) that resolves even the smallest scale turbulence on the grid. Even though simulations without turbulence models are more computationally expensive, through DNS the subgrid scale turbulence is solved directly and the understanding of the flow can be applied to develop more refined Large Eddy Simulation models to further the understanding of the fluid-particle interactions. For the particulate phase the individual motion of a particle is computed by numerically integrating the equation of motion for a small sphere

exposed to an unsteady and non-uniform flow field.

The first flow field models a rotor wake comprised of gradually introduced coherent vortices into a turbulent boundary layer. The second flow is a turbulent boundary layer without vortices to segregate and characterize the effect of the vortex structures on the dispersed phase properties. Both flows are shown in Figure (3), the turbulent boundary layer with and without the vortices. The simulations are performed with two groups of particles having different densities both of which display strong vortex-particle interaction close to the source location, and mixing of the particles into the boundary layer downstream. These simulations will be compared to isolate the effects from particle-particle collisions as well as the vortex effects. In addition, a subset of the simulations is exposed to a gravitational force acting on the particles. The gravitational term is enforced as a particle settling velocity that drives the particles toward the lower wall. In essence, the simulations contain two different particle groups, two different flow fields, particle-particle collisions, as well as simulations with and without a gravitational term.

The objectives are to gain insight into the fluid-particle dynamics that influence transport near the bed by analyzing the competing effects of the vortices, inter-particle collisions, and the gravitational force on the particles. It is important to determine where and which features of the flow and the particles are dominant in the mixing and transport of the particles to and from the wall. Another objective is to advance the understanding of the mesoscopic particle velocity field. This objective requires very large particle ensembles in order to recover an Eulerian description

of the particle field. Visualizations and statistical descriptors presented quantify the effect of the coherent vortex structures, inter-particle collisions, and the inclusion of a gravity force on the dispersed phase properties.

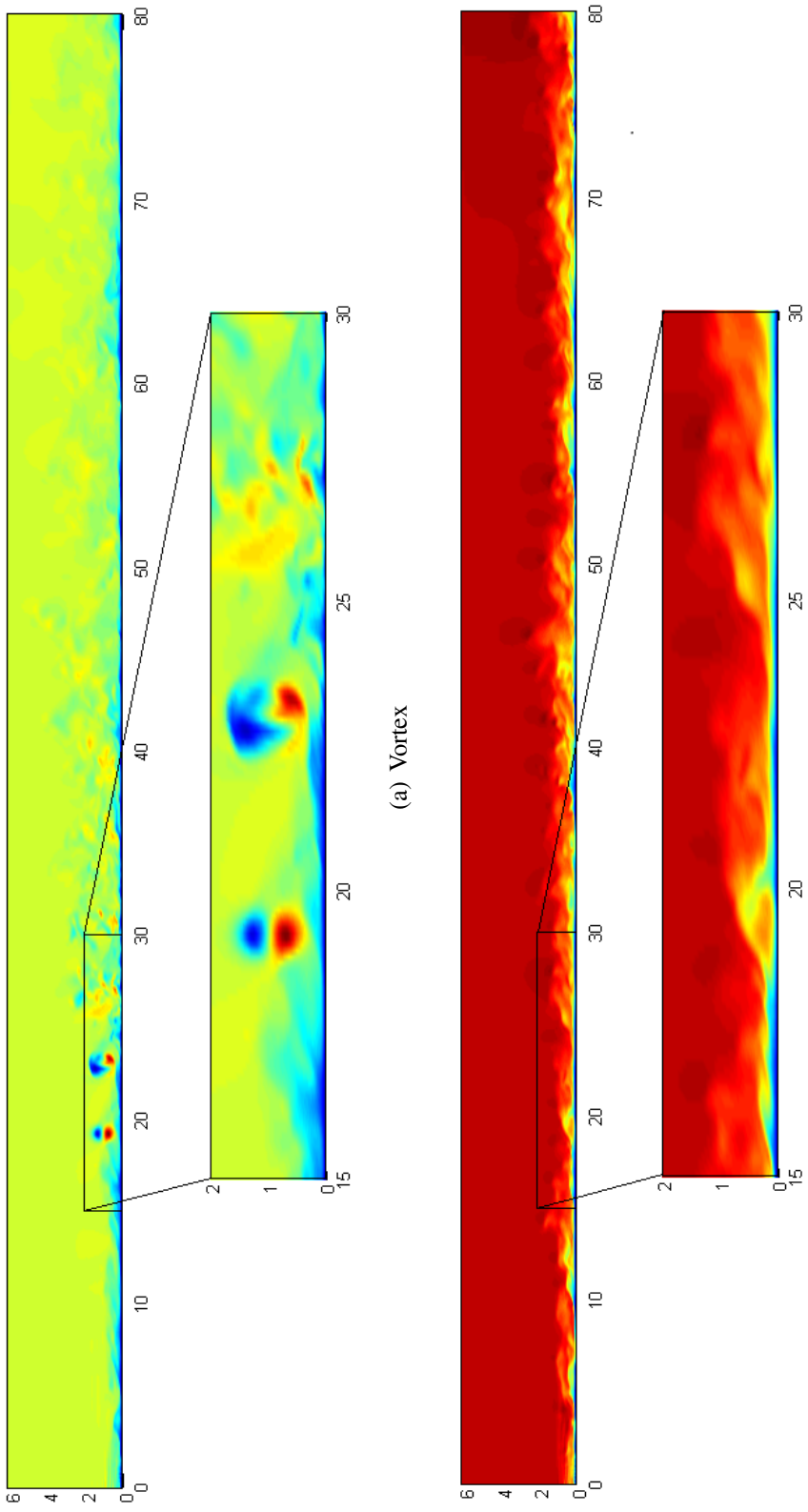

(a) Vortex

(b) Turbulent Boundary Layer

Figure 3. Streamwise velocity contours for both flows

II. Background

This section details information on previous experiments and simulations, as well as details on the idealized rotor flow and sediment transport. In general, the primary technical challenges can be divided into those residing at the microscale and the mesoscale. Specific technical challenges include simulation or measurement of the detailed processes of particle lift-off from a sediment bed, the role of turbulence influencing dispersed-phase transport, particle-particle interactions, and the influence of particle momentum exchange on properties of the carrier phase turbulent flow. Brownout measurements on full size rotorcraft are limited given the scale and complexity of the components involved. Nevertheless, several experiments have been performed on sub-scale rotors, usually ignoring the fuselage, to shed light on the two-phase dynamics. In addition to the experiments, several simulations have also been performed albeit with a number of simplifications. Specifically, the intricacies of the rotor flow and the momentum exchange between the two phases are simplified in the numerical models. On the other hand sediment transport has been studied extensively, unfortunately most studies were conducted under uniform, invariant flow field conditions. Even though non-uniform studies have not been extensive, the vast knowledge obtained from the previous uniform conditions provide an adequate starting point from which more knowledge can be gathered and the simulations continually improved to reflect physical conditions more appropriately.

A. Experiments and Simulations

The previous sections outlined the complexities associated with a rotorcraft experiencing brownout, nevertheless attempts have been made to shed light on the driving mechanisms causing this potentially fatal event. A difficulty surrounding the brownout problem is the lack of experimental data. Clearly, performing measurements on a full scale test is complicated given the size of the physical components, nevertheless Wadcock *et al.* [6] performed measurements on a full size UH-60 Blackhawk, focusing on the downwash characteristics of a UH-60 Blackhawk in relation to particle entrainment and brownout. However, instead of pursuing full scale measurements several researchers have opted to perform laboratory measurements on smaller scale rotor systems. Leishman *et al.* [7] studied two-phase flow using high-speed flow visualization and particle image velocimetry(PIV), in particular the surface and upwash velocities were shown to strengthen significantly with the viscous merging of adjacent wake vortices. Also Johnson [3] presented detailed snapshots of large sediment particles uplifted by the vortical flow which proceed in a modified saltation trajectory and bombard the sediment bed causing finer particulates to suspend onto the medium. Green *et al.* [8] attempted to recreate brownout in a laboratory setting to provide more insight on the issue. The experiment established that the recirculation regime consisted of a region of vorticity, spread over a relatively large distance of the flow along the ground. In addition, the tip vortices were seen to accumulate ahead of the rotor disk, or to be reingested through

the rotor disk. Unfortunately, these experimental measurements utilize small rotors which may suffer scaling issues when compared to the full scale rotorcraft, nevertheless these measurements provide great qualitative insight to the physical underpinnings of the brownout phenomenon as well as providing some guidance to the computer models.

In addition to the sub-scale rotor measurements, several numerical simulations have been undertaken to provide more details on the physical processes of brownout. Eulerian simulations modeling the brownout cloud formations have been explored, however many assumptions and simplifications are necessary to calculate the evolution of the dust cloud. Haehnel *et al.* [9] developed a model to simulate the unsteady flow phenomena that strongly affects particle entrainment. Phillips *et al.* [10, 11] employed a vorticity transport model coupled with a model to represent the entrainment and transport of particulate matter through the flow. These types of large scale numerical models simplify the rotor flow during IGE, as well as the sediment uplift by the rotor downwash, and finally the momentum exchange between the two phases is also simplified. The simplification on the sediment uplift models may prove detrimental to the mitigation effort since these models have only been validated for uniform flow. In subsequent sections the threshold conditions utilized in uplift models for particle transport will be discussed for both uniform and non-uniform flows.

Another approach to numerical simulation of the brownout phenomenon is the Lagrangian method where every particle in the computational domain is tracked in-

dividually while the fluid phase is computed in an Eulerian scheme. Euler-Lagrange two-phase flow numerical simulations of particle transport in turbulent boundary layers have been widely studied. Many numerical simulations have been performed to increase the understanding of particle-turbulence interactions near the wall. An issue plaguing Lagrangian simulations is the possibility of the particle population becoming diffuse and losing accuracy in the computation of statistical quantities. Early simulations considering the particle-turbulence interactions did not include inter-particle collisions [12, 13]. These early investigations demonstrated that dense particles accumulate in certain regions of the flow also known as preferential concentration. Soldati *et al.* [14, 15] have shown that there is a strong correlation between coherent wall structures, particle segregation, and deposition phenomena. Specifically that the particle deposition process is initially dominated by inertia and results in accumulation of particles into specific regions along the walls. Particles tend to accumulate in specific flow regions and remain for extended periods of time. Therefore particles do not fully experience the Eulerian statistics of the turbulent flow field and instead only preferentially sample the flow field [16]. The inclusion of particle-particle interactions strongly influence the particle statistics and visibly reduce the preferential concentration effect [17]. Furthermore the effects of inter-particle collisions are significant even in the dilute regime [18, 19]. More recently, the Lagrangian approach has been employed by [20–22] with modifications to the particulate phase, specifically particle entrainment and transport under non-uniform flow that resemble brownout conditions.

The simulations in this investigation consist of a flow solver that models the downwash of the rotor flow coupled with a particle tracking algorithm that individually follows millions of particles throughout the computational domain. This work employs a Direct Numerical Simulation(DNS) for the fluid phase to resolve even the small scale turbulent structures within the flow. Even though DNS is more computationally expensive than other methods, DNS is chosen to drive the understanding of this type of flow. For the particulate phase a Lagrangian framework is employed with large particle ensembles to capture the motion of the individual particles under the influence of the simulated rotor flow. The focus of the simulations is on the near-surface fluid-particle dynamics, specifically understanding the competing effects of inter-particle collisions and the simulated rotor vortices.

B. Idealized Rotor Flow

In order to gain insight into rotorcraft brownout, a simulation not only requires large particle ensembles but also a model flow that is representative of the non-uniform structures present in rotor downwash impinging on a surface. In earlier sections the complexity and difficulties associated with rotorcraft flow pertaining to brownout were briefly mentioned. In this section the characteristics of the simulated rotor flow and the assumptions are listed. The flow around a helicopter rotor is complex due to the helicoidal blade tip vortex filaments which leads to asymmetric flow [3]. During out of ground operations the induced flow eventually contracts and the vortices diffuse into a turbulent jet. For a rotorcraft operating in ground ef-

fect, the ground becomes a streamline of the flow forcing the downwash to radially expand. The expansion occurs near the surface and is parallel to the ground which makes rotor downwash highly unsteady and three-dimensional. Leishman [1] studied the rotor vortices both IGE and OGE and illustrates the difference in Figures 4 and 5.

Simulating the flow surrounding a rotorcraft without assumptions or simplifications is currently impossible with the current computing capabilities, it is therefore necessary to make assumptions that may distort the problem but will still prove useful in shedding light on the fundamental driving mechanisms. The large scale of the rotorcraft can prove challenging, however, since the main interest of this investigation lies on the near-surface fluid-particle dynamics, the scope of the simulations is limited to near-surface interactions. With this limitation in place several other complexities of the flow are also avoided, including the rotor and fuselage effects on the downwash. The focus of the project is not on how the airflow evolves from the rotor to the surface, but on the effect of the downwash on a sediment bed. The effects of the rotorcraft on the airflow are being considered by other institutions as part of the MURI [5].

The asymmetric nature of rotor flow increases the difficulty of characterizing the flow. The simulated rotor flow circumvents the asymmetric characteristic of the flow by considering the vortex as a sheet parallel to the lower wall. It is quite obvious that the evolution of the rotor vortices is greatly affected by the proximity of the ground as seen on Figure 5. Nevertheless at distances a few rotor diameters away

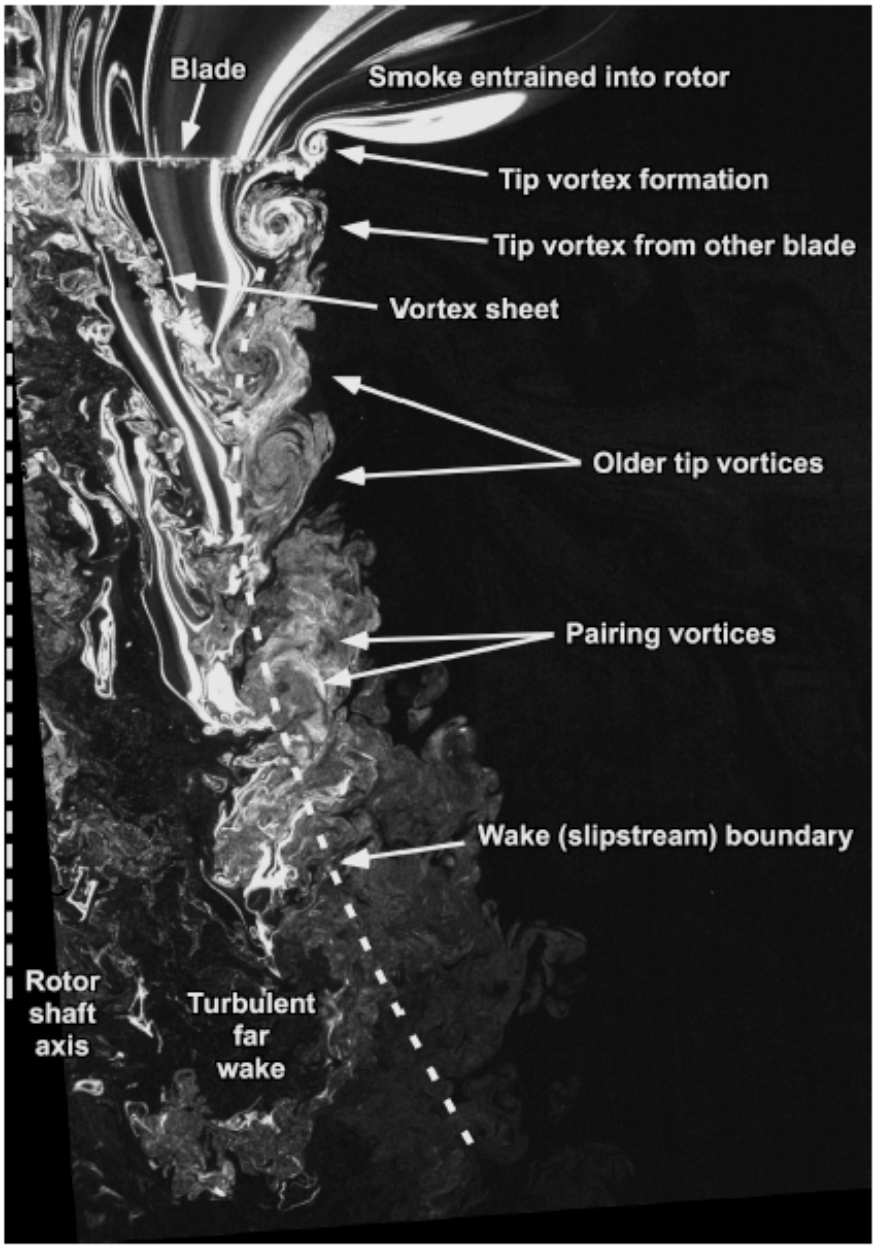

Figure 4. OGE experimental rotor flow [1]

from vortex impingement, the rotorcraft downwash resembles a radially expanding sheet. In actual rotorcraft flow, the vortex sheet expands radially outward which forces the flow to slow to conserve momentum. The numerical model is limited to a rectangular coordinate system where the effect of the radial fluid expansion is ig-

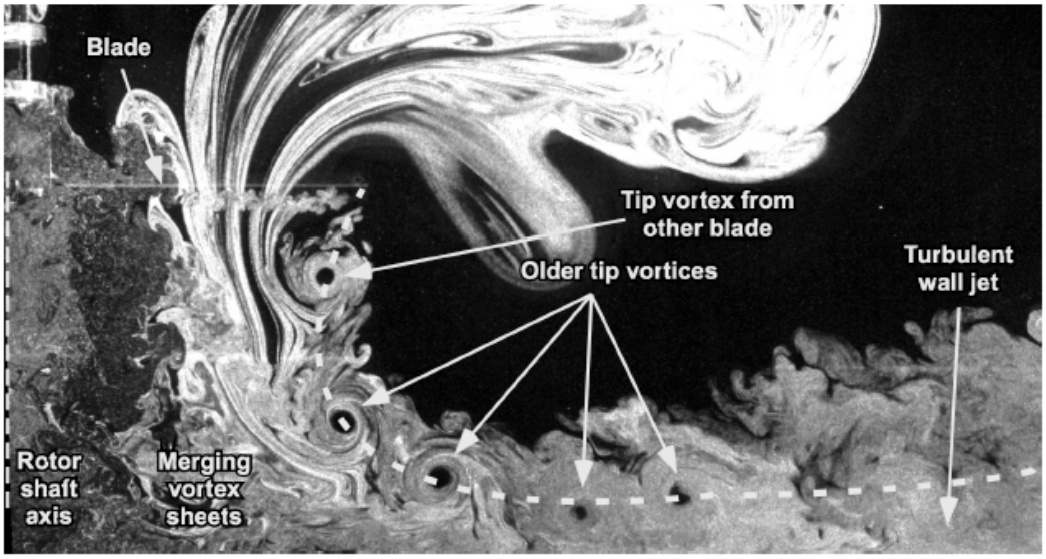

Figure 5. IGE experimental rotor flow [1]

nored. The simulation models the vortices generated by the near ground operation of rotorcraft by superposing a vortex generated by a body force onto a turbulent boundary layer. The idealized rotor flow is combined with the particle tracking scheme to lay the foundation for the near-surface rotorcraft brownout simulation.

The schematic on Figure 6 shows the idealized rotor flow for the entire rotorcraft, however the focus is on the near-surface interactions as seen on the two lower frames of the figure. The flow is a turbulent boundary layer onto which periodic vortex sheets are gradually introduced. The vortex sheets appear at about the edge of the boundary layer and then proceed to convect downstream parallel to the lower surface. Figure (7) shows a number of vortices on the domain, the newly introduced vortex sheet is circular and well defined while the older vortices are dissipated and have lost coherence. As the vortex sheet moves downstream, the initially well-formed, circular sheet begins to dissipate and interact with the particles. By the

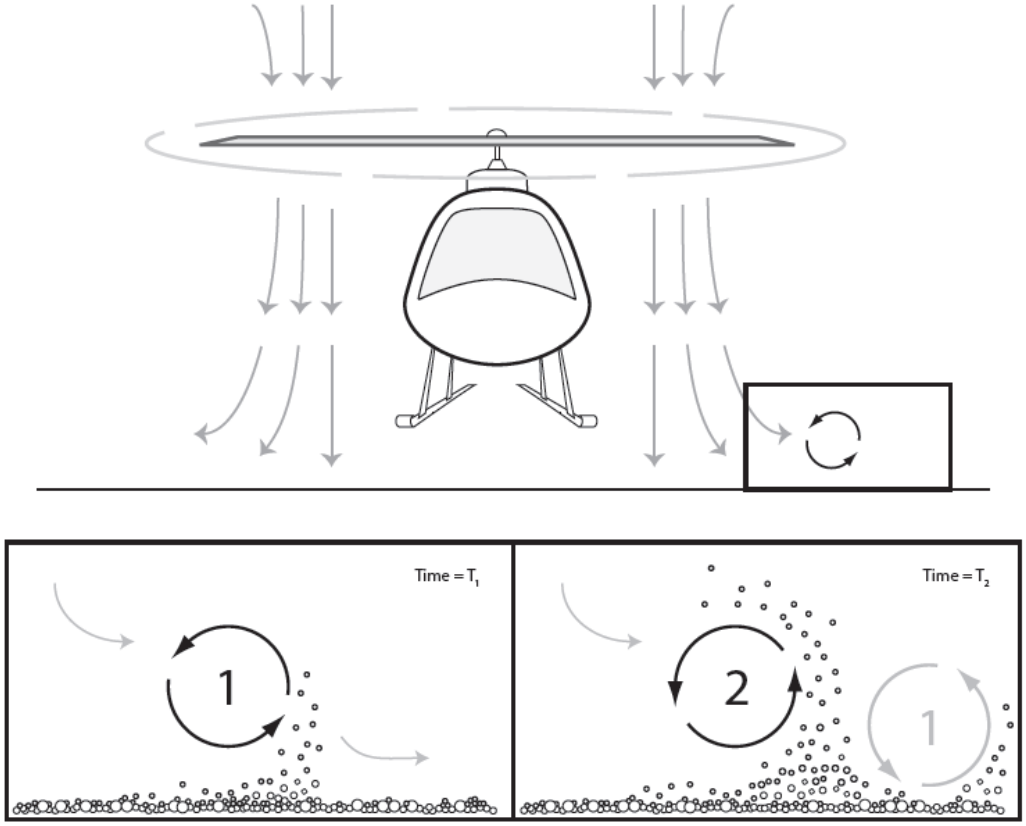

Figure 6. Schematic of simulated rotor with zoomed in section showing the focus of the current investigation

time the vortex reaches the end of the domain the flow has nearly recovered to an equilibrium state. The flow solver, developed by Piomelli *et al.* [23] is combined with the particle tracking module to model the fluid-particle interactions near the ground. More specific details and quantifications concerning the flow solver are contained in the computational approach section.

C. Sediment Transport

The evolution of the brownout cloud is governed by the underlying fluid-particle and particle-particle dynamics. In order to fully comprehend and eventually pre-

dict the brownout cloud formation a thorough understanding of sediment transport physics is necessary. The following is a brief summary on sediment transport, for a more comprehensive review the reader can consult the following references [2, 24–26]. Sediment transport is the response of particles to a fluid in liquid, gaseous, or solid phase as well as particle response to the gravitational force. In practice, sediment is most commonly transported by water, a fluvial process, or by wind, an aeolian process. The response of particles undergoing sediment transport creates the processes of erosion and deposition wherein the sediment uplifted, or entrained, in one area is deposited at some other region. These processes occur naturally due to transport by water, wind, or other fluids. Figure 8 shows the natural process of erosion as a plume of dust erodes from the Sahara Desert over the Atlantic Ocean and into the Canary Islands. As visible from the figure sediment transport is a phenomenon that encompasses multiple length scales.

1. Sediment Properties

Sediment transport is a complicated process in which poly-disperse mixtures of particles are interacting with the environment and colliding with other parti-

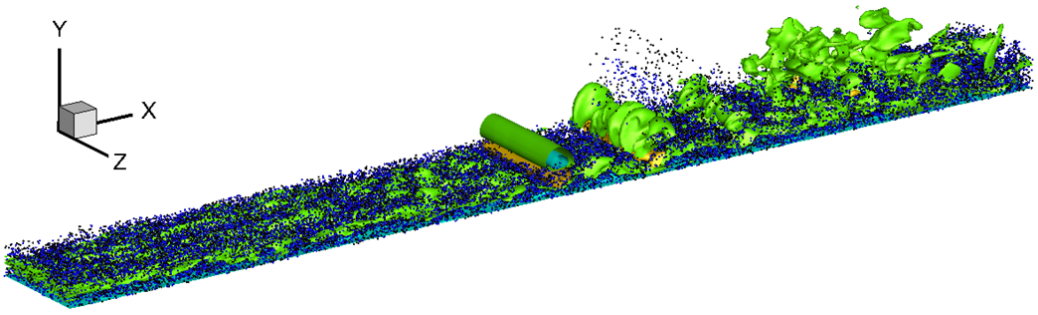

Figure 7. Isometric view of particle-laden coherent vortex flow

cles as well as the surrounding topography. The basic properties of sediment can be divided into two groups, the characteristics of the individual particles and the properties of a mixture of many particles of various sizes. The response of a single sediment particle to a fluid or the gravitational force depends on the physical parameters of the particle. These physical parameters can vary greatly amongst particles and significantly alter the response of the particle [24]. An important characteristic that influences particle transport and deposition is the size of the particle. The sizes

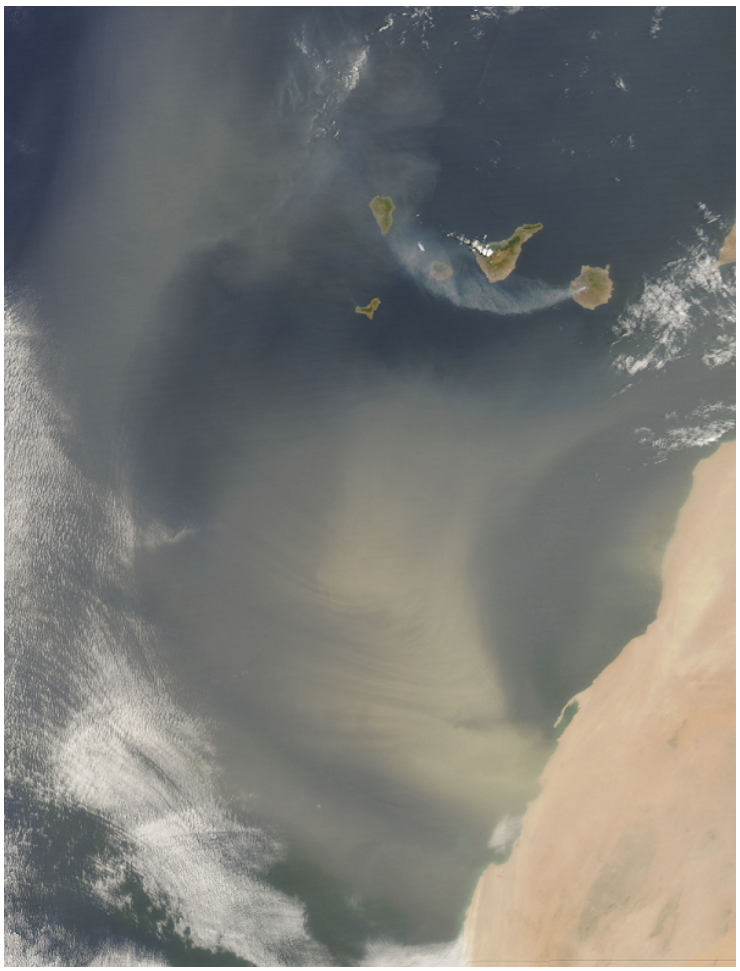

Figure 8. A plume of dust erodes over the Sahara Desert

of particles found in sediment can range significantly and have been categorized by several different institutions and countries as seen on Figure 9.

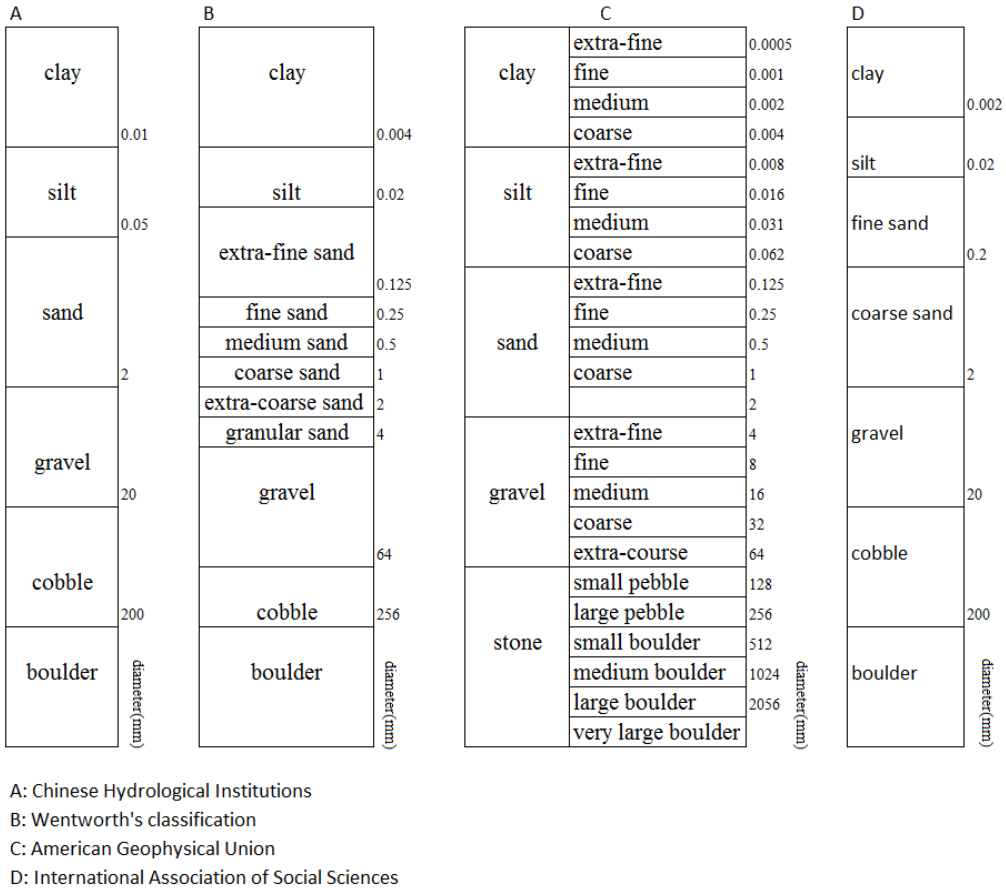

A: Chinese Hydrological Institutions
B: Wentworth's classification
C: American Geophysical Union
D: International Association of Social Sciences

Figure 9. Classification of sediment [2]

Measuring the size of a particle can prove a challenging task, not only because a particle can be very small but also because particles may have highly non-spherical shapes. Specific details on the measurement of very fine particles are outlined by Chien [2], suffice to say the measurement and categorization of particles is not a simple task. Another difficulty associated with the classification of particles is the surface texture of the particle. The particle surface may be either smooth or rough

and will also affect the motion of the individual particle. These are some of the individual particle characteristics that control the response of a single particle undergoing some type of transport. Additionally, environmental conditions will also have an effect on the behavior of the particles the humidity will affect agglomeration, or clumping, of the particles. Furthermore the cumulative effects of individual particles introduce additional sediment characteristics that affect particle motion. These cumulative effects are properties of a sediment mixture composed of individual particles that cover an extensive range of physical characteristics.

In a typical sediment mixture the size distribution of the individual particles covers a wide range of shapes, volumes, and mineral compositions. Furthermore a sediment mixture has voids in the space occupied by the sediment particles known as porosity. The porosity of a sediment mixture depends on the shape, size, and uniformity of the particles as well as other external forces that act on the mixture [2]. The voids make the sediment mixture permeable and so fluid can come into contact with particles below the exposed surface. Another significant characteristic of sediment mixtures is cohesion, which is highly dependent on the individual particle surface texture. Smaller particles, such as clay, are more cohesive than larger particles and tend to form aggregates, a collection of sediment particles. In addition to the aforementioned effects, particles collide against each other as well as any surrounding objects. Finally chemical and electric effects as well as van der Waals forces can also play a significant role on the transport of sediment. Now that the characteristics influencing particle transport have been reviewed, the particle

dynamics will be discussed.

2. Particle Dynamics

A single particle experiences a collection of forces when exposed to an external flow. Figure 10 highlights the different forces which act on a particle under the influence of an aoelian flow. In addition to the gravitational force, W, a single

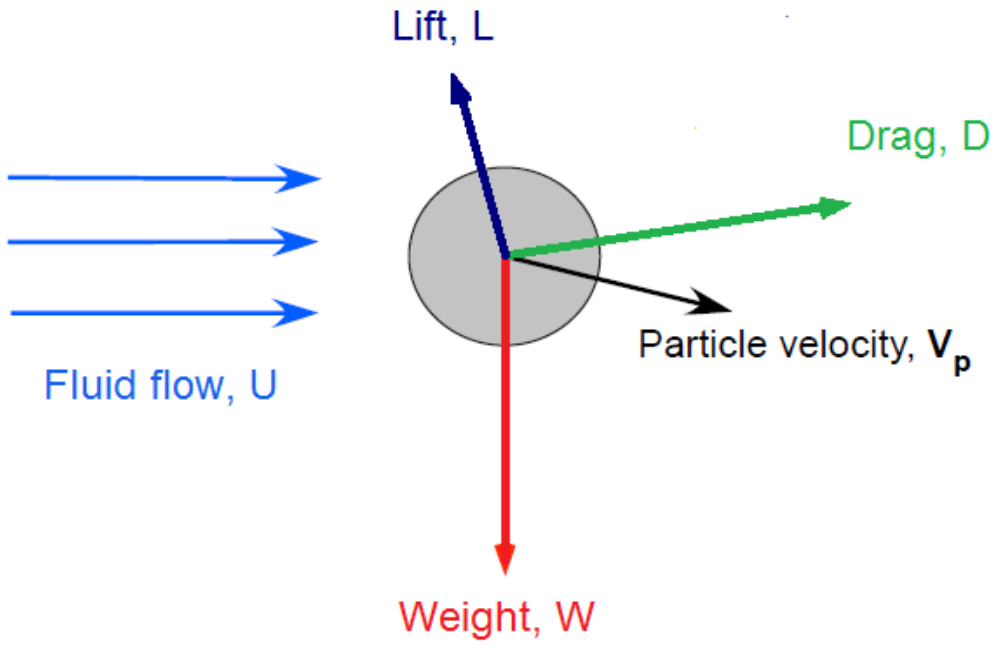

Figure 10. Forces acting on a sediment particle

particle experiences drag, D and lift, L forces. The drag force is a combination of the Stokes drag and an additional drag force produced by the non-spherical shape of sediment particles which varies for each individual particle. The lift forces on a single particle can also stem from the non-spherical shape of a particle as well as from high shear in the flow, known as the Saffman lift force [27]. Another possible contribution to the lift force is the Magnus lift force which occurs when a particle

achieves angular spin. For the two-phase flow under consideration where the particulate density is much larger than the carrier density, $\rho_p \gg \rho_f$, the lift forces are of little consequence [28]. Furthermore, a sediment particle is likely to be in contact with other sediment particles which create cohesive forces amongst the contacting surfaces. Particles experience friction, since most particles are not completely smooth, also particles can experience electrostatic and chemical forces on exposed surfaces. For most particles, electrostatic and chemical forces are probably of little consequence in terms of rotorcraft brownout. The inter-particle cohesion may be more significant and affect the behavior of individual particles which may aggregate into a collection of particles. At some point the forces acting on the particle reach a threshold and the particle undergoes some type of transport.

3. Particle Modes of Transport

Sediment particles from a bed material can be transported in four different ways [25]. First, particles can be transported along the bed without being sus-

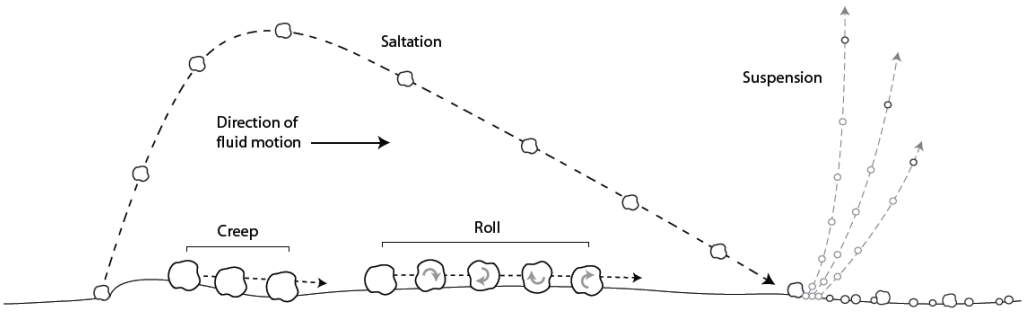

Figure 11. Particle modes of transport

pended. Creep and roll describe the acts of particles sliding or rolling along the sediment bed without being suspended into the flow. Second, single grains are

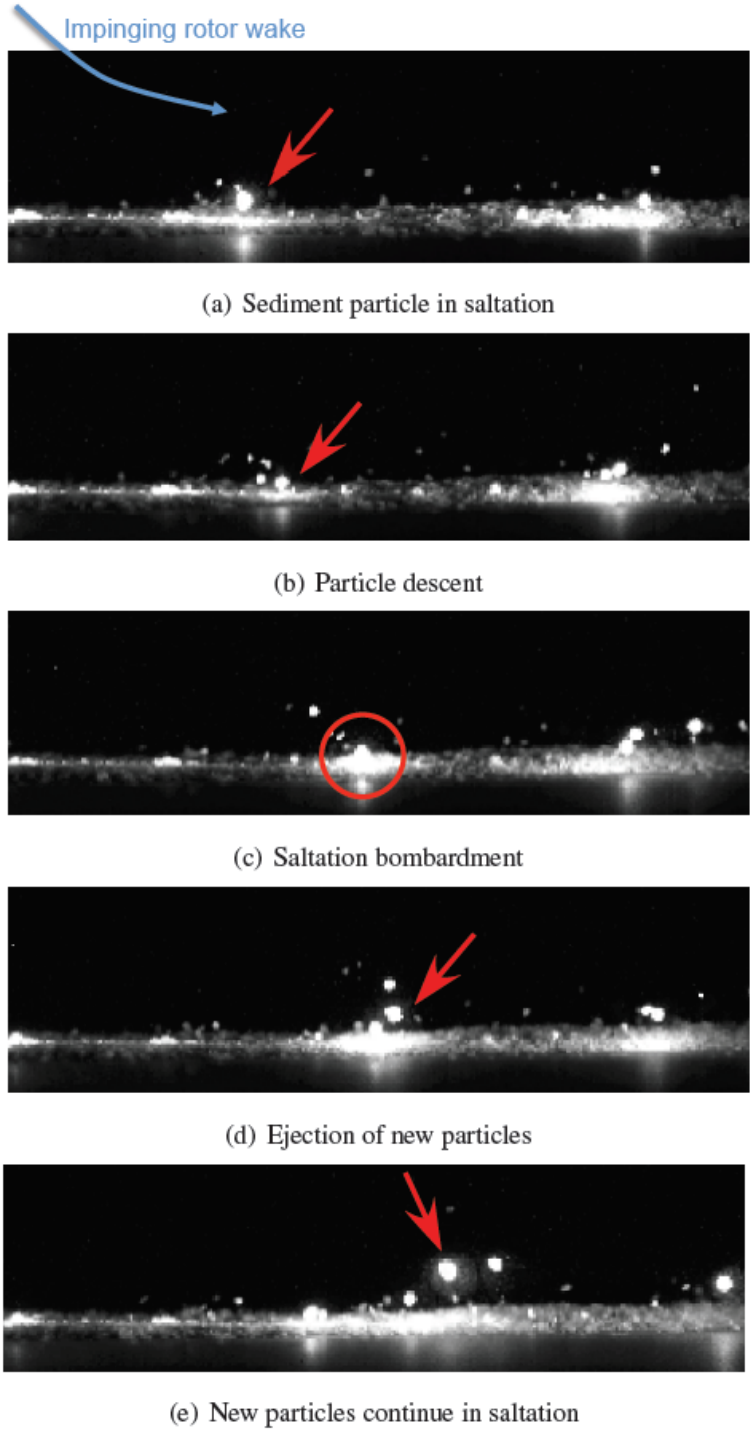

(a) Sediment particle in saltation

(b) Particle descent

(c) Saltation bombardment

(d) Ejection of new particles

(e) New particles continue in saltation

Figure 12. Time sequence showing the process of saltation bombardment [3]

raised from the bed and transported as suspended particles until they become deposited on the bed. This process known as saltation is the event in which a heavier particle is uplifted only a few particle diameters and collides back into the sediment bed effectively transferring momentum onto lighter particles on the sediment bed and causing some of those particles to directly suspend into the flow, known as saltation bombardment. Johnson has an excellent set of snapshots that illustrate the process of saltation bombardment as seen on Figure (12). Third, particles can be suspended onto the flow and rest in suspension throughout the process of transport. Particle suspension describes the event in which a particle is directly entrained from the sediment bed into the flow without returning back into the sediment bed. Finally, the particles may behave as a fluidized material resulting in a two-phase flow. Naturally the occurrence of all or any of the aforementioned events is dependent on particle properties as well as environmental properties. The roundness, density, diameter, porosity, amongst other factors have some effect on whether a particle goes through one transport event over another. Next, the conditions surrounding particle incipient motion are detailed.

4. Threshold Criterion

Perhaps the greatest difficulty surrounding sediment transport is being able to accurately and conclusively predict exactly when a sediment particle will undergo saltation, suspension, or any other form of transport. Over the past several decades extensive work has been carried out in determining the parameters that initiate par-

ticle motion. Naturally, particle incipient motion depends on the forces being exerted on the sediment mixture by the flow and any other external forces. When those applied forces reach a critical value particles become mobilized. The challenge is to determine beyond what threshold particles become entrained by the flow and also to determine the type of transport. Several studies have been performed to describe a threshold criterion that defines when a particle will undergo a specific type of transport event. The notion of a threshold bed shear stress responsible for the motion of a sediment particle has held a central position in sediment transport theory. The threshold criteria in the literature assume the turbulence of the flow has a strong impact on particle entrainment. The suspension of particles from the sediment bed has been associated to the turbulence-particle interactions occurring near the surface of the sediment bed [29–34].

Particle entrainment for uniform flows has been extensively studied, early work by Bagnold [24] set the basis for the classical threshold velocity criterion. The criterion assumes particles remain in suspension if the particle settling velocity w_s, the rate at which a particle settles in still fluid, is less than the vertical velocity component of the turbulent eddies in the flow. These turbulent eddies scale with the flow shear velocity, u^*, and the critical value for the initiation of suspension would satisfy the condition $u^*/w_s = 1$. The flow shear velocity and particle settling velocity can be written as,

$$u^* = \sqrt{\frac{\tau_w}{\rho_f}} \tag{1}$$

$$w_s = \sqrt{\frac{4\rho g d_p}{3C_D}} \tag{2}$$

where τ_w is the wall shear stress, ρ_f is the density of the fluid, g is the gravitational acceleration constant, d_p is the representative mean diameter of the particle, C_D is the coefficient of drag, and $\rho = \rho_p/\rho_f$ is the density ratio between the particle and fluid respectively.

A number of years later van Rijn [35] expanded upon the work of Bagnold and developed a range of limit conditions for which particles are entrained from the sediment and suspended into the flow. Subsequently, Niño *et al.* [36] examined the conditions of previous experiments and developed empirical formulas for the entrainment of sediment from the particle bed. From the aforementioned developments several things become clear, the field of sediment transport is complicated and the subtle details involved in particle incipient motion are not well understood. Furthermore, most work on the threshold criterion for the motion of particles has been performed on uniform flow. Unfortunately regarding brownout sediment transport occurs in a non-uniform flow which has not been studied extensively and whose driving mechanisms may differ significantly from a uniform flow.

The problem of developing a velocity threshold criterion for the sediment particles experiencing rotorcraft brownout is complicated by the non-uniformity inherent in the rotor flow during near ground operation [1]. For uniform flows, the shear stress remains invariant in time and space which is not the case for non-uniform flows. In uniform flow the flux of particles depends linearly on the local surface

shear stress and a critical threshold value. For non-uniform flows the particle entrainment flux can be related to the shear stress based on the turbulent fluctuations of the flow [37]. Haehnel *et al.* [38] performed a set of experiments with an impinging jet on a bed of cohesionless particles. The aim of the experiment was to produce a model for particle entrainment under non-uniform flow, however boundary conditions for non-uniform flows have not been developed. Therefore their methods utilized conditions developed for uniform flows which can be useful even for non-uniform flows if the turbulent fluctuations of the flow can be accurately resolved. Kiger *et al.* [39, 40] have also explored approaches to quantifying the entrainment of particles from non-uniform flows through a set of experiments.

Even though the characterization of particle entrainment in non-uniform flows has not been widely studied, in recent years interest has increased for this particular area of research. From the limited work that has been performed, it seems apparent that the driving mechanisms for non-uniform flow are more subtle and more challenging than the mechanisms in uniform flow. Recent work by Johnson as seen on Figure (13), highlights the sediment trapping effect which is a vortex mechanism that mobilizes sediment from the bed. In the figure, the direct numerical simulation is also shown which displays similar behavior and even with the simplifications and assumptions in the current models the agreement is strong between the experiment and the simulation.

Although significant work is necessary to adequately explain entrainment in non-uniform conditions, the previous work on entrainment from uniform flow will

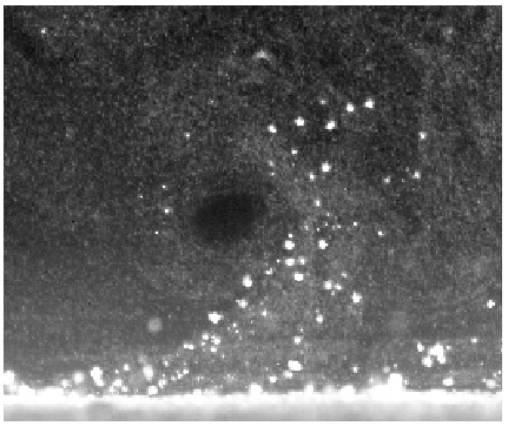

(a) Experiment (B. Johnson [3])

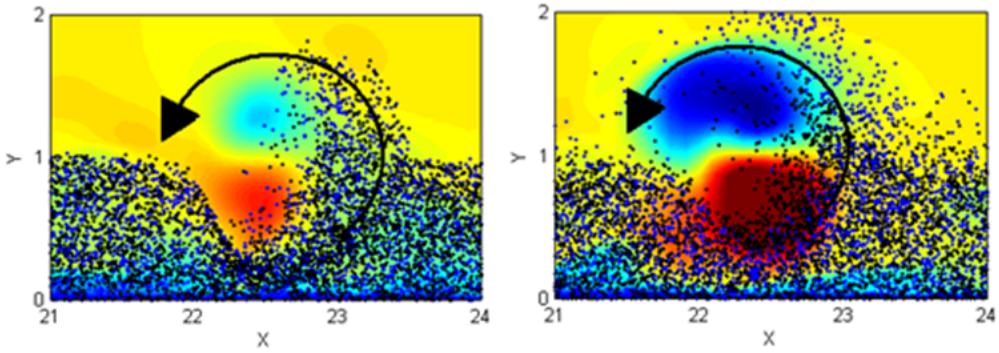

(b) Direct Numerical Simulation

Figure 13. Sediment trapping effect

provide a wealth of knowledge. As more research is completed on the entrainment of particles in non-uniform flow, the appropriate boundary conditions will be revealed and CFD simulations will have access to improved models resulting in more realistic simulations and possible mitigation strategies for the brownout issue.

III. Computational Approach

The simulation is a combination of a Fortran based Eulerian flow solver to model the rotor flow and a C++ based particle module to handle the Lagrangian particle tracking. After the flow is advanced, the particle module is accessed by external functions placed within the Fortran flow solver. In essence the particle module operations become a subroutine in the Fortran program. Once the simulation is initialized the particle module requires the computational grid from the flow solver and then the particle module proceeds to enable operating conditions i.e. whether to enable inter-particle collisions, restart statistics, etc.. From there on, the flow solver will advance the fluid phase and then call an external subroutine that in turn advances the particles. The simulation then continues executing and collecting statistics for both phases which is described in more detail in the subsequent sections.

A. Fluid Phase

The flow solver utilized in the current investigations was developed by Dr. Ugo Piomelli, for more information on the details of the flow solver the reader is directed to the work of Piomelli *et al.* [23] on spanwise vortices. The flow solver is a Direct Numerical Simulation(DNS) of a flat plate boundary layer interacting with periodic spanwise vortices, introduced at the edge of the boundary layer through a forcing method. As the vortices advect downstream, strong perturbations extend to the near-wall region and alter the turbulence dynamics by lifting and deforming the

near-wall eddies as well as interacting with the surrounding particles. The spanwise vortices lose coherence and strength at which point the boundary layer begins a reversal to an undisturbed state. The near-wall region returns to equilibrium more rapidly than the outer region. In the present work, there is a transfer of momentum from the fluid to the particles, but the reverse is neglected. The governing equations for the continuous fluid medium do not include effects from the particle phase.

The governing equations solved for the fluid phase are the conservation of mass and momentum for incompressible flow in which the fluid density remains constant,

$$\frac{\partial u_i}{\partial x_i} = 0 \tag{3}$$

$$\frac{\partial u_j}{\partial t} + \frac{\partial u_i u_j}{\partial x_i} = -\frac{1}{\rho_f}\frac{\partial p}{\partial x_j} + \nu_f \frac{\partial^2 u_j}{\partial x_i \partial x_i} - \frac{\partial \tau_{ij}}{\partial x_i} + f_i \tag{4}$$

in the previous equations u is the fluid velocity where i and j represent the i^{th} and j^{th} component of the velocity. The symbol f_i is a force term used to introduce spanwise vortices onto the turbulent boundary layer. The pressure is identified by p, the kinematic viscosity is ν_f, and the fluid density is ρ_f. The subgrid-scale stresses, τ_{ij}, are computed directly in this numerical simulation. To perform a direct numerical simulation of the incompressible Navier-Stokes Equation (4) the scale of the discretized mesh must be on the same order as the smallest flow structures. DNS requires the grid spacing to be on the order of the Kolmogorov length scale [41]

defined as,

$$\eta \equiv \left(\frac{\nu_f^3}{\epsilon} \right) \tag{5}$$

where ϵ is the kinetic energy dissipation rate. DNS does not resort to turbulence models and is more computationally expensive than Large Eddy Simulation(LES). In LES, rather than solving the small scale turbulence directly, turbulence models are utilized to describe the small scale turbulent motions. For the current investigation, DNS is chosen to drive the knowledge of this non-uniform flow which can then be applied to develop more refined LES models.

The numerical model utilizes second-order central differences for both convective and diffusive terms. The wall-normal diffusive term employs a semi-implicit Crank-Nicolson scheme, while the other terms use an Adams-Bashforth scheme. The Poisson equation is solved by applying a Fourier transform for both the streamwise and spanwise directions and directly solving the resulting tridiagonal matrix at each wavenumber. The flow solver employs the MPI scheme to divide the computational domain amongst a chosen number of processors.

1. Non-dimensional Equations

The equations of motion for the fluid, Equation (3) and (4), are non-dimensionalized with the free stream velocity, U_∞, the boundary layer thickness, δ,

and the fluid density ρ_f.

$$\begin{aligned} \overline{u}_i &= \frac{u_i}{U_\infty}, \quad \overline{t} = t\frac{U_\infty}{\delta}, \quad \overline{x}_i = \frac{x_i}{\delta}, \\ \overline{p} &= \frac{p}{\rho_f U_\infty^2}, \quad \overline{\tau}_{ij} = \frac{\tau_{ij}}{U_\infty^2}, \quad \overline{f}_i = f_i\frac{\delta}{U_\infty^2}. \end{aligned} \tag{6}$$

The non-dimensional variables shown in Equation (6) are substituted into the dimensional equations of motion and after some algebraic manipulation governing equations become

$$\frac{\partial \overline{u}_i}{\partial \overline{x}_i} = 0 \tag{7}$$

$$\frac{\partial \overline{u}_j}{\partial \overline{t}} + \frac{\partial \overline{u}_i \overline{u}_j}{\partial \overline{x}_i} = -\frac{\partial \overline{p}}{\partial \overline{x}_j} + \frac{1}{Re}\frac{\partial^2 \overline{u}_j}{\partial \overline{x}_i \partial \overline{x}_i} - \frac{\partial \overline{\tau}_{ij}}{\partial \overline{x}_i} + \overline{f}_i \tag{8}$$

where

$$Re = \frac{\delta U_\infty}{\nu_f} \tag{9}$$

describes the Reynolds number for the flow, $Re = 2800$. The non-dimensional time step, $\overline{t} = 0.001$ is held constant. The dimensions of the computational domain are also non-dimensionalized with the boundary layer thickness

$$\overline{x} = \frac{x}{\delta}, \quad \overline{y} = \frac{y}{\delta}, \quad \overline{z} = \frac{z}{\delta} \tag{10}$$

and represent the streamwise, wall-normal, and spanwise dimensions respectively.

At the lower wall, a no-slip boundary condition is applied, while periodic boundary conditions are applied in the spanwise directions. At the upper domain,

a far-field boundary condition is applied, $\overline{u}_1 = 1, \partial\overline{u}_2/\partial\overline{y} = \partial\overline{u}_3/\partial\overline{y} = 0$. At the inflow, the recycling/rescaling method by Lund *et al.* [42] is used, while at the outflow a convective condition is applied [43]. The recycling plane is chosen well upstream of the location where the vortices are initially introduced.

2. Simulated Rotor Vortex Parameters

The spanwise vortices are introduced by a local force in the momentum equation. The tangential velocity from the vortex has the following expression

$$V_\theta(r) = A_f \begin{cases} A \sin \pi r/(2r_1), & 0 \le r \le r_1 \\ \{1 - \exp -(a_1 r)^2\} \,/\, \exp(a_2 r)^2, & r > r_1 \end{cases} \tag{11}$$

where

$$r_1 = \frac{1}{a_1}\sqrt{\ln\left(\frac{a_1^2 + a_2^2}{a_2^2}\right)} \quad \text{and} \quad A = \frac{1 - \frac{a_2^2}{a_1^2+a_2^2}}{\left(\frac{a_1^2+a_2^2}{a_2^2}\right)^{(a_2/a_1)^2}} \tag{12}$$

The parameters a_1 and a_2 determine the size of the vortex core, the maximum tangential velocity and r_1, the location of the maximum V_θ. A_f is an amplitude factor used to achieve the desired circulation $\Gamma = \oint_{r=r_1} V \cdot dl$. The values for $a_1 = 3.3$ and $a_2 = 2.7$ which result in $r_1 \approx 0.3$ are used in the present investigations. Becuase the vortices are introduced at the edge of the boundary layer, the induced velocity is negligible at the wall. The tangential velocity V_θ obtained from Equation 11 is shown in Figure 14. The parameter A_f is selected to achieve a Reynolds number based on circulation, $Re_\Gamma = \Gamma/2\pi V = 3150$. This value is comparable

to the circulation of the vortices in experimental studies of rotor wakes interacting with the ground by Johnson [3]. To determine f_i, the direct forcing method de-

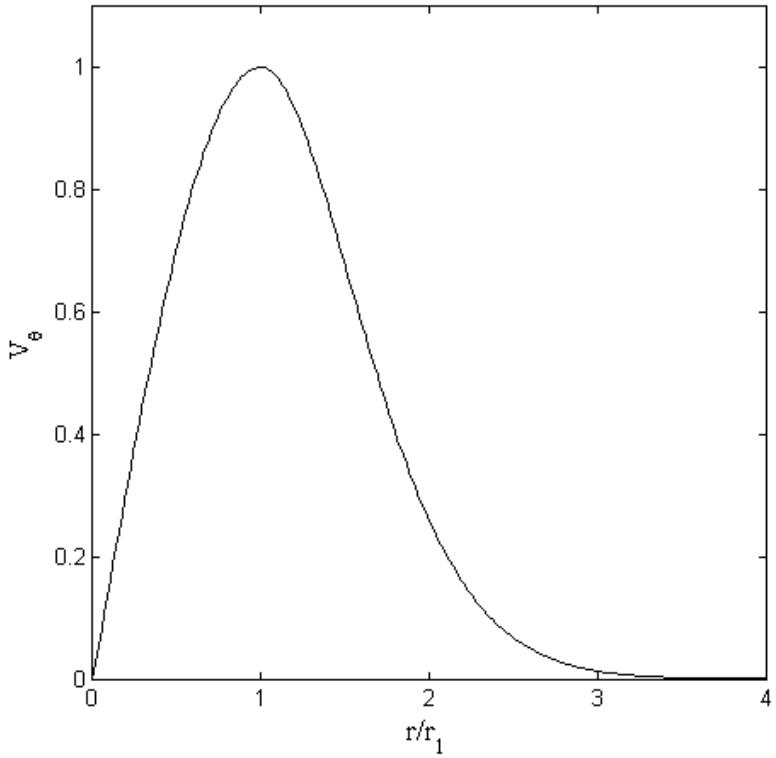

Figure 14. Tangential velocity distribution of the vortex

veloped within the framework of Immersed-Boundary Methods [44] is utilized to define a force,

$$f_i = \frac{u_i - V_{\theta,i} - U_\infty \delta_{i1}}{\Delta t} \tag{13}$$

where $V_{\theta,i}$ are the Cartesian components of V_θ. After the velocity correction step, the vortex does not have the desired peak velocity at $r = r_1$. The factor A_f is adjusted and within 2 or 3 iterations the desired circulation of the vortex is achieved. The force is applied locally and gradually, over a short region. After the vortices

with the desired circulation have been generated, the force is set to zero and the flow is governed by the standard Navier-Stokes equations.

3. Fluid Parameters

The computational domain for the fluid simulation is large to analyze the behavior of the flow as the vortices dissipate and the conditions revert back to an undisturbed state. The domain is specifically long in the streamwise dimension to capture the evolution of the vortex sheet. In the wall-normal direction the grid spacing is determined using a hyperbolic function to maintain the grid points in the near wall region compact. As the grid moves into the outer region, the spacing becomes increasingly coarser. For the other dimensions a linear spacing is employed. The parameters of the fluid grid are summarized in Table (1). The grid spacing for the

Table 1. Fluid grid parameters

	$Streamwise$	$Wall-normal$	$Spanwise$
Symbol	x	y	z
Length	80δ	6δ	4δ
Points	802	128	98
Spacing	linear	hyperbolic	linear

streamwise and spanwise directions is $\Delta x = 0.1$ and $\Delta z = 0.0418$ respectively. The wall-normal component of the grid spacing varies and is defined by

$$\begin{aligned} \eta_y &= \frac{m-1}{2\left(N_y-1\right)},\ 0 \leq m < N_y \\ \widetilde{y}_m &= L_y\left[1+\frac{\tanh\left(\alpha\left(\eta_y-\frac{1}{2}\right)\right)}{\tanh\left(\frac{\alpha}{2}\right)}\right] \\ y_m &= \frac{\widetilde{y}_{m+1}-\widetilde{y}_m}{2} \end{aligned} \tag{14}$$

$$\Delta y_m = \frac{y_{m+1} - y_m}{2}. \tag{15}$$

Equation (14) describes the location of the grid points along the wall-normal direction. N_y is the number of segments along the wall-normal direction, L_y is the total length of the geometry in the wall-normal dimension. The grid points are distributed as a hyperbolic function, with α determining the stretching of the grid spacing. For the cases under consideration, $\alpha = 5.029$ to force fine resolution near the lower wall.

B. Particulate Phase

In the present investigation, the effects of the particles on the carrier flow are neglected and the fluid velocity remains undisturbed by particle effects. After the fluid velocity u_f has been advanced by the flow solver, the particle module shares access to a common block where the fluid velocity is stored. After rearranging the fluid velocity into a new array to conform to the C++ row-major standard, the particle module can then proceed to advance the particles. The motion of the particles is computed through a Discrete Particle Simulation(DPS) by numerically integrating the equation of motion for a small sphere in unsteady, non-uniform velocity field [45]. The equations of motion for the particles are,

$$\frac{dx_{p,i}}{dt} = v_{p,i} \tag{16}$$

$$\frac{dv_{p,i}}{dt} = -\frac{3}{4}\frac{\rho_f}{\rho_p}\frac{C_D}{d_p}|\boldsymbol{v}_r|v_{r,i} + g_i \tag{17}$$

where $x_{p,i}$ and $v_{p,i}$ are the i^{th} component of the particle position and velocity, $v_{r,i}$ is the particle relative velocity, and g_i is the acceleration due to gravity. The particle relative velocity is the difference between the particle and fluid velocities at the particle position

$$v_{r,i} = v_{p,i} - u_{f,i} \tag{18}$$

while $|\boldsymbol{v}_r| = |v_{r,i}v_{r,i}|$ is the magnitude of the slip velocity. The drag coefficient, C_D, for a particle with a correction to extend the particle Reynolds number, Re_p, range of the drag force [46] is given by

$$C_D = \frac{24}{Re_p}(1 + 0.15Re_p^{0.687}) \tag{19}$$

while the particle Reynolds number is expressed as

$$Re_p = \frac{|\boldsymbol{v}_r|d_p}{\nu_f} \tag{20}$$

where ν_f is the kinematic fluid viscosity.

The particle equations of motion, are integrated in time using second order Adams-Bashforth. Since the particles are not necessarily located at fluid grid points, Equation (17) employs third-order Lagrange polynomials to interpolate the fluid velocity to the particle location. The equation of motion can be compactly rewritten as,

$$\frac{dv_{p,i}}{dt} = -\frac{|\boldsymbol{v}_r|}{\tau_p} + g_i \tag{21}$$

where τ_p is the particle relaxation time expressed as,

$$\tau_p = \frac{\rho d_p^2}{18\nu_f}(1 + 0.15Re_p^{0.687})^{-1} \tag{22}$$

though more commonly the particle relaxation time is simplified to

$$\tau_p = \rho d_p^2/(18\nu_f). \tag{23}$$

The inclusion of gravity in the particle equation of motion is enforced through a particle settling velocity. The settling velocity of the particles is expressed as

$$w_s = g_i\tau_p \tag{24}$$

and the value is chosen to be identical for both particles.

1. Non-dimensional Equations

The equation of motion for the particles, Equation (17), is non-dimensionalized with the free stream velocity, U_∞ and the boundary layer thickness, δ

$$\overline{v}_{p,i} = \frac{v_{p,i}}{U_\infty}, \quad \overline{t} = t\frac{U_\infty}{\delta}, \quad \overline{l} = \frac{l}{\delta}, \quad \overline{g}_i = g_i\frac{\delta}{U_\infty^2}. \tag{25}$$

The non-dimensional variables shown in Equation (25) are substituted into the dimensional equation of motion and after some algebraic manipulation the particle

equation of motion becomes

$$\frac{d\overline{v}_{p,i}}{d\overline{t}} = -\frac{|\overline{\boldsymbol{v}}_r|}{\overline{\tau}_p} + \overline{g}_i. \tag{26}$$

Particle properties including the diameter and the particle response times as well as the particle settling velocity are also expressed in non-dimensional form

$$\overline{d}_p = \frac{d_p}{\delta}, \quad \overline{\tau}_p = \frac{\rho \overline{d}_p^2}{18\nu_f}, \quad \overline{g}_i = \frac{\overline{w}_s}{\overline{\tau}_p}. \tag{27}$$

The value of the non-dimensional settling velocity, $\overline{w}_s = 0.02$ is based on a simplified formula for estimating particle settling velocity [47].

In addition the relevant particle parameters are also presented in viscous units. The variables of interest are transformed with the friction velocity, u_τ and the kinematic fluid viscosity, ν_f

$$v_{p,i}^+ = \frac{\overline{v}_{p,i}}{\overline{u}_\tau}, \quad t^+ = \frac{\nu_f}{\overline{u}_\tau^2}, \quad l^+ = \frac{\nu_f}{\overline{u}_\tau}. \tag{28}$$

The particle parameters are chosen such that the particle viscous diameter, $d_p^+ = 1$ independent of the particle density ratio

$$d_p^+ = \frac{\overline{d}_p}{l^+} = \overline{d}_p \frac{\overline{u}_\tau}{\nu_f}. \tag{29}$$

The particle relaxation time in viscous units is computed to compare results with

previous simulations with similar conditions

$$\tau_p^+ = \frac{\overline{\tau}_p}{t^+} = \overline{\tau}_p \frac{\overline{u}_\tau^2}{\nu_f}. \tag{30}$$

2. Particle Parameters

Simulations are performed for two particle Stokes numbers, $St = \tau_p/(\delta/U_\infty)$. In all simulations the diameter of the particles was specified as one viscous unit. Therefore the variation in Stokes number is realized by varying the density ratio, as summarized on Table 2. The particle response times are chosen so that the lighter particle follows the fluid closely while the heavier particle is less affected by the flow. In addition the density ratios chosen encapsulate a wide range of density ratios found in nature.

Table 2. Particle parameters

ρ_p/ρ_f	504	2016
St	4	16
τ_p^+	28	112

The simulations are carried out for two particle groups with an equal number of particles. The number of particles per group, N_p depends on whether inter-particle collisions are enabled since the computation of collisions is computationally expensive. Initially the position of the particles is randomly generated for the streamwise and spanwise components. The wall-normal component of the initial particle position is also randomly generated, however, a constraint is enforced to keep the particles within a specified range, h_p which differs depending on whether inter-

particle collisions are enabled as shown on Table 3. The particle volume and mass fractions are also outlined on the table. The fractions are computed with the initial space occupied by the particles as enforced by h_p. Also the initial velocity of the particles is equal to the fluid velocity interpolated to the particle position.

Table 3. Particle operating conditions

$Collisions$	N_p	h_p	V_{frac}	M_{frac}
Off	$32M$	1.5δ	0.0127	$6.4(light)$ $25.6(heavy)$
On	$10M$	5δ	0.0012	$0.6(light)$ $2.4(heavy)$

There are a number of distinct boundary conditions enforced for the particles. In the wall-normal direction, a particle is assumed to contact the smooth lower wall when the center of the particle is one radius from the wall, and elastic collisions are enacted for wall contact events. If a particle reaches the top wall, then the particle is reintroduced at the inlet with a randomized wall-normal position to be located somewhere within the constraint h_p. The spanwise position of the particle remains unchanged while the velocity is reinitialized and once again set equal to the fluid velocity interpolated to the new particle position. For particles that move out of the channel in the spanwise direction periodic boundary conditions are applied to reintroduce the particle into the computational domain. When a particle reaches the far downstream outlet, then the particle is reintroduced at the inlet identical to the treatment at the upper wall. In addition, since the computational domain is divided amongst the total number of processors N_{procs}, the particles may go through several processors during the execution of the simulation. The details of the parallel

handling of the particles are outlined in the next section.

3. Parallel Treatment of Particles

Initially the parallel treatment of the particulate phase was based on Linux socket code. This method was applied before the MPI paradigm became the method of choice in most parallel applications. In essence the Linux socket code and the MPI scheme are very similar although there are some fundamental differences. The use of MPI simplifies the treatment of parallel simulations since the majority of the work is done by the MPI libraries, essentially one is not required to manually open and close ports of communication between two different machines and/or processors. The manual operation of ports was a necessary step with the Linux socket code, nevertheless the transfer of data was somewhat simpler than with MPI since the receiving machine or processor only needed to know the amount of bytes being passed. In the current MPI implementation, it is necessary to describe the type of variable being transferred (i.e. integer, floating point value, character, etc.) in addition to the quantity of the specific type of variable being transferred. Essentially, this is necessary to ensure the number of bytes passed remains consistent as with the Linux socket approach, albeit somewhat more involved than the Linux code. However MPI affords the user an opportunity to create a new datatype to easily send and receive structs that can contain a variety of datatypes. For more information on the inner workings of the MPI paradigm the reader is directed to the MPI Users Guide [48].

Although the Linux socket code has some advantages it also suffers from several limitations. First, MPI is the method of choice for most parallel implementations, also MPI offers a set of standards for parallel communication between different computer architectures, from a desktop server to a super computer with thousands of processors. Second and most importantly, MPI implementation is portable and not necessarily restricted to architecture or programming language and can also be scaled effectively. In the simulations the flow solver is based on the Fortran programming language while the particle module uses C++ and both the flow solver and particle module access the same MPI distribution. Compiling programs with multiple languages can be challenging and the appropriate libraries have to be linked so the languages can work in tandem. Furthermore, the same logic applies for the MPI libraries and a specific library has to be linked for the Fortran compiler as well as the C++ compiler.

The bulk of the parallel communication on the particle module revolves around the point to point transfer of particles entering and exiting a subvolume of the domain. During each timestep after the flow solver advances the fluid, the particle module advances the particles and proceeds to check whether a particle has reached a location beyond the computational domain on either side as seen on Figure 15. If a particle goes beyond the domain then the particle is passed on to the following processor along with the relevant information including velocity, group, and individual number. The transfer of particles between processors is capable of handing and receiving in both directions though the fluid flow is mostly from left to right

which means most particles are travelling from left to right. Particles in the vicinity of the vortex may be ejected from right to left though for the majority of the particles the bulk of fluid motion is from right to left. The particle transfers occur between all active processors during every time step and after the transactions are finalized each processor purges its own particle struct to avoid redundancy.

In the present investigations, the simulations use 32 processors, $N_{procs} = 32$ and the computational domain is divided along the streamwise direction into 32 sections of equal size and volume. The turbulent boundary layer simulation remains fairly homogeneous along the streamwise component which results in consistent load balance across the processors. Even though the number of particles on the individual processors varies, the amount of particles on any given processor remains mostly uniform. The only potential problem is the inclusion of the vortex which has a more pronounced effect on the particles near the point of insertion. Even with the vortex, the load balance on the processors remains well within operational limits and does not pose an issue for the simulations.

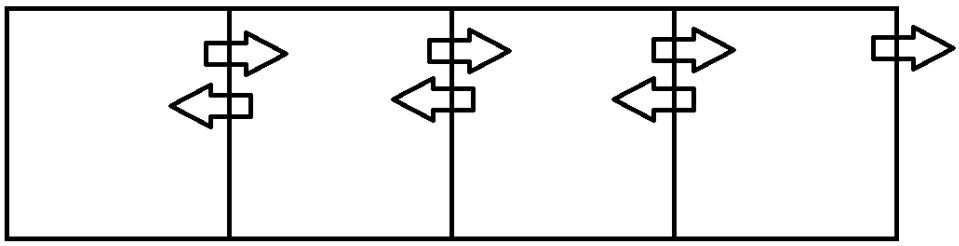

Figure 15. Representative sections of computational domain

4. Inter-Particle Collisions

This section is a brief summary of the treatment of particle-particle collisions, for a more detailed implementation of the collision algorithm the reader is referred to Vance [49]. Inter-particle collisions are computed by accounting for all particle pairs that collide within each timestep. Only binary collisions without energy dissipation or inter-particle friction are considered. If a particle collides with multiple particles during one timestep only the earliest collision detected is enacted. Furthermore collisions are monodisperse and checked independently for each particle group in addition to being checked once per timestep. To avoid the quadratic expense of naive collision detection, the computational domain is divided into sections comprised of a three dimensional array of cells. In performing this manipulation, the possible list of collision partners is reduced to those particles residing at the same cell as the particle under consideration or one of the adjacent 26 cells. In essence when checking collision pairs, a particle is restricted to a neighborhood of cells as shown on Figure 16.

The size of the cells comprising the collision detection neighborhood is dependent on particle parameters and must be chosen such that no particle-particle collisions remain undetected. It is possible to make the cells of the collision detection algorithm large and ensure that no collisions are overlooked, however the increase in size also increases the computational cost. The cells need to be large enough to account for all possible inter-particle collisions, but also as small as possible

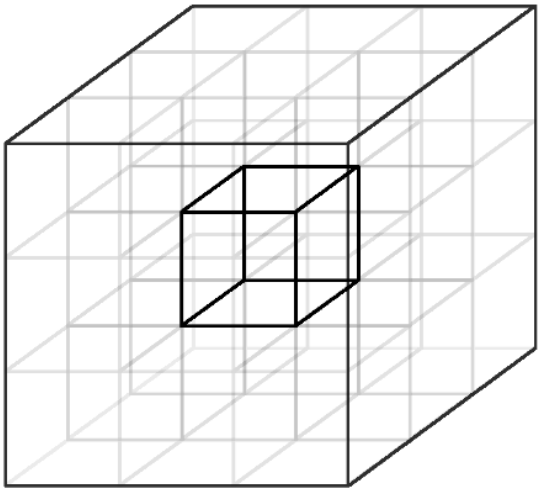

Figure 16. Collision detection neighborhood

to reduce the computational cost of checking for collisions pairs. The size of the collision detection cells depend on the timestep and the maximum attainable particle velocity. With these conditions as the basis for the collision detection cells the maximum relative displacement of any particle pair between successive timesteps will be within the collision detection neighborhood. This approach assumes that the maximum attainable velocity of a particle is known beforehand. Knowing the parameters of the flow it is simple and effective to estimate a maximum velocity based on observations and check that the maximum observed relative velocity does not exceed the prediction.

The collision detection scheme divides the computational domain into neighborhoods to minimize the potential particle pairs, however, a collision pair may be on separate processors. At every timestep the processors send and receive the particles on the edges of the computational domain to the adjacent processors on

either side. These particles are received by a temporary particle array and the simulation proceeds to check whether or not these particles participate in a collision. This temporary particle array is not added to the particles currently on the processor, the temporary struct is simply used to check whether or not a particle has a collision and after the check is complete the temporary arrays are released from memory. The geometry of a particle pair before and during a collision are showed

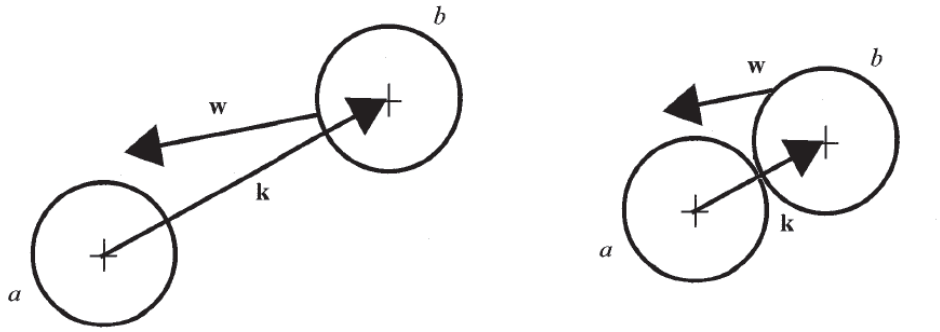

(a) Before impact (b) During impact

Figure 17. Collision geometry

in Figure 17. The relative position of the particles is $k_i = x_{a,i} - x_{b,i}$ and the relative velocity $w_i = v_{a,i} - v_{b,i}$. A collision event at the instant t^c is defined by

$$k(t^c) = r_a + r_b, \quad r_a = r_b = r_p, \quad k(t^c) = 2r_p \tag{31}$$

where r_a and r_b are the radii of the particle pair. For the monodisperse particle populations considered in this investigation, a collision occurs at the instant t^c when the relative distance between two particles is equal to the particle diameter. The instant of impact is t^c and the particle velocities are assumed constant over the collision

detection interval. The effects of inter-particle collisions are approximated using relations for the perfectly elastic impact of two smooth spheres of equal mass. Only translational momentum is exchanged during a collision. The modified velocities for a particle pair undergoing a collision are given by,

$$\begin{aligned} v_{a,i}^{c} &= v_{a,i} + \frac{1}{4r_p^2} k_i(t^c) k_j(t^c) w_j \\ v_{b,i}^{c} &= v_{b,i} - \frac{1}{4r_p^2} k_i(t^c) k_j(t^c) w_j \end{aligned} \tag{32}$$

where $v_{a,i}^{c}$ and $v_{b,i}^{c}$ are the modified post collision velocities of particle a and particle b, respectively. Finally, the relative position at the instant of impact is expressed as,

$$k(t^c) = k(t^{n-1}) + w(t^c - t^{n-1}) \tag{33}$$

where $t^n - t^{n-1}$ is the time interval between collision detection searches.

5. Mesoscopic Eulerian Formalism

During rotorcraft brownout very large numbers of particles are swept from the ground and suspended in the air. A numerical simulation of brownout requires an accurate model for the impinging blade tip vortices and also a particle tracking model to keep track of each individual particle. Ideally, a simulation would be extremely realistic and have billions or perhaps trillions of particles, nevertheless a simulation of that magnitude is not possible with the current available hardware. Rather than attempting a simulation with billions or trillions of particles, Fevrier

et al. [50] developed a statistical approach which enables the decomposition of the instantaneous particle velocity field into two contributions for dilute suspensions of heavy particles in gas-solid turbulent flows. The first contribution shared by all the particles in the domain is called the mesoscopic Eulerian particle velocity field and the second contribution corresponds to the quasi-Brownian velocity distribution which is a random velocity component unique to each particle. The particle velocity for the Mesoscopic Eulerian Formalism(MEF) is decomposed as follows,

$$v_p(t) = \tilde{v}_p + \phi v_p \tag{34}$$

where $\tilde{v}_p$ represents the common particle velocity and ϕv_p is the random component as seen on Figure (18). The evaluation of the MEF is performed using local volume averages by dividing the computational domain into cubes. This requires large particle ensembles such that any given volume will contain a sufficient number of particles in order to obtain meaningful statistics and avoid variation in the mesoscopic field of the particles.

A goal of the simulations is to provide qualitative predictive models for the behavior of sediment exposed to rotor downwash. In order to provide accurate and robust models to the MEF approach from the Lagrangian particle tracking simulations, large particle ensembles are necessary. This necessary increase in the number of particles is what led the evolution of the particle module onto the Saguaro cluster system. Once the relevant parallel sections were ported to the MPI scheme, the par-

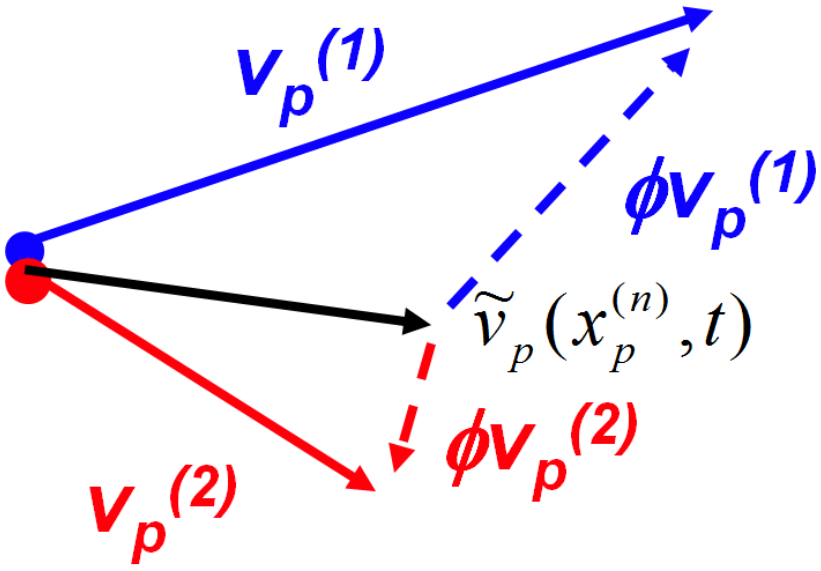

$$v_p^{(n)}(t) = \tilde{v}_p(x_p^{(n)}(t), t) + \phi v_p^{(n)}(t)$$

Figure 18. Velocity decomposition for a single particle into common and random components

ticle module can take advantage of the parallel processing offered by the Saguaro cluster. Lagrangian simulations with large particle ensembles can lead to knowledge of the behavior of the random, uncorrelated particle velocity contribution that must be modeled. The correlated contribution of the particle velocity field can then be computed in an Eulerian scheme to achieve true two-phase simulations of the dusty gas.

C. Collection of Statistics

The statistics for the fluid are computed at every grid point, but since particles are transported along the domain it is necessary to compute the statistics for the particles differently. The particle statistics are computed on a per bin basis, the

computational domain is divided into bins and quantities of interest are calculated for every bin. Figure (19) shows a contour of streamwise velocity and the reconstruction of the particle velocity from the particle distribution within the domain. In essence a single bin may contain a few tens or even a few hundred particles, but the statistical quantities are averaged to a single value effectively replacing many particles with a single mean value. The calculation of a statistical quantity is as follows,

$$\psi = \frac{1}{N_b} \sum_{i=1}^{N_b} \Psi_i \tag{35}$$

where N_b represents the total number of particles in a given bin, while Ψ_i and ψ are the statistical quantity for an individual particle and the statistical quantity for the entire bin respectively.

Even though the simulations utilize millions of particles, in order to formulate adequate statistics, the particle statistics are taken at a single spanwise plane. The particles are all projected onto a single spanwise plane to ensure a large number of particles on every bin. Since the flow is mostly symmetric along the spanwise dimension, spanwise averaging will not distort the acquired statistics. The collection of statistics begins after 150 viscous time units of execution to reduce artifacts on the particle statistics by the initial conditions. After the statistics are enabled the collection of statistics take place every ten iterations over a period of 350 viscous time units in the most computationally expensive simulation and over 500 viscous time units in the less taxing simulations. This amount of time ensures that the par-

ticles are exposed to a significant number of vortices and provides opportunity for the particles to reach equilibrium.

For simulations with multiple groups, the particle groups are independent of each other and are unaffected by the other particle groups, so each group is a monodisperse particle group. When investigating the macroscopic behavior particles are not spanwise averaged, instead there are almost as many bins as there

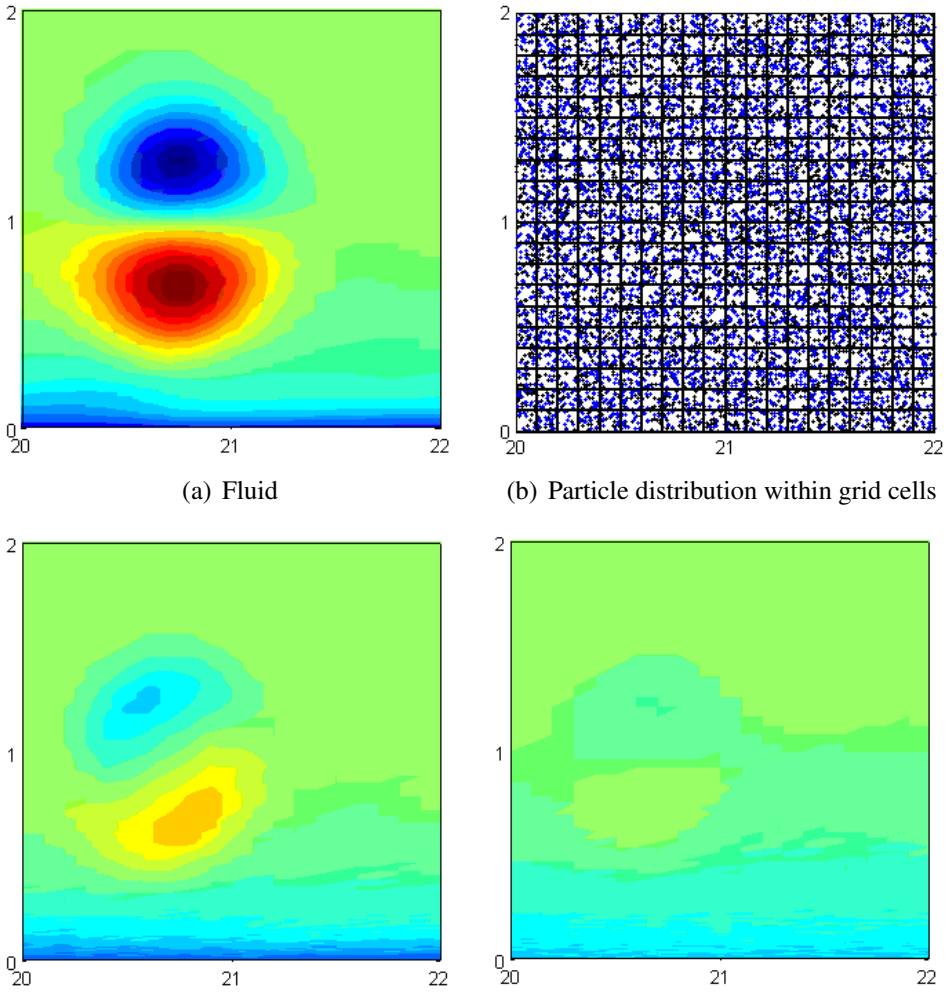

(a) Fluid (b) Particle distribution within grid cells

(c) $\tau_p^+ = 28$, blue (d) $\tau_p^+ = 112$, black

Figure 19. Instantaneous streamwise velocity

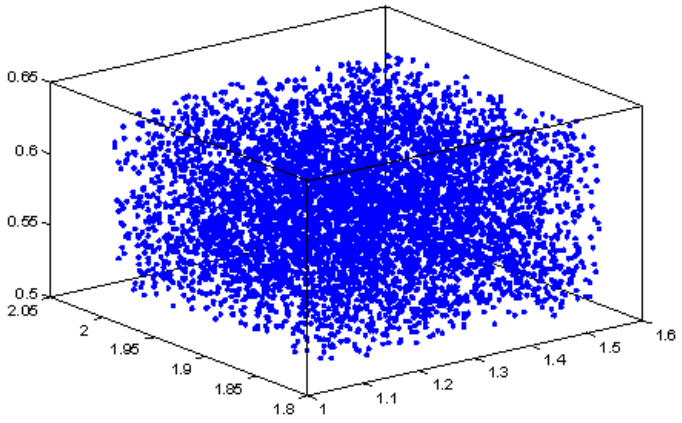

(a) Subset of particles

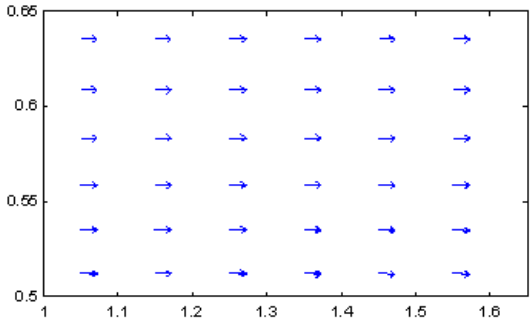

(b) Particle data condensed into a single plane

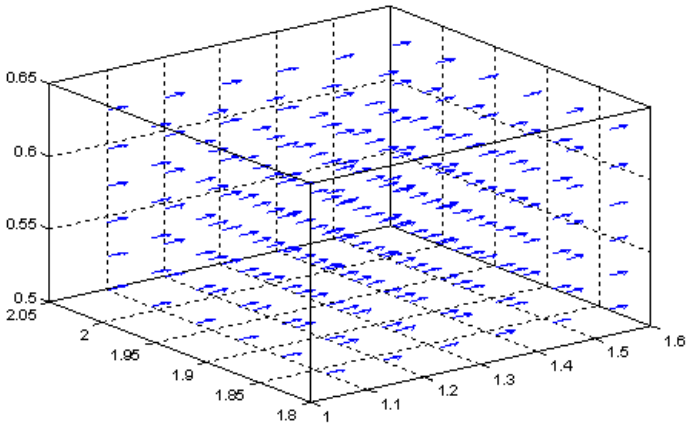

(c) Particle data acquired for every plane

Figure 20. Particle velocity vectors, spanwise averaged (b) and without averaging (c)

are grid points. Figure (20) shows a particle distribution while the subfigures show both approaches of computing statistics at a bin.

The particle wall-normal grid differs from the fluid grid. In the fluid wall-normal grid the spacing near the wall is very fine to capture the details within the boundary layer. This spacing is small enough that a particle diameter is larger than the length between the first two fluid grid points. Therefore the spacing for the particle wall-normal grid was modified to accommodate the particles, by modifying $\alpha = 2.5$ in Equation (14) and recomputing the wall-normal grid points. This has no effect on the acquired statistics, other than having a more even distribution of particles throughout the bins.

A variety of statistics are computed to shed light on the response of the particles, especially the competing effects of inter-particle collisions and the simulated rotor vortex. The following section shows the results of the simulations and the comparisons for cases with and without collisions as well as both types of flows.

IV. Results

In this section, figures highlighting the fluid-particle interaction are shown to help the reader visualize the two-phase flow. Subsequently, a short subsection details some fluid statistics that are independent of the particles. The fluid results section is aimed at shedding light on the difference between the two types of flows in the simulations: with and without vortices. Finally, the last subsection details the particle results for both types of flows and also with and without inter-particle collisions.

A. Fluid-Particle Interactions

The particles are greatly affected by the vortices, Figure (21) shows the evolution of a particle distribution through time. The different snapshots are only a few time units apart and the evolution of both the particles and the vortices can be easily followed. These figures highlight the ease with which the particles are affected by the flow, but to fully understand the effects of the vortex on the flow, quantitative measures are necessary.

The simulated rotor vortex is introduced as a sheet on the computational domain. Figure (22) displays the vortex sheet from different angles and the particles in the vicinity of the vortex. The sediment trapping effect, the sudden change in the vertical velocity induced by the vortex, is clearly visible in the images. Figure (23) shows the computational domain colored by streamwise velocity contours in addition to showing zoomed in isosurface views of the vortex. These figures clearly

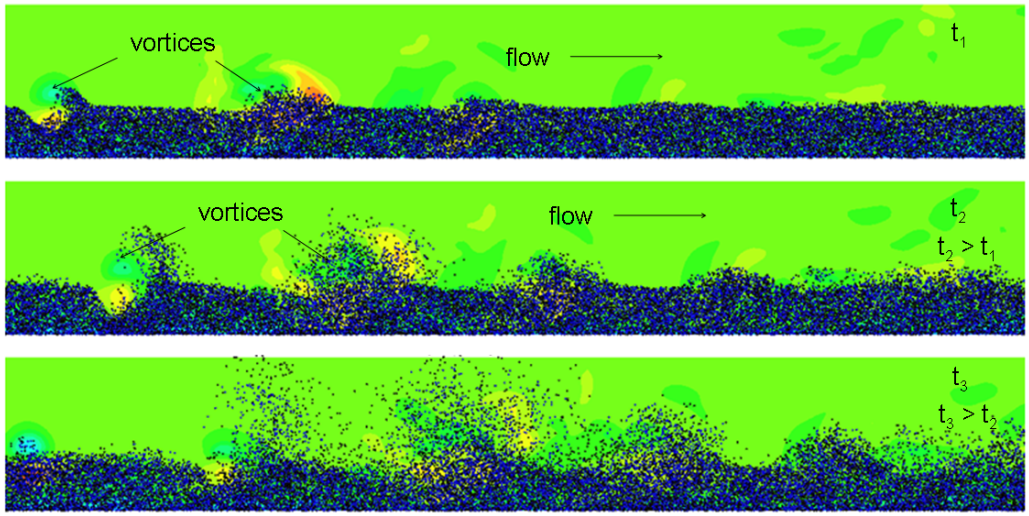

Figure 21. Evolution of coherent vortices interacting with particles

show the effect of the flow on the particles but of more significance is the long term effect of the flow on the particles.

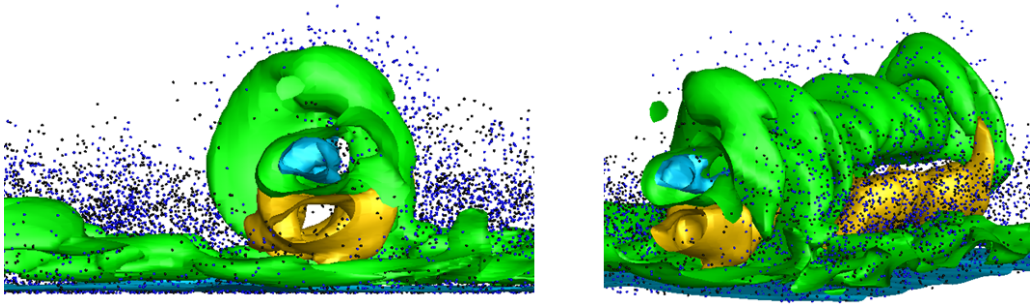

Figure 22. Vortex-particle interaction

The influence of the vortex on the particles is obvious but there are questions that are not so obvious. What is the region in which the vortex influence remains strong? Which is more important the vortex effects or inter-particle collisions? These are some questions that are not easily answered which require more quantitative measures to analyze. The next sections are aimed at providing more details on the long term effects of the vortex.

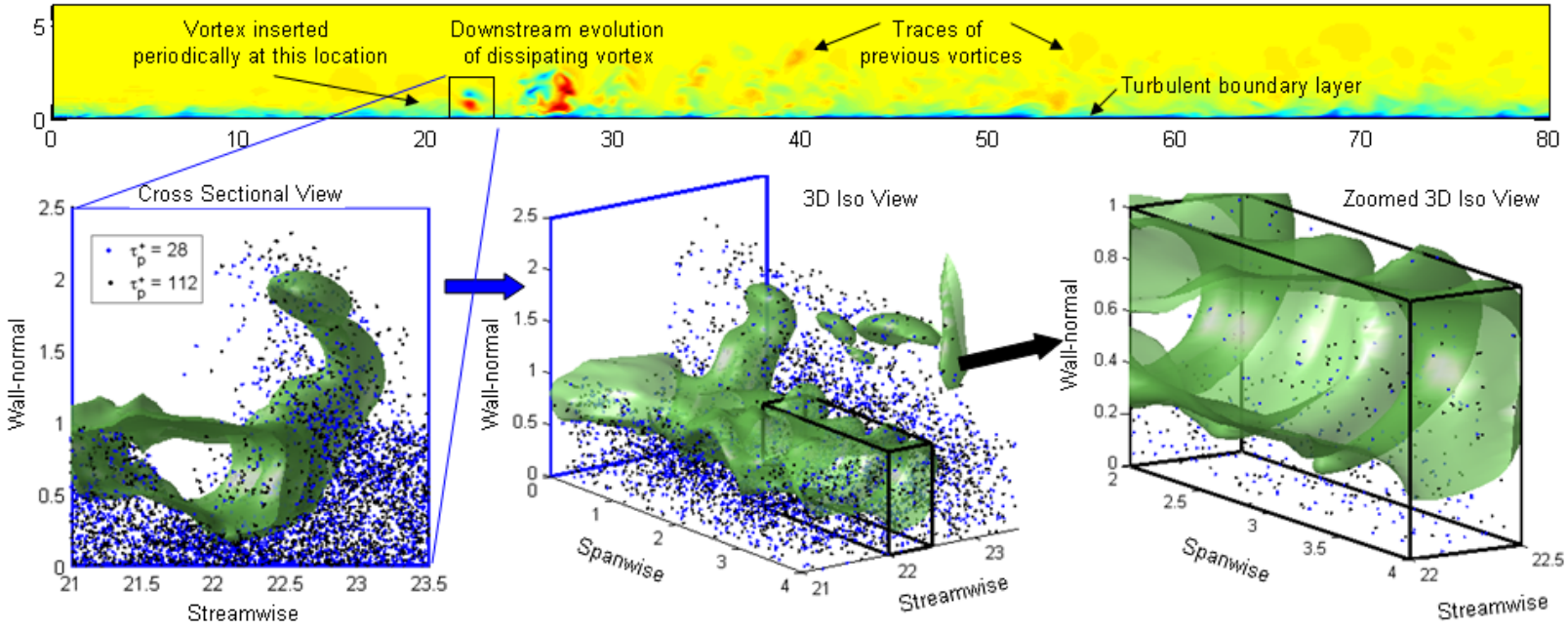

Figure 23. DNS of large-scale coherent vortex introduced into particle-laden turbulent boundary layer

B. Fluid Phase

Before reviewing the particle statistics, fluid statistics are presented and analyzed. The focus of the current investigation is not on the fluid phase, however having an understanding of the underlying characteristics of the flow can shed light on the behavior of the particles. A select few statistics of the fluid phase are shown, for more detailed information on the intricacies of the flow the reader is directed to the work of Piomelli *et al.* [23]. The simulations are one-way coupled so the particles have no effect on the fluid phase. The fluid statistics remain unaffected by the particle distribution in the domain. The following statistics shown on Figure (24) are normalized by the friction velocity, $\overline{u}_\tau$. From this point forward the turbulent boundary layer will be abbreviated as TBL in subsequent figures and the vortex superimposed on the turbulent boundary layer will be abbreaviated as V-TBL.

The effect of the vortices on the statistics is clear, especially on the streamwise velocity. The blue line is close to the inlet at a point in the domain in which both flows are turbulent, therefore there is little variation between both flows at that point in the domain. As vortices are introduced into the domain, the statistical quantities begin to be greatly affected. Both the streamwise and the wall-normal turbulence intensities display significant differences away from the lower wall. Essentially, the vortices introduce strong perturbations that increase the wall shear stress. In addition, spanwise vortices generate significant turbulent kinetic energy near the wall. Finally the vortices lose coherence and the flow reverses to an equilibrium

state and the vortex flow resembles the turbulent boundary layer flow.

The fluid statistics shown in Figure (24) are normalized with the friction velocity which is dependent on the wall shear stress, τ_w. In the streamwise fluid velocity plot, there is a large decrease in the normalized fluid velocity which is due to an increase in the wall shear stress as seen in Figure (25). On the other hand the wall shear stress for the turbulent boundary layer remains almost constant through the entire domain. The vortices are introduced at around $\overline{x} = 20$, and so the regions before this location have very similar values since both flows are turbulent at those points. At around the region where the vortex is introduced there is a small decrease

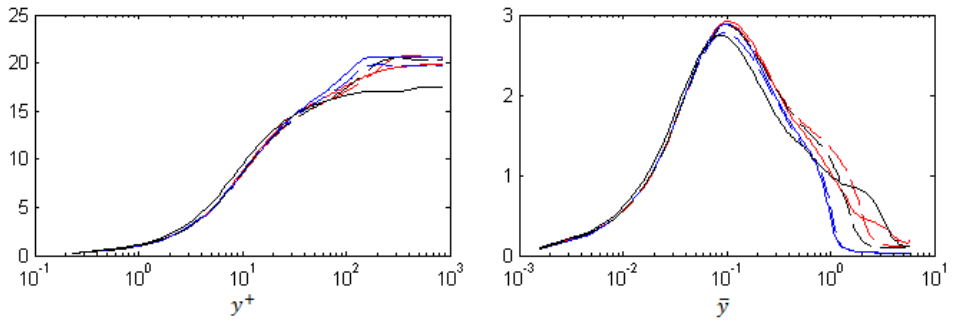

(a) Streamwise velocity (b) u_{rms}

(c) v_{rms} (d) $u'v'$

Figure 24. Fluid phase statistics at different streamwise locations.
— V-TBL, - - TBL.
Blue: $\overline{x} = 10$, *Black*: $\overline{x} = 40$, *Red*: $\overline{x} = 70$

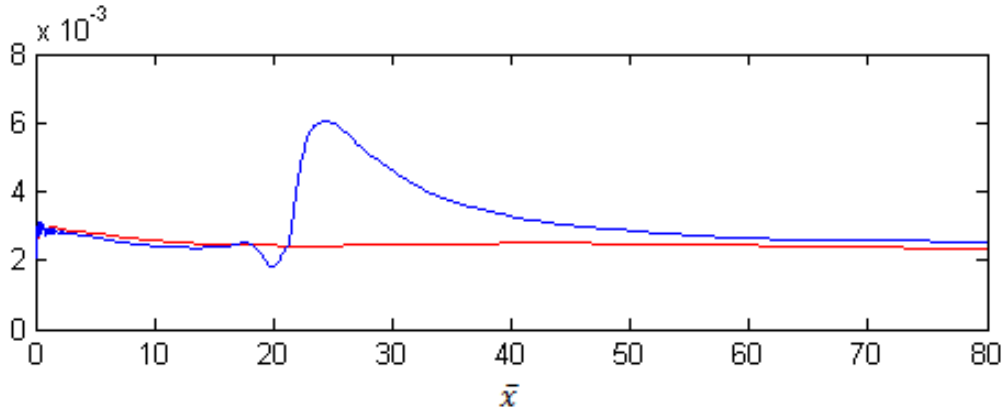

(a) Wall shear stress

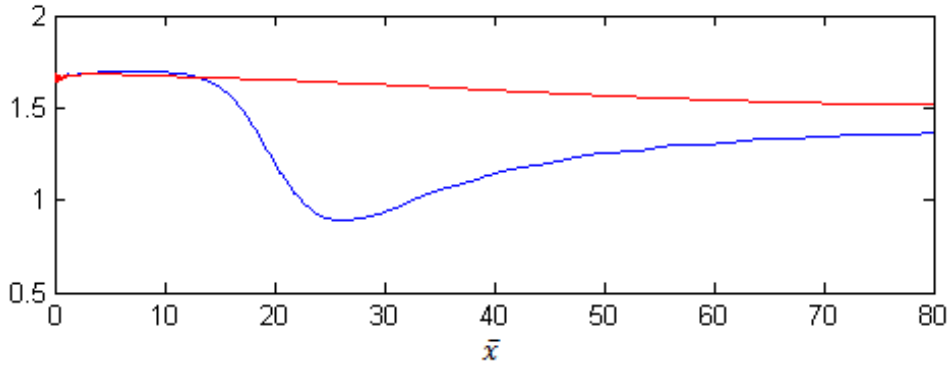

(b) Shape Factor

Figure 25. Fluid phase statistics along streamwise direction.
Blue: V-TBL, *Red*: TBL

in the wall shear stress and then a sudden sharp increase that slowly decreases as the vortices convect through the domain. Also shown is the shape factor defined as the ratio between the displacement thickness and the momentum thickness. Again the shape factor for the turbulent flow remains mostly constant while the vortex flow experiences sharp gradients near the point of vortex introduction.

C. Particulate Phase

The instantaneous particle distribution with and without collisions for the vortex flow is shown at a series of wall-normal planes in the following figures. As has been shown many times, particles tend to accumulate in regions of low vorticity and high strain rate [12] in the absence of inter-particle collisions. The instantaneous particle distribution in this case displays preferential concentration in certain regions of the flow. Preferential concentration describes the accumulation of dense particles within specific regions of the instantaneous turbulence field. The mechanisms which drive preferential concentration are centrifuging of particles away from vortex cores and accumulation of particles in convergence zones [13, 51]. Snapshots of the particle positions and the gas phase equivalent are shown at different wall-normal planes. The particle concentration of the lighter particles near the wall is higher than the heavier particles. In addition to the increased particle concentration, the lighter particles display more defined regions of preferential concentration while the larger particles tend to resist the influence of the flow. At a plane some distance above the wall that slices through the vortex ring, $y^+ = 175$ the distribution of both particles show defined regions of preferential concentration due to the effects of the vortex. The inclusion of particle-particle collisions disrupts the formation of preferential concentration regions as seen on previous work [49]. At planes near the wall, both particle groups show very little preferential concentration for cases including collisions, nevertheless there is a collection of particles in the

trail of the vortices. At the plane that slices through the vortex, even the colliding particles exhibit some preferential concentration though much less pronounced than the case excluding collisions.

The particle number density is shown for all simulations. Simulations without inter-particle collisions are initially seeded between $0 \leq \overline{x} \leq 1.5$ and simulations with collisions range from $0 \leq \overline{x} \leq 5$. The particle number density is defined as

$$n_I = \frac{1}{\Delta y_b} \sum_{m=1}^{N_b} m \tag{36}$$

$$n_D = \frac{1}{N_s} \sum_{I=1}^{N_s} n_I \tag{37}$$

where n_I is the instantaneous number density for a given bin, N_s is the total number of times particle statistics have been sampled, and n_D is the average number density for a given bin. Simulations without inter-particle collisions tend to accumulate particles in the near-wall region, an effect that has been observed in previous simulations [14]. The inclusion of particle-particle interactions leads to a more uniform particle concentration. This effect of inter-particle collisions on particle concentration has also been observed in previous work [18, 52]. For both simulations with and without vortices, the particles are diffusing into the outer flow, albeit more significantly for the case with vortices. Across both types of flows the particles are diffusing, in addition the heavier particles are diffusing further than the lighter particles. The simulations with gravity show less flux of particles across the

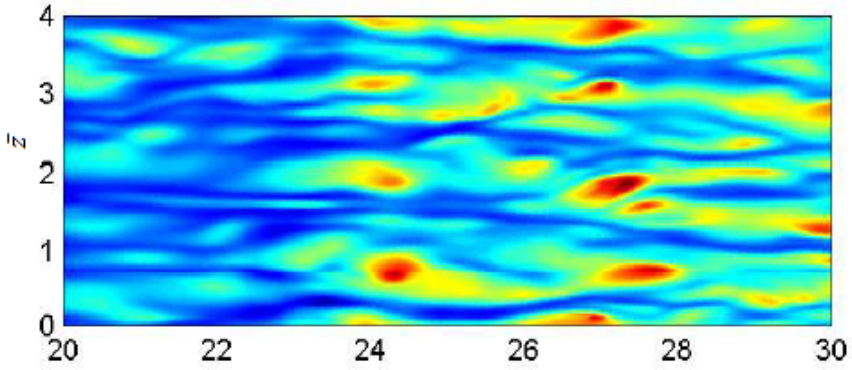

(a) Instantaneous streamwise fluid velocity

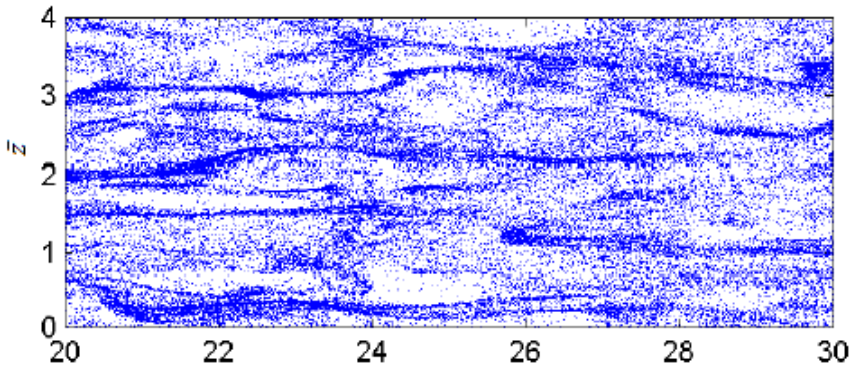

(b) $\tau_p^+ = 28$

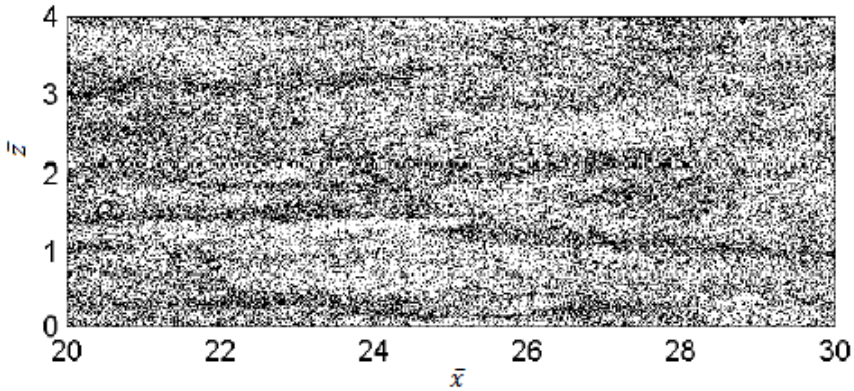

(c) $\tau_p^+ = 112$

Figure 26. Instantaneous particle distribution without collisions at $y^+ = 5$

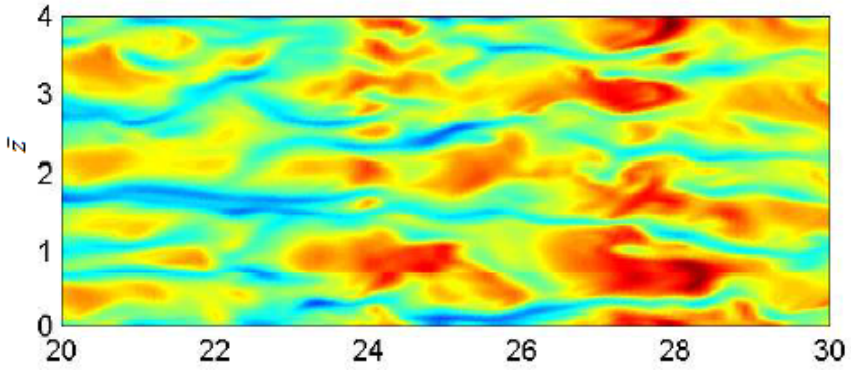

(a) Instantaneous streamwise fluid velocity

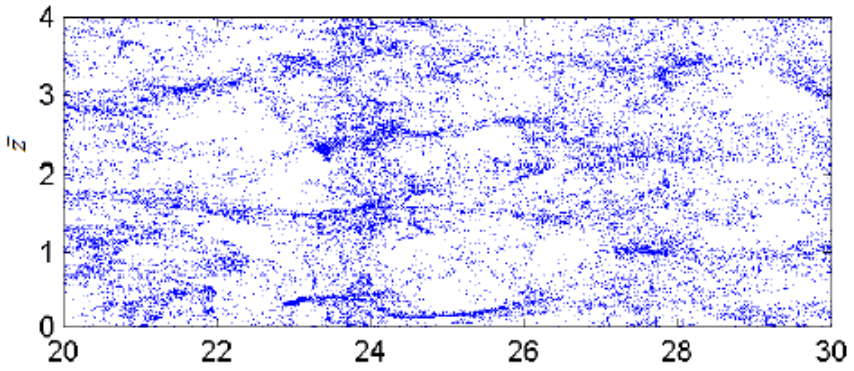

(b) $\tau_p^+ = 28$

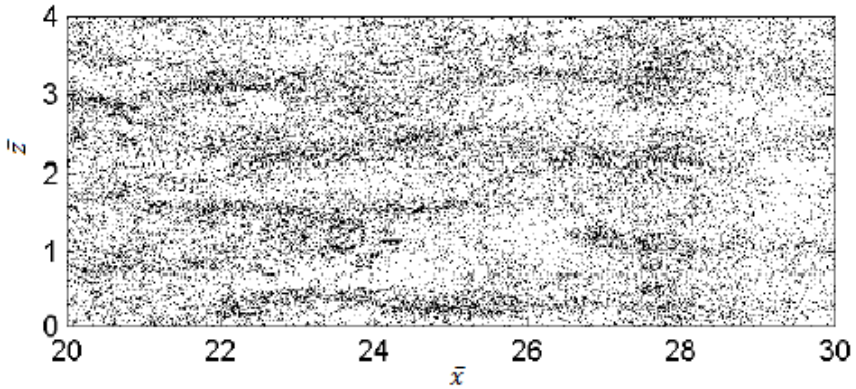

(c) $\tau_p^+ = 112$

Figure 27. Instantaneous particle distribution without collisions at $y^+ = 20$

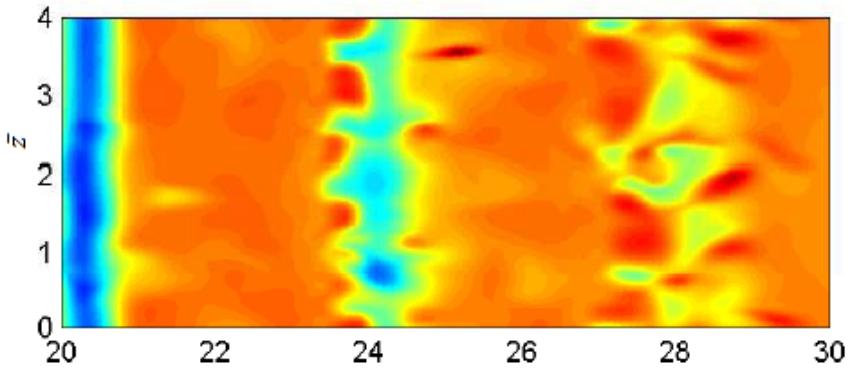

(a) Instantaneous streamwise fluid velocity

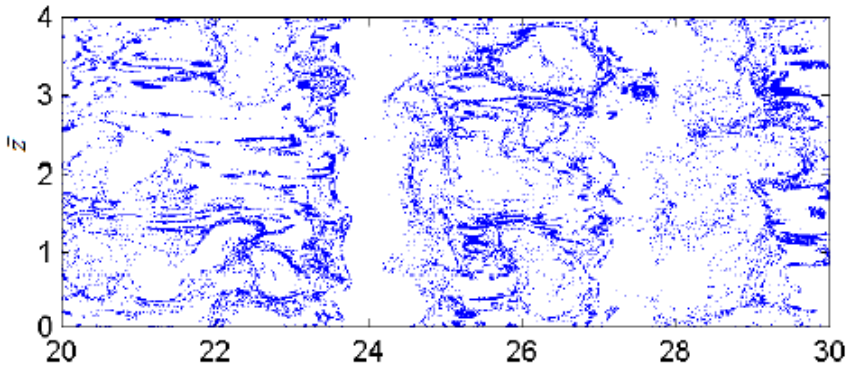

(b) $\tau_p^+ = 28$

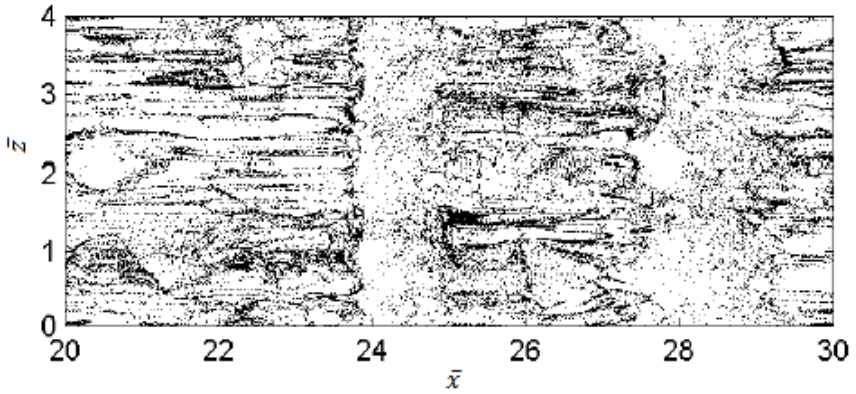

(c) $\tau_p^+ = 112$

Figure 28. Instantaneous particle distribution without collisions at $y^+ = 175$

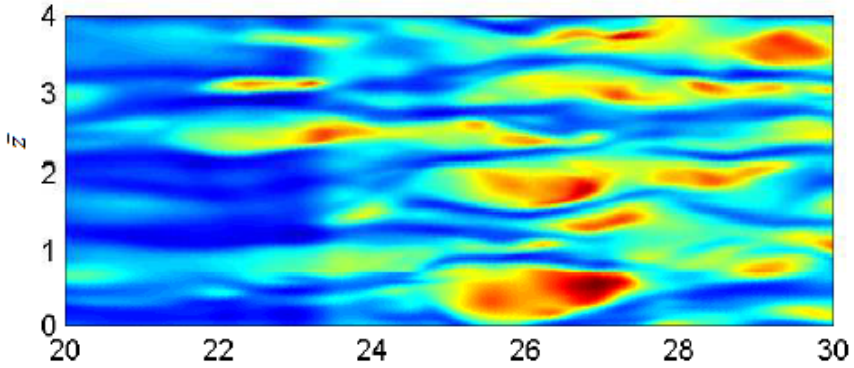

(a) Instantaneous streamwise fluid velocity

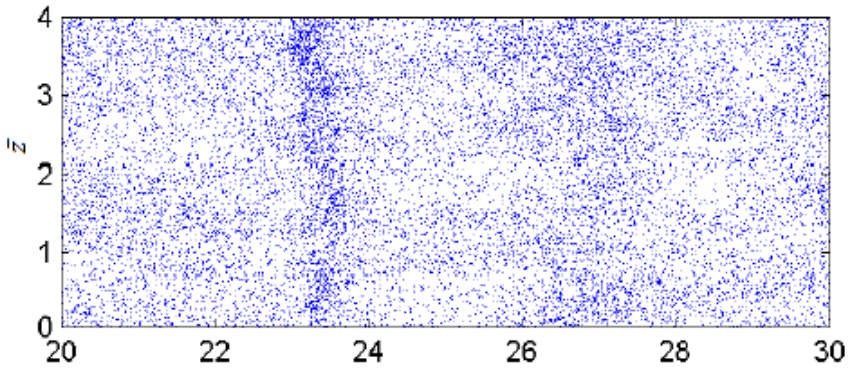

(b) $\tau_p^+ = 28$

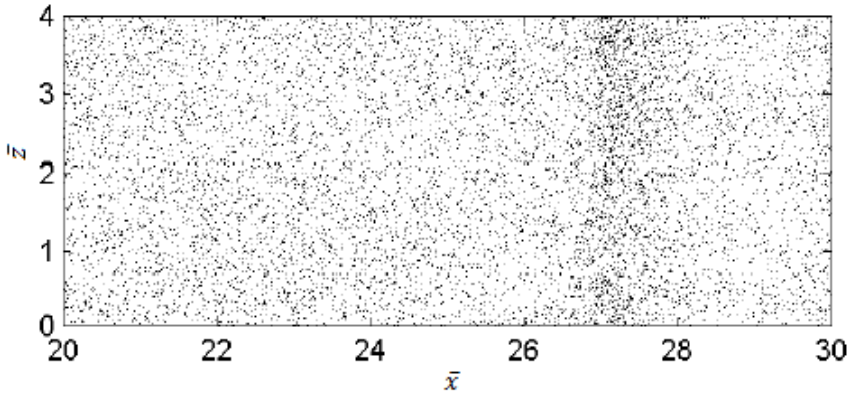

(c) $\tau_p^+ = 112$

Figure 29. Instantaneous particle distribution with collisions at $y^+ = 5$

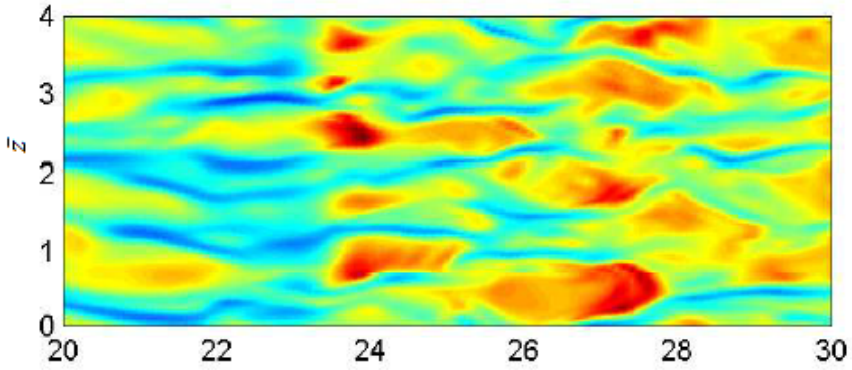

(a) Instantaneous streamwise fluid velocity

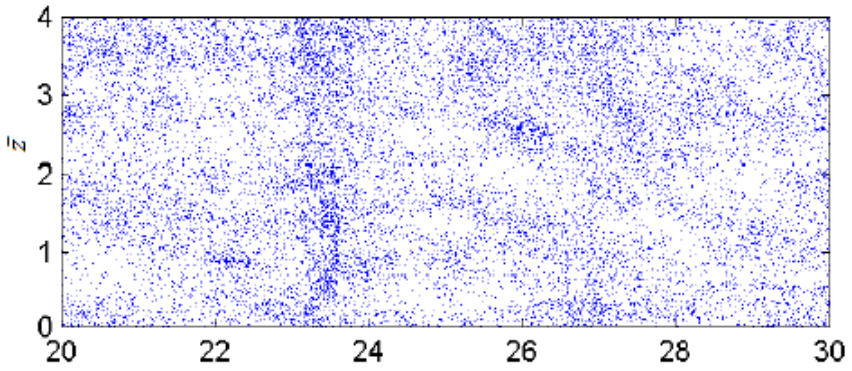

(b) $\tau_p^+ = 28$

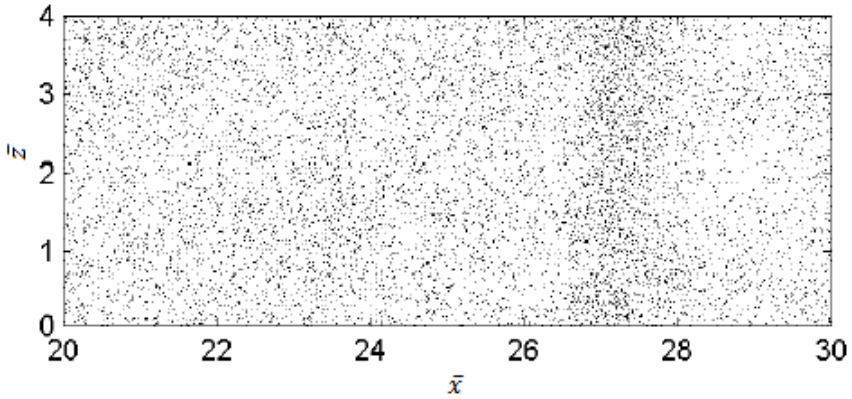

(c) $\tau_p^+ = 112$

Figure 30. Instantaneous particle distribution with collisions at $y^+ = 20$

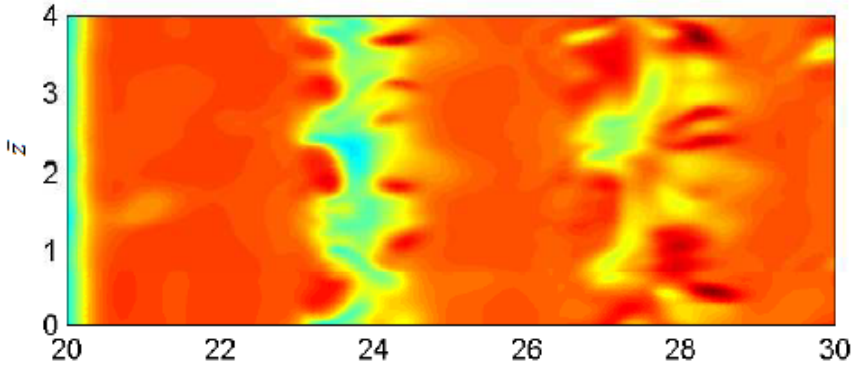

(a) Instantaneous streamwise fluid velocity

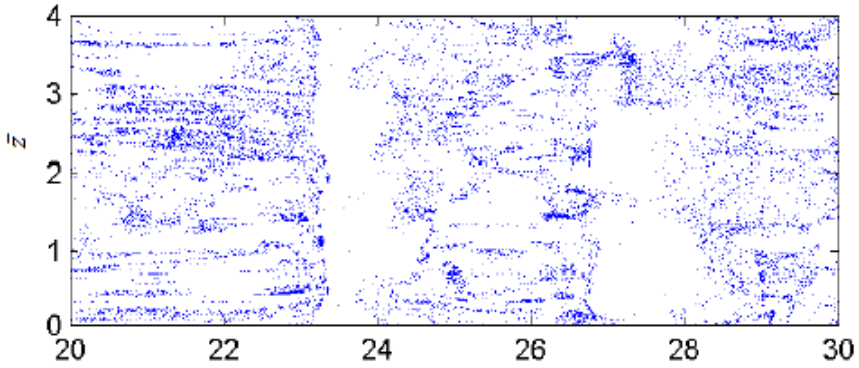

(b) $\tau_p^+ = 28$

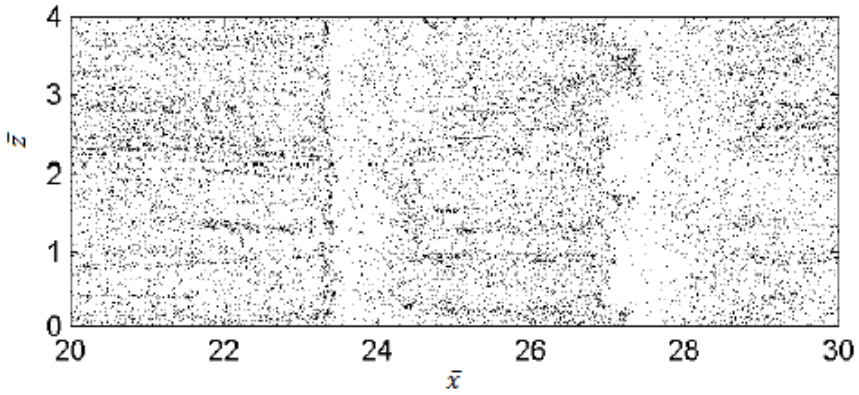

(c) $\tau_p^+ = 112$

Figure 31. Instantaneous particle distribution with collisions at $y^+ = 175$

wall-normal direction as expected since the particles are actively being pulled in the direction of the wall. The cases with gravity have larger particle concentrations near the wall and the particles are not dispersing as much as the simulations that do not include gravity.

The profiles near the inlet are less smooth since the particles are reinitialized at the inlet and randomly distributed across the domain. The random distribution of particles does not readjust before the sampling occurs at $\overline{x} = 20$ and show statistical bias. The turbulent boundary layer cases without collisions have seen the particles migrate distances of over 100% of the initial seeding. The further downstream the further the particles have dispersed throughout the domain. The lighter particles have not dispersed as much as the denser particles for any given simulation without inter-particle collisions. The cases with the vortices have seen the particles migrate as much as 300% of the initial seeding length. On average the vortex disperses the particles nearly twice as far compared to simulations without the vortices. The simulations with collisions have more uniform particle distributions with gravity increasing the particle concentration near the wall. In addition these cases have seen the number density near $\overline{y} = 5$ decrease as the number density near the lower wall rises, the number density at the top decreases. The decrease is is slower for the simulations including vortices because the vortices compete against the gravitational force.

In addition to the wall-normal profiles, streamwise profiles of the number of particles at a given plane are also shown. Since the bins are homogenous along the

streamwise dimension, Figures (36)-(41) show the number of particles at the bin as opposed to the number density. At the wall, the number of particles is relatively small initially but as the simulation progresses the collection of particles at the wall increases dramatically for the cases without collisions. The increase is particularly substantial for the cases with gravity where the particle concentration has increased by two orders of magnitude. Also the light particle concentration is larger at the wall with or without collisions as seen previously in the instantaneous particle distribution. With inter-particle collisions active, the overall number of particles is decreased. For these cases the increase in particles near the wall is not as substantial given the effect of collisions which maintain more uniformity and prevent the preferential concentration of particles at the wall. Even at the wall the semblance of the vortex is apparent and quite distinguishable though not as obvious in cases with collisions.

Further away from the wall at $y^+ \approx 170$, the initial distribution contains a greater number of particles. As the simulation progresses the number of particles at this location has decreased when compared to the initial distribution. Given the substantial increase of particles near the wall, other locations in the domain necessarily undergo a decrease in the number of particles. At this location the concentration of heavier particles is slightly larger for the cases without collisions. Meanwhile the cases with collisions remain mostly uniform in the number of particles compared to the initial distribution even with the gravitational effect on the particles. Close to the center of the domain at $y^+ \approx 360$, the simulations without collisions are

not initially seeded. The simulations with the vortex are more efficient at dispersing the particles throughout the computational domain. The TBL also disperses particles toward the outer flow, albeit, not as efficiently. Additionally the gravitational settling of the particles restricts the dispersal of the particles but does not completely impede the particle flux away from the wall. For the simulations with collisions, again the distribution is relatively uniform compared to the initial distribution, however the addition of gravity creates non-uniformity particularly for the lighter particle group.

The next set of plots in Figure (42) shows the collision frequency of the particles. The collision frequency shown is the total number of particle collisions divided by the simulation time averaged into a single profile. In all cases the lighter particles have more frequent collisions near the wall given the larger particle concentrations. In the cases with gravity the collision frequency near the wall for the light particles is close to 5 times larger compared to the cases without gravity. Gravitational settling increases the collision frequency significantly in the boundary layer. At locations above the boundary layer the effect of gravity in increasing the collision frequency is not as considerable. The vortex impacts the frequency of collisions in the near wall region, however the vortex effect is stronger in promoting the occurrence of collisions in the outer flow. For the TBL, collisions for light and heavy particles do not exceed $\overline{y} \approx 2$ and $\overline{y} \approx 3$ respectively. Meanwhile the vortex increases the occurrence of collisions to $\overline{y} \approx 3.5$ and $\overline{y} \approx 5$ for light and heavy particles respectively. The mixing of the particles induced by the vortex increases

the opportunity of particles colliding and results in greater collision frequency in the outer flow.

The Inter-particle collision time is shown in Figure (43). The figure shows the average time interval between collisions along the wall-normal direction. The time is shown in viscous units to directly compare to the particle response times of the particle groups shown as horizontal lines. As expected from the collision frequency, the time interval near the wall is small and decreases away from the wall. Also the time interval is smaller for the light particle near the wall, however away from the wall the time interval for the heavier particle is smaller. The gravitational settling of the particles, produces more frequent collisions which results in reduced time intervals when compared to cases without gravity. Additionally, the vortex increases mixing of the particles and reduces the time between collisions in the outer flow. The particle response time was also included in the figure to compare between the particle response time and the time interval between collisions. For the light particle the response time usually exceeds the collision time except very near the wall with gravity enabled. The heavy particles have a smaller collision time interval surrounding the boundary layer area. The heavy particles are sensitive to the effects of collisions near the wall. Even though the light particle response time is smaller than the interval between collisions, the effect of collisions is significant near the wall as shown in subsequent figures.

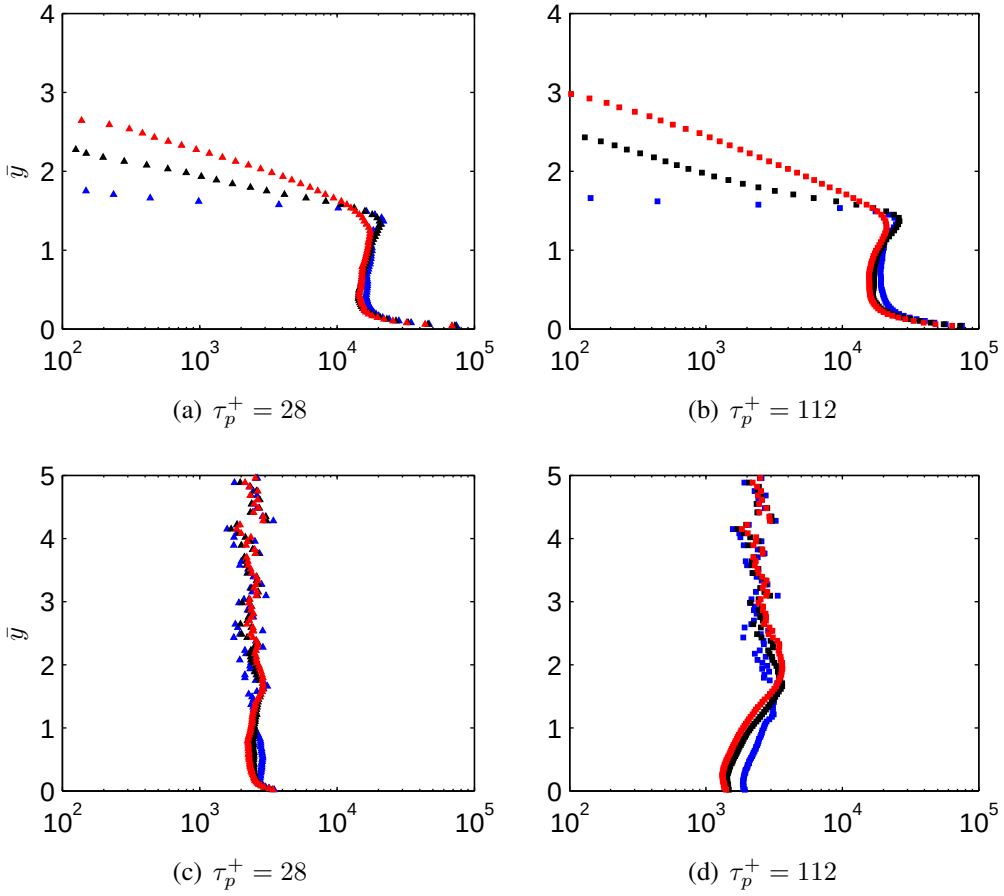

(a) $\tau_p^+ = 28$ (b) $\tau_p^+ = 112$

(c) $\tau_p^+ = 28$ (d) $\tau_p^+ = 112$

Figure 32. Number density TBL without gravity.
Blue: $\overline{x} = 20$, *Black*: $\overline{x} = 40$, *Red*: $\overline{x} = 60$
Top: *no collision*, *Bottom*: *with collision*

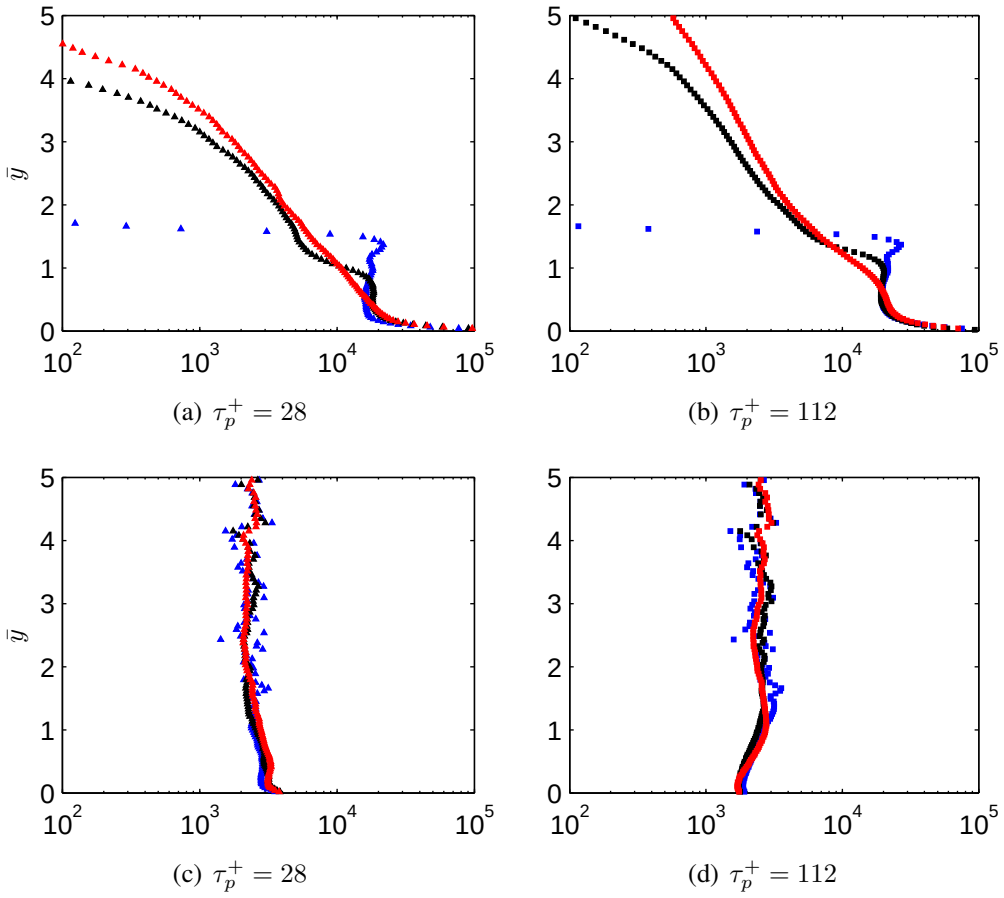

(a) $\tau_p^+ = 28$ (b) $\tau_p^+ = 112$

(c) $\tau_p^+ = 28$ (d) $\tau_p^+ = 112$

Figure 33. Number density V-TBL without gravity.
Blue: $\overline{x} = 20$, *Black*: $\overline{x} = 40$, *Red*: $\overline{x} = 60$
Top: *no collision*, *Bottom*: *with collision*

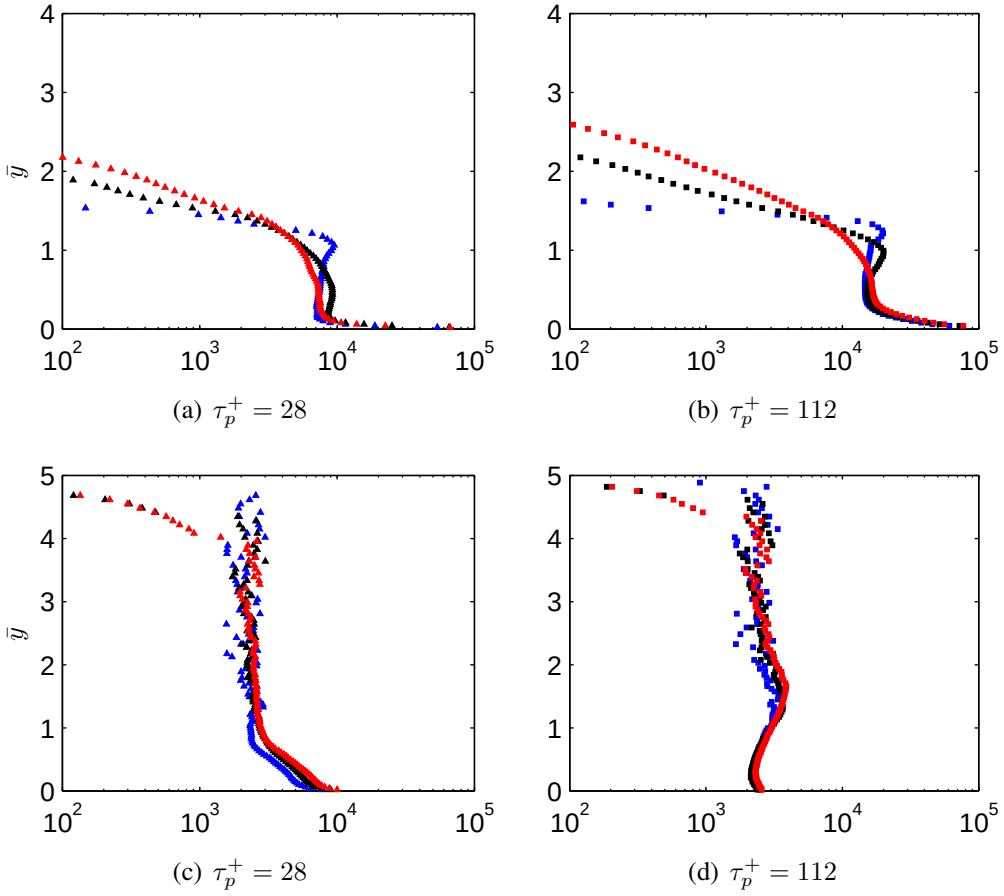

(a) $\tau_p^+ = 28$ (b) $\tau_p^+ = 112$

(c) $\tau_p^+ = 28$ (d) $\tau_p^+ = 112$

Figure 34. Number density TBL with gravity.
Blue: $\overline{x} = 20$, *Black*: $\overline{x} = 40$, *Red*: $\overline{x} = 60$
Top: *no collision*, *Bottom*: *with collision*

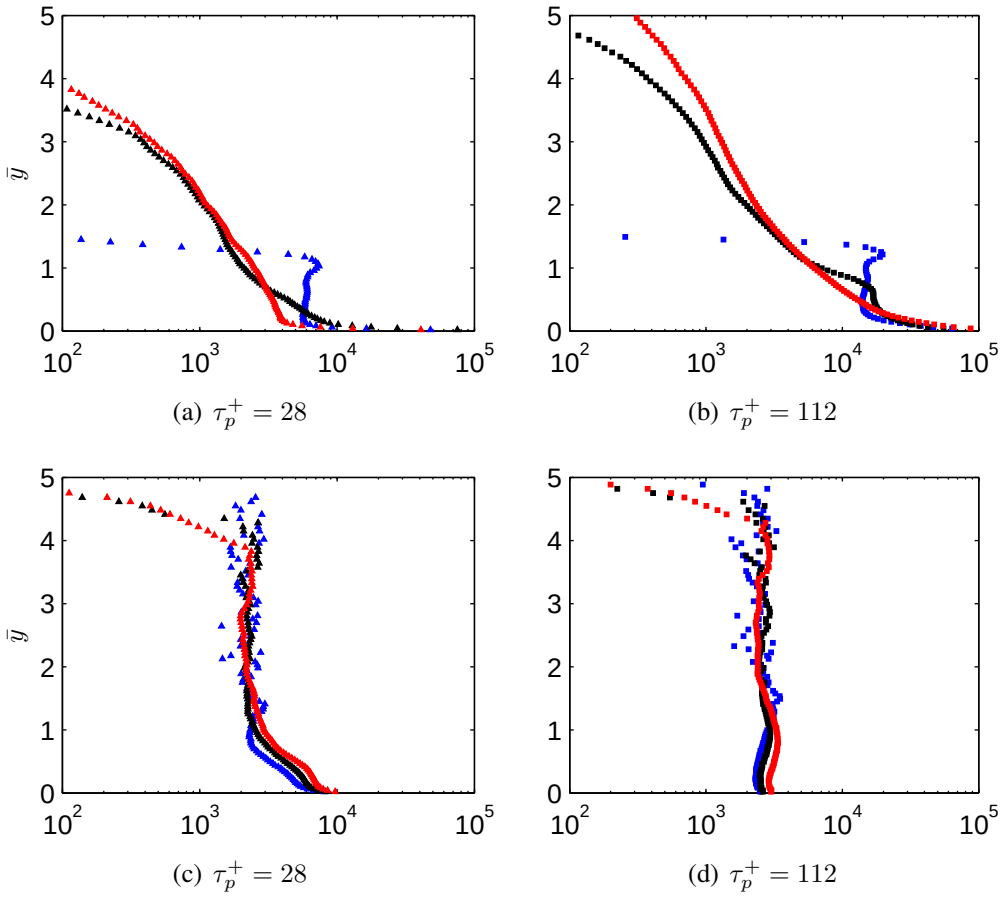

(a) $\tau_p^+ = 28$ (b) $\tau_p^+ = 112$

(c) $\tau_p^+ = 28$ (d) $\tau_p^+ = 112$

Figure 35. Number density V-TBL with gravity.
Blue: $\overline{x} = 20$, *Black*: $\overline{x} = 40$, *Red*: $\overline{x} = 60$
Top: *no collision*, *Bottom*: *with collision*

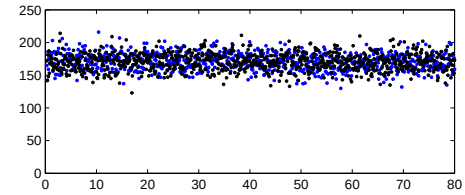

(a) Initial distribution

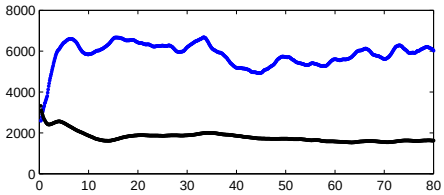

(b) TBL without gravity

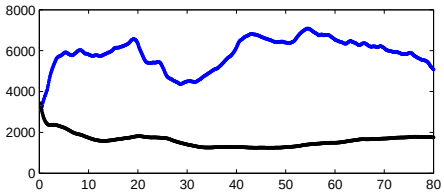

(c) V-TBL without gravity

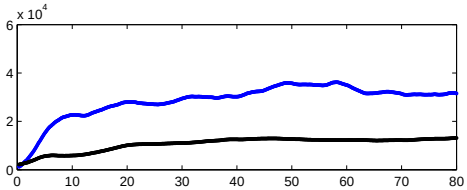

(d) TBL with gravity

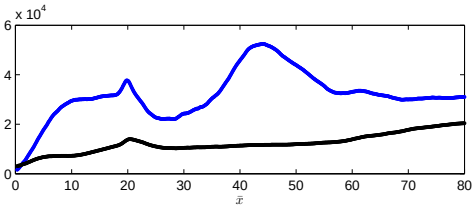

(e) V-TBL with gravity

Figure 36. Number of particles at wall without collisions.
Blue: $\tau_p^+ = 28$, *Black*: $\tau_p^+ = 112$

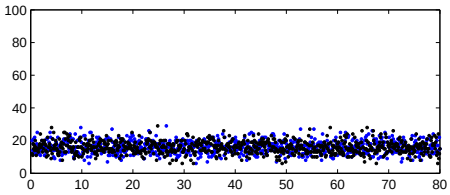

(a) Initial distribution

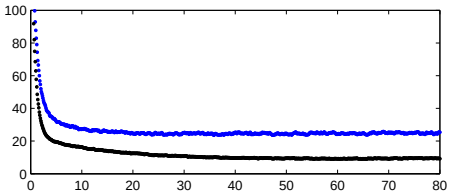

(b) TBL without gravity

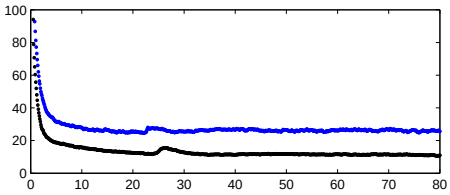

(c) V-TBL without gravity

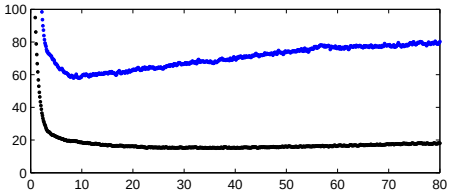

(d) TBL with gravity

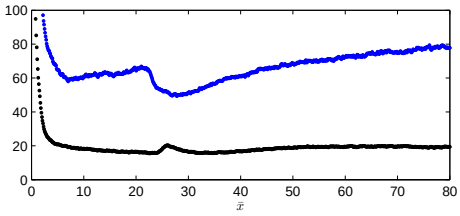

(e) V-TBL with gravity

Figure 37. Number of particles at wall with collisions.
Blue: $\tau_p^+ = 28$, *Black*: $\tau_p^+ = 112$

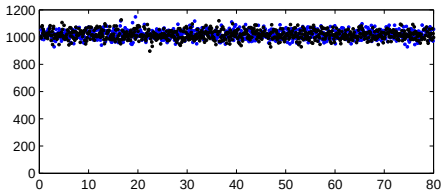

(a) Initial distribution

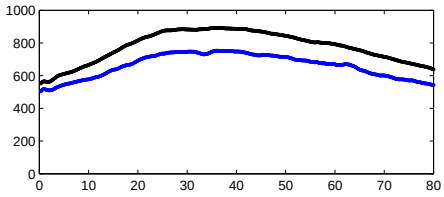

(b) TBL without gravity

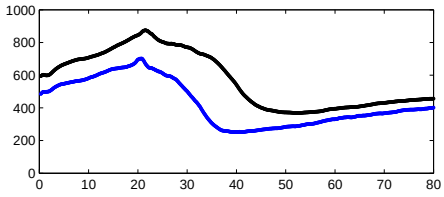

(c) V-TBL without gravity

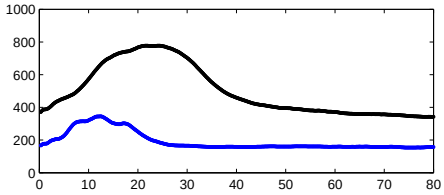

(d) TBL with gravity

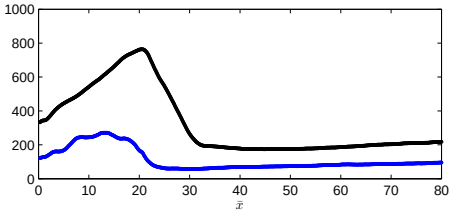

(e) V-TBL with gravity

Figure 38. Number of particles at $y^+ \approx 170$ without collisions. *Blue*: $\tau_p^+ = 28$, *Black*: $\tau_p^+ = 112$

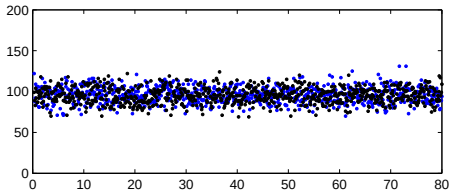

(a) Initial distribution

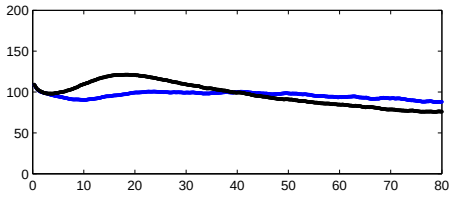

(b) TBL without gravity

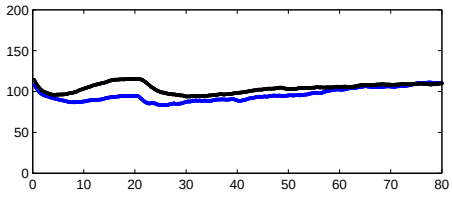

(c) V-TBL without gravity

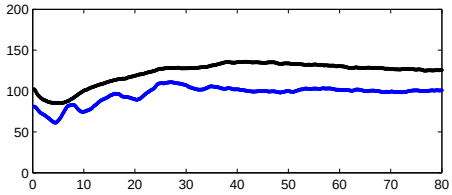

(d) TBL with gravity

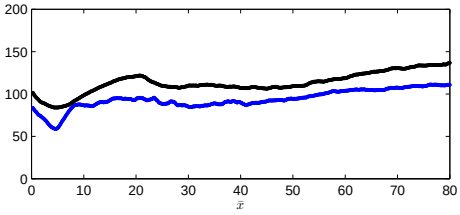

(e) V-TBL with gravity

Figure 39. Number of particles at $y^+ \approx 170$ with collisions. *Blue*: $\tau_p^+ = 28$, *Black*: $\tau_p^+ = 112$

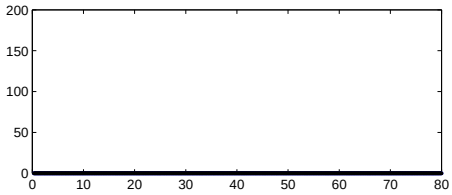

(a) Initial distribution

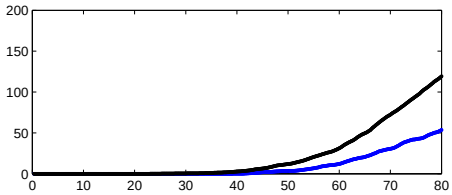

(b) TBL without gravity

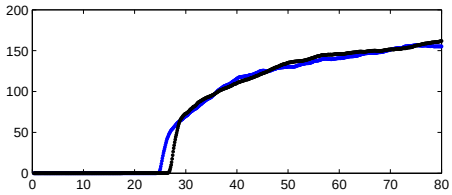

(c) V-TBL without gravity

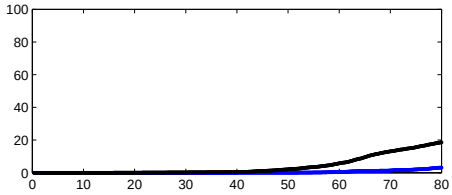

(d) TBL with gravity

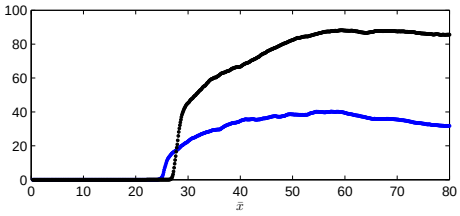

(e) V-TBL with gravity

Figure 40. Number of particles at $y^+ \approx 360$ without collisions. *Blue*: $\tau_p^+ = 28$, *Black*: $\tau_p^+ = 112$

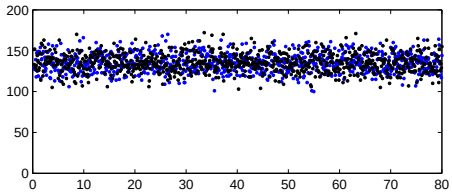

(a) Initial distribution

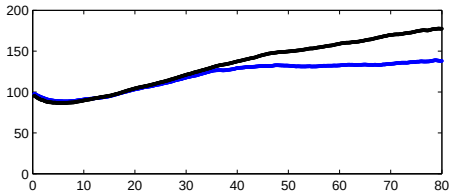

(b) TBL without gravity

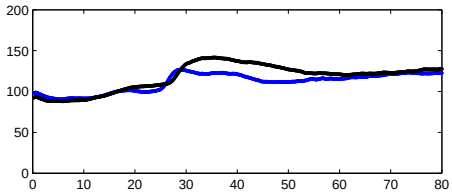

(c) V-TBL without gravity

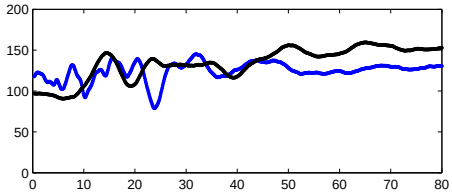

(d) TBL with gravity

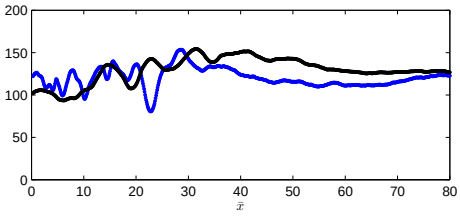

(e) V-TBL with gravity

Figure 41. Number of particles at $y^+ \approx 360$ with collisions. *Blue*: $\tau_p^+ = 28$, *Black*: $\tau_p^+ = 112$

The mean streamwise particle velocity is shown on Figures(44)-(47) for different streamwise locations. The fluid velocity shown is the undisturbed fluid velocity computed during the gas phase solution. The profiles are normalized with the fluid friction velocity, u_τ. For the cases without vortices, the streamwise velocity along the domain tends to slightly decrease in magnitude along the streamwise direction. The case with vortices displays significant effect of the vortex in the area surrounding the vortex introduction. At distances away from the point of vortex introduction, the flow begins a reversal to the undisturbed flow. The inclusion of particle-particle collisions shows that there is a strong effect of collisions on the wall-normal profiles of the particle velocity with increasing Stokes number [17]. The effect of collisions is very strong near the wall along the entire domain as seen on the higher magnitude of the velocities for both particle groups, particularly for the denser particles. The streamwise velocity for the particles with collisions results in a more uniform velocity profile, particularly for the denser particle which exhibit a velocity near the wall which is comparable to the particle velocity at the outer flow. The values near the wall for the particle velocity show that there is a slip condition between the particle mean velocity and the wall, which agrees with the elastic bouncing of particles on the wall. The vortices have a significant impact in the evolution of the particle velocity as seen on the different profiles. Initially near the inlet both cases are identical, that is both are turbulent boundary layers, however at locations beyond $\overline{x} = 20$ where the vortices are introduced, the vortices have an obvious effect on the particles. As the particles travel downstream and the vortices lose coherence

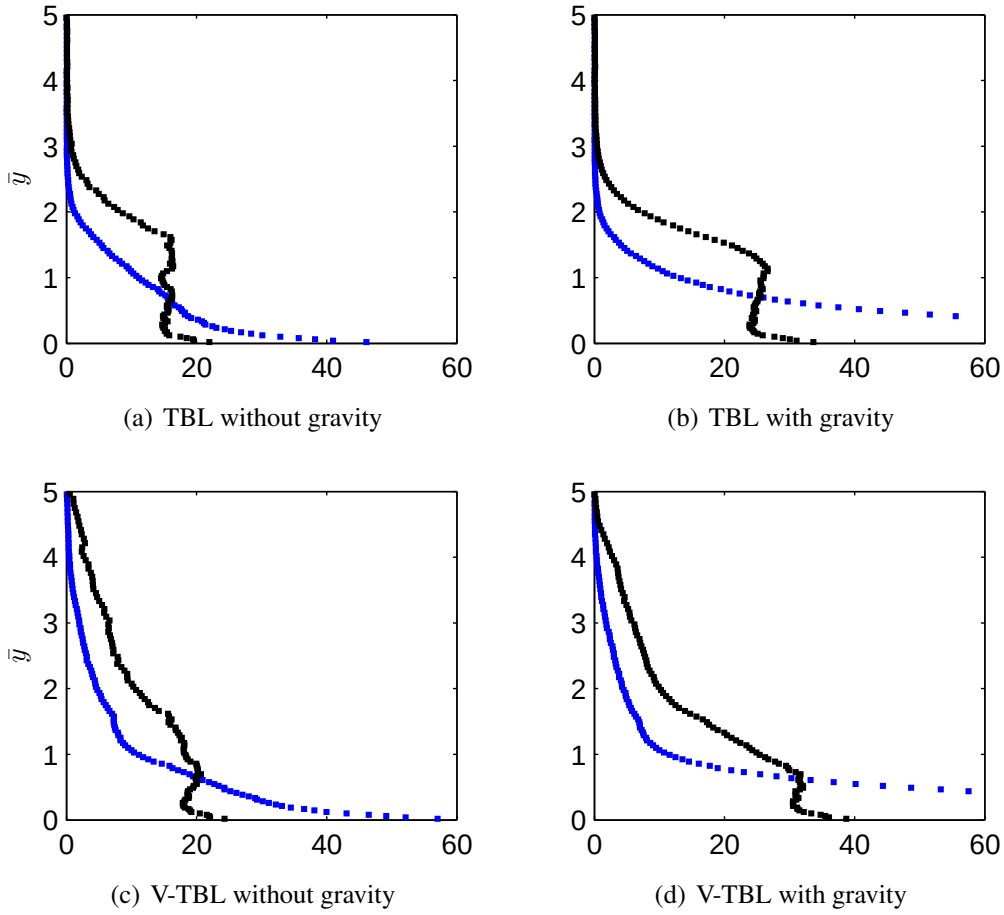

(a) TBL without gravity

(b) TBL with gravity

(c) V-TBL without gravity

(d) V-TBL with gravity

Figure 42. Collision frequency.
Blue: $\tau_p^+ = 28$, *Black*: $\tau_p^+ = 112$

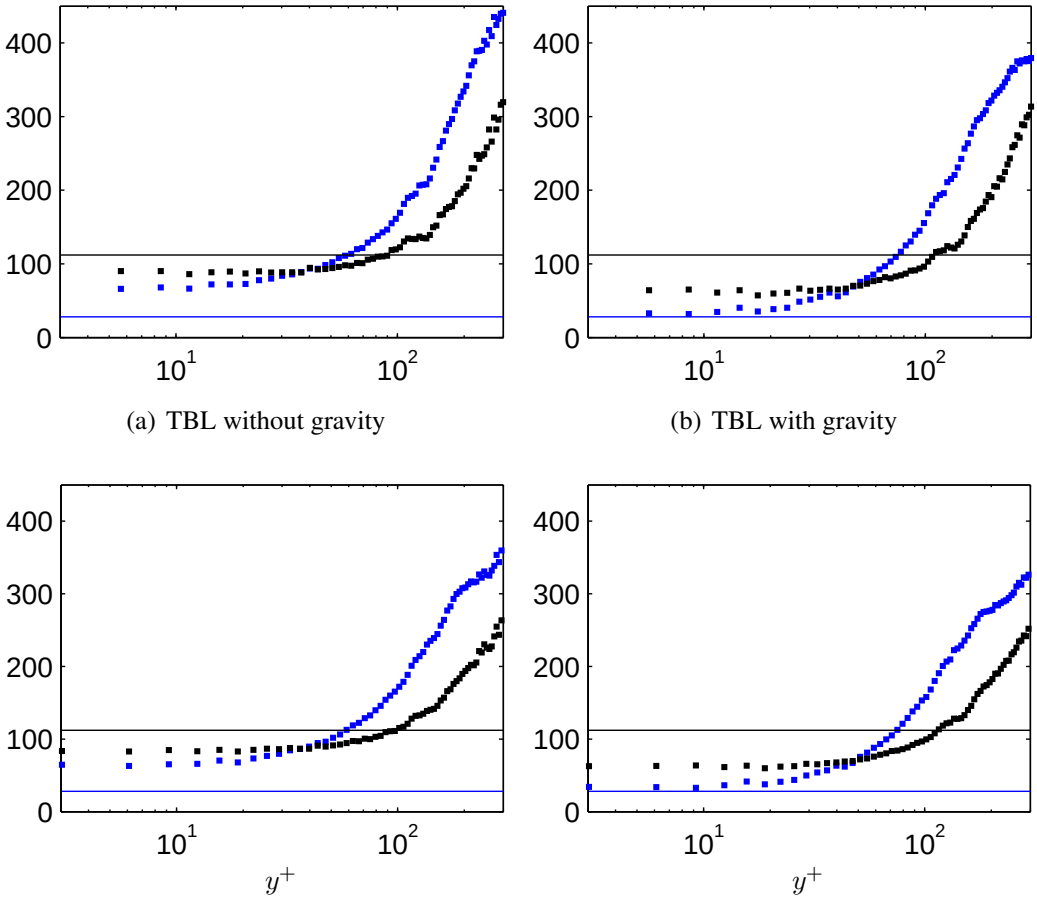

(a) TBL without gravity

(b) TBL with gravity

(c) V-TBL without gravity

(d) V-TBL with gravity

Figure 43. Inter-particle collision time interval.
— *particle response time*, □ *collision time*.
Blue: $\tau_p^+ = 28$, *Black*: $\tau_p^+ = 112$

the particles begin to reverse back into an equilibrium state that resembles the inlet conditions. The effect of the vortices is strong between $25 < \overline{x} < 50$ as opposed to the effect of inter-particle collisions which remains in effect through the entire length of the computational domain. The addition of gravity has a greater impact on the simulations without inter-particle collisions particularly the lighter particles. In the cases without gravity the velocities between the lighter and heavier particles without collisions is clear, however with the inclusion of gravity the velocities of the particles become of similar magnitude.

The particle relative velocity, v_r is the difference between the particle velocity and the interpolated fluid velocity at the particle position. Figure (48) shows the particle relative velocity normalized with the fluid friction velocity, u_τ at $\overline{x} = 20$. For all cases, the relative velocity of the denser particle including collisions is almost an order of magnitude larger in value very near the wall. In the absence of vortices and gravitational settling, the light particles with collisions and the denser particles without collisions have similar values in the near wall region. In addition, the light particles without collisions have a streamwise velocity that is very close to the fluid velocity which results in a particle relative velocity that is close to zero. When the particles experience gravity, the light particles without collisions achieve a relative velocity that is of similar value as the heavier particles without collisions. Naturally, the vortex induces a dramatic perturbation in the fluid velocity which results in negative values for the particle relative velocity. Even though the vortex is introduced at the edge of the boundary layer, $\overline{y} \approx 1$ the vortex affects the particles

in the near wall region as evidenced by the slightly higher particle relative velocity magnitude when compared to turbulent flow without the vortex.

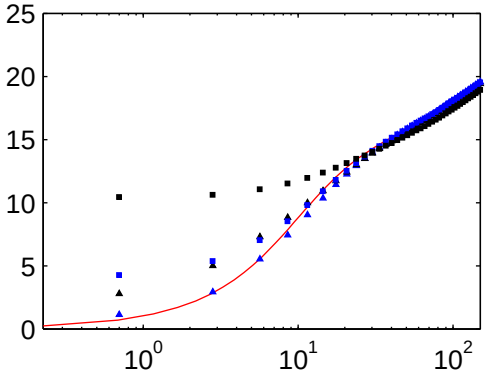

(a) $\overline{x} = 20$

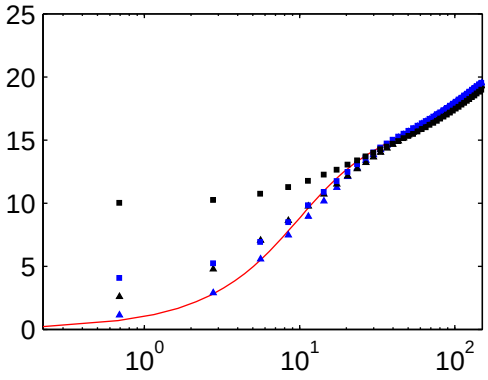

(b) $\overline{x} = 30$

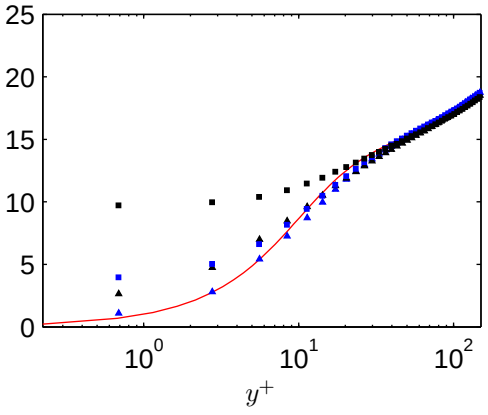

(c) $\overline{x} = 60$

Figure 44. TBL: streamwise velocity without gravity.
— $fluid$, △ $no\ coll$, □ $with\ coll$.
$Blue$: $\tau_p^+ = 28$, $Black$: $\tau_p^+ = 112$

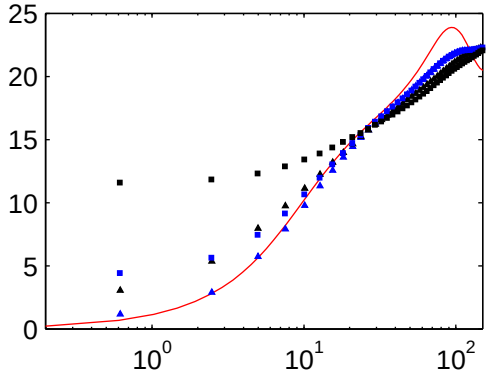

(a) $\overline{x} = 20$

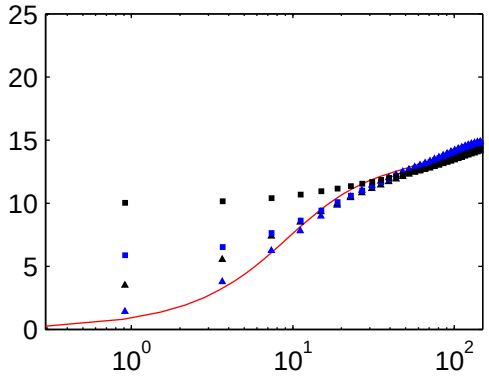

(b) $\overline{x} = 30$

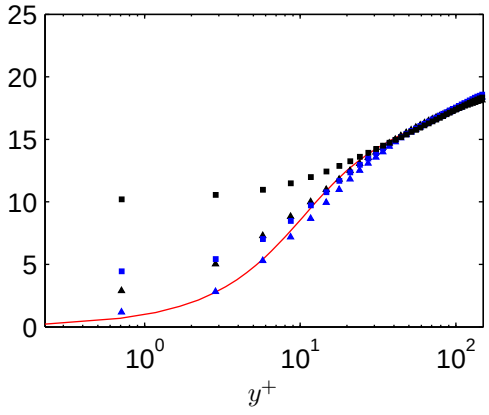

(c) $\overline{x} = 60$

Figure 45. V-TBL: streamwise velocity without gravity.
— $fluid$, △ $no\ coll$, □ $with\ coll$.
$Blue$: $\tau_p^+ = 28$, $Black$: $\tau_p^+ = 112$

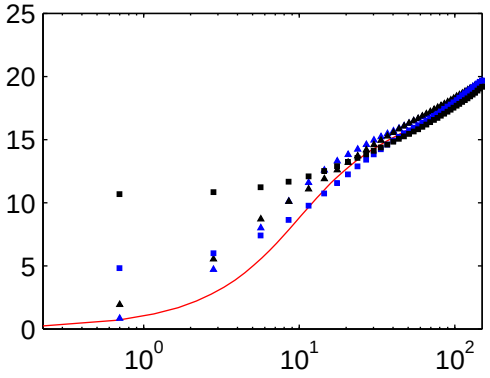

(a) $\overline{x} = 20$

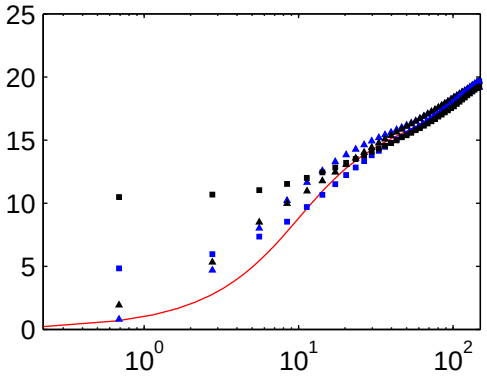

(b) $\overline{x} = 30$

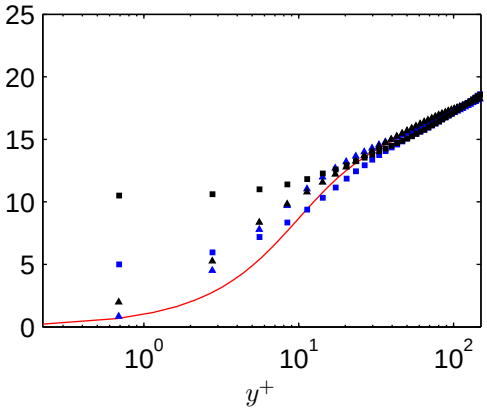

(c) $\overline{x} = 60$

Figure 46. TBL: streamwise velocity with gravity.
— *fluid*, △ *no coll*, □ *with coll*.
Blue: $\tau_p^+ = 28$, *Black*: $\tau_p^+ = 112$

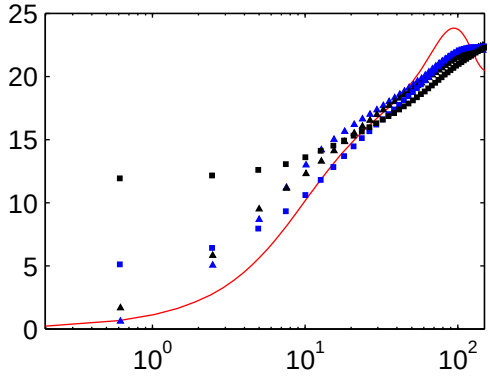

(a) $\overline{x} = 20$

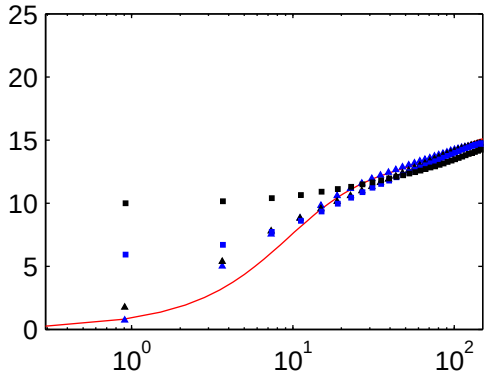

(b) $\overline{x} = 30$

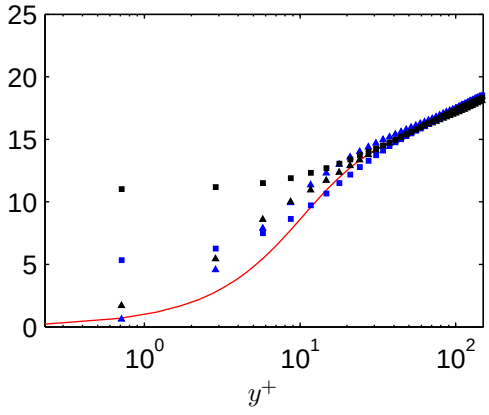

(c) $\overline{x} = 60$

Figure 47. V-TBL: streamwise velocity with gravity.
— *fluid*, △ *no coll*, □ *with coll*.
Blue: $\tau_p^+ = 28$, *Black*: $\tau_p^+ = 112$

The streamwise, wall-normal, and spanwise root mean square(RMS) velocity of the particles and fluid is shown in Figures (49)-(60) at different streamwise locations. The RMS velocity of the fluid and particles is defined as

$$\begin{aligned} \langle u_i' u_i' \rangle &= \sqrt{\overline{u_i u_i} - \overline{u_i}\,\overline{u_i}} \\ \langle v_i' v_i' \rangle &= \sqrt{\overline{v_i v_i} - \overline{v_i}\,\overline{v_i}}. \end{aligned} \tag{38}$$

The fluid RMS velocity is the undisturbed fluid velocity computed on the fluid grid. Once again, the variation in the turbulent boundary layer simulation is subtle at different locations along the domain, although for increasing values of $\overline{x}$ the tail end of the RMS velocity is increasing for all three directions. The flow with vortices shows clear variations along different locations on the domain. At $\overline{x} = 10$, before the vortices are introduced, the profiles for both types of flows are very similar for each of the three components of the RMS velocity. Then as the flow progresses and vortices are introduced, the RMS velocity away from the wall increases due to the perturbations of the vortices as seen on $\overline{x} = 40$. The perturbation on the RMS velocity is more apparent in the wall-normal and spanwise direction, while the streamwise RMS velocity seems to only be affected very near the wall. As the vortices lose coherence, the RMS velocity begins to resemble the undisturbed state as seen on the profile for $\overline{x} = 70$. Though not quite completely recovered yet, the flow is transitioning to the undisturbed state as seen on the progression from the figures. The RMS velocity for the particles at the wall is non-zero due to the

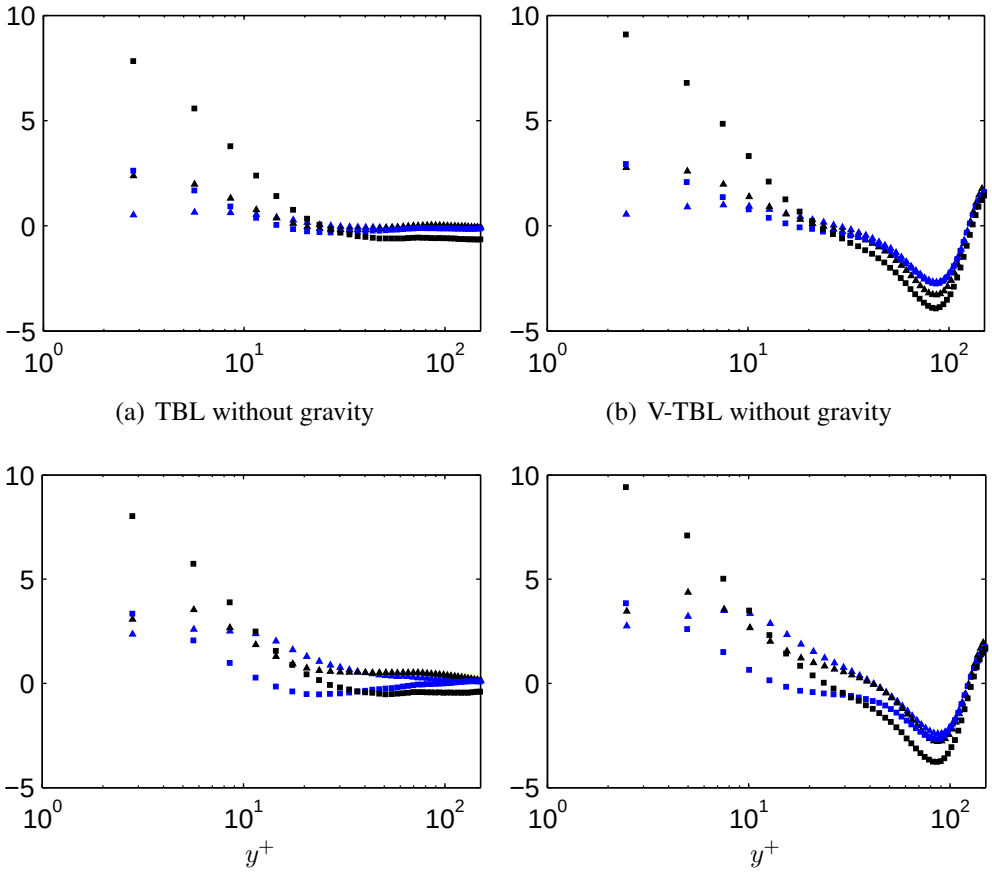

(a) TBL without gravity

(b) V-TBL without gravity

(c) TBL with gravity

(d) V-TBL with gravity

Figure 48. Streamwise particle relative velocity at $\overline{x} = 20$
$\triangle$ *no coll*, $\square$ *with coll*.
Blue: $\tau_p^+ = 28$, *Black*: $\tau_p^+ = 112$

inelastic collisions at the lower wall.

For the cases without collisions, both particle groups have larger wall-normal and spanwise RMS velocity away from the wall with the lighter particle group having larger values of the RMS velocity. For cases with collisions enabled, both particle groups have an increase in magnitude, however the larger inertia particles undergo a more significant increase due to the particle collisions which are more common for the denser particles. In addition without inter-particle collisions, the wall-normal and spanwise RMS curves tend to increase in magnitude away from the wall and then slowly decrease with the exception of $\overline{x} = 40$ where the vortex effect is significant and modifies the RMS velocity beyond the boundary layer. On the other hand, the cases with collisions tend to peak near the wall and then proceed with a sharp decrease, predominantly for the lighter particle group. The addition of gravity, results in higher particle concentrations near the wall which in turn increases the wall-normal and spanwise RMS velocity of the particles with collisions enabled. The increase is due to more inter-particle collisions which increase the RMS velocity of the particles. The streamwise RMS velocity variation is less pronounced when compared with the other directions. The denser particles have a peak streamwise RMS velocity at the wall and tend to decrease away from the wall while the lighter particles peak near the wall and then proceed to decrease away from the wall regardless of inter-particle collisions. Away from the wall the values for both particle groups with and without collisions is quite similar except close to the inlet where the denser particles with collisions have larger magnitude away from the

wall.

Fluid-particle correlations are shown for the different cases under consideration as well particle-particle correlations. The correlations similarly to the RMS velocity are defined as follows

$$\begin{aligned} \left\langle u_i' v_j' \right\rangle &= \sqrt{|\overline{u_i v_j} - \overline{u_i}\,\overline{v_j}|} \\ \left\langle v_i' v_j' \right\rangle &= \sqrt{|\overline{v_i v_j} - \overline{v_i}\,\overline{v_j}|}. \end{aligned} \tag{39}$$

The particle-particle correlation $\langle v_2' v_2' \rangle$ is sensitive to inter-particle collisions as seen in the peak values near the wall, particularly the denser particle group for which the change is quite dramatic as seen on Figures (61) and (62). Also with collisions enabled the particles have higher values than the fluid-particle correlation $\langle u_2' v_2' \rangle$, whereas without collisions the values are similar. The addition of the vortex is particularly efficient at raising the correlation values for both the particles and the fluid in the outer flow as well as an observable increase very near the wall. Across both flows without collisions the behavior is analogous and the particle-particle correlation is similar to the fluid-particle correlation. With collisions enabled the near wall values for $\langle v_2' v_2' \rangle$ increase significantly for both particles. The light particles tend to follow the fluid-particle correlation at distances close to and beyond the edge of the boundary layer while the heavier particles do not follow this trend. When exposed to the gravitational settling the particle concentration near the wall increases providing more opportunities for collisions. The particle-particle correla-

tion values near the wall increase particularly for the lighter particle group where a peak develops near the wall. Even for cases without collisions the gravitational settling causes a slight increase in the values of $\langle v_2' v_2' \rangle$ near the wall.

The fluid-particle correlation $\langle u_1' v_2' \rangle$ has significantly lower values than the particle-particle correlation $\langle v_1' v_2' \rangle$ across both flows and with or without collisions. The addition of collisions provides a large increase in $\langle v_1' v_2' \rangle$ near the wall. Also $\langle v_1' v_2' \rangle$ peaks near the wall and steadily decreases for all simulations. As observed previously the denser particle group is more sensitive to the inter-particle collisions in the near wall region. The fluid-particle correlation $\langle u_1' v_2' \rangle$ is sensitive to the perturbations induced by the vortex beyond the boundary layer. The addition of the vortex does not affect the evolution of $\langle v_1' v_2' \rangle$ significantly aside from increasing the amplitude of the curves. The addition of gravity increases the amplitude of the curves given the greater occurrence of collisions. The correlations demonstrate that inter-particle collisions are significant to particle-particle correlations in the near wall region while the vortices influence the fluid-particle correlations toward the edge of the boundary layer and beyond.

Lastly the particle velocity triple correlation $\langle v_2' v_2' v_2' \rangle$ is shown at $\overline{x} = 60$. Once again the effects of collisions are quite significant for both flows. In the cases without gravity, the triple correlation value remains rather small and mostly uniform particularly for the denser particle. When inter-particle collisions are enabled the magnitude of the triple correlation increase dramatically, especially for the denser particle group. The values increase only slightly with the addition of the vortex

given the location of the profiles is far from the vortex insertion. With gravity enabled, the dense particles do not exhibit a noticeable change. The lighter particles however are quite sensitive to the effect of gravitational settling, predominantly in the near wall region. From about $0 \leq \overline{y} \leq 0.5$ the light particles quite active in both cases with and without collisions, albeit with collisions active the value is large and positive while without collisions the value is large and negative. The collisions offset the gravitational settling of the particles in the near wall region due to the high concentration of particles and the increased opportunities for particle collisions.

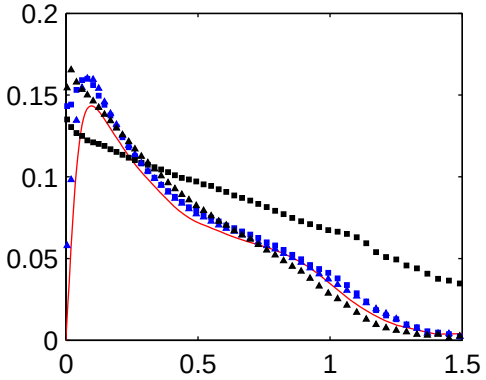

(a) $\overline{x} = 10$

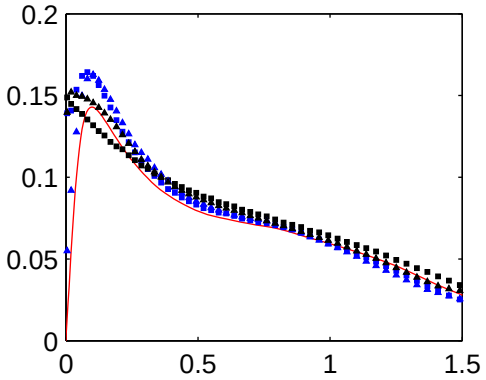

(b) $\overline{x} = 40$

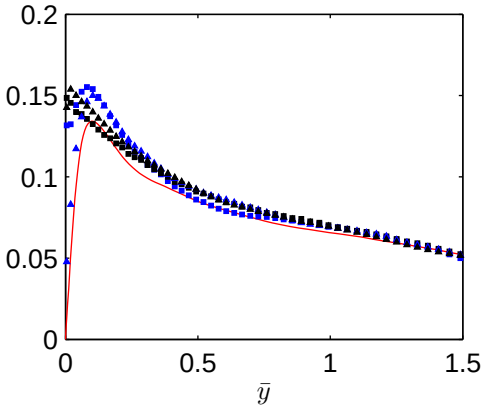

(c) $\overline{x} = 70$

Figure 49. TBL: RMS streamwise velocity without gravity.
— $fluid$, △ $no\ coll$, □ $with\ coll$.
$Blue$: $\tau_p^+ = 28$, $Black$: $\tau_p^+ = 112$

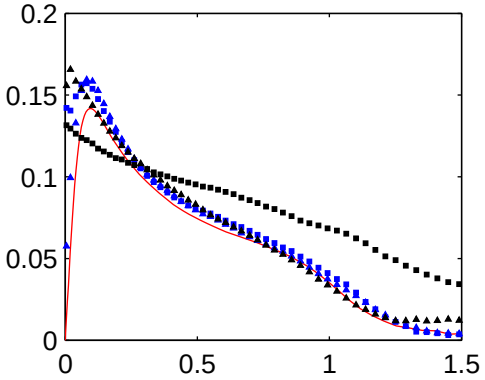

(a) $\overline{x} = 10$

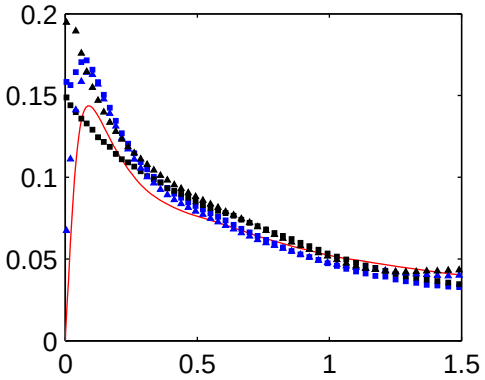

(b) $\overline{x} = 40$

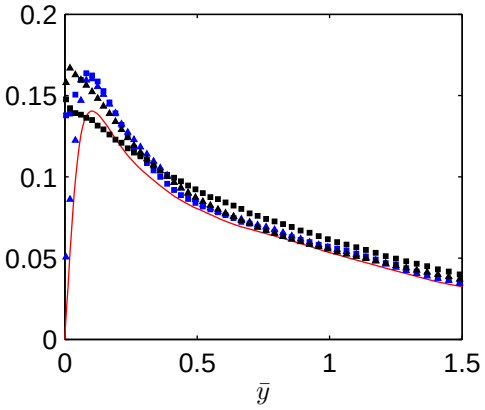

(c) $\overline{x} = 70$

Figure 50. V-TBL: RMS streamwise velocity without gravity.
— $fluid$, △ $no\ coll$, □ $with\ coll$.
$Blue$: $\tau_p^+ = 28$, $Black$: $\tau_p^+ = 112$

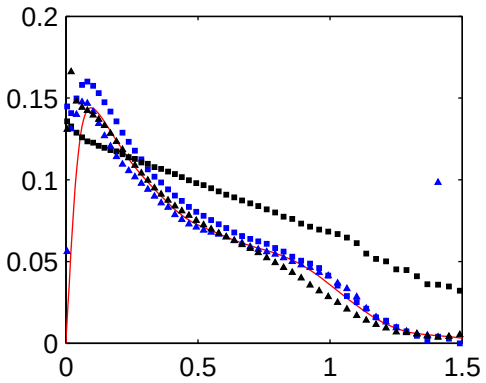

(a) $\overline{x} = 10$

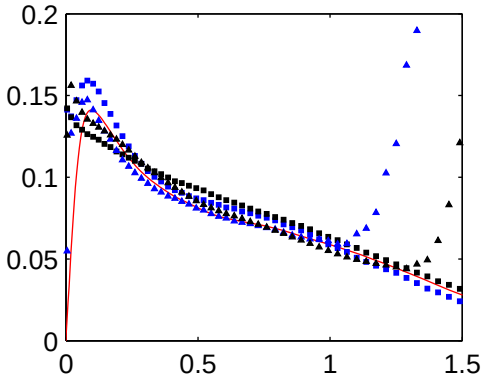

(b) $\overline{x} = 40$

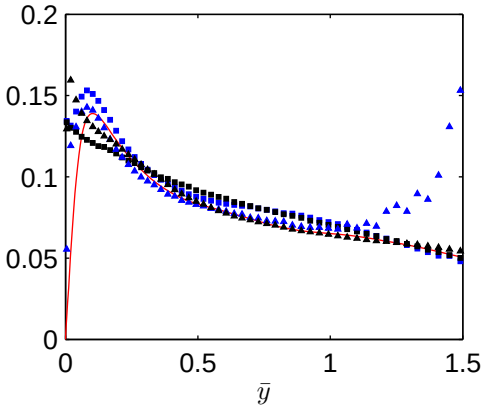

(c) $\overline{x} = 70$

Figure 51. TBL: RMS streamwise velocity with gravity.
— $fluid$, △ $no\ coll$, □ $with\ coll$.
$Blue$: $\tau_p^+ = 28$, $Black$: $\tau_p^+ = 112$

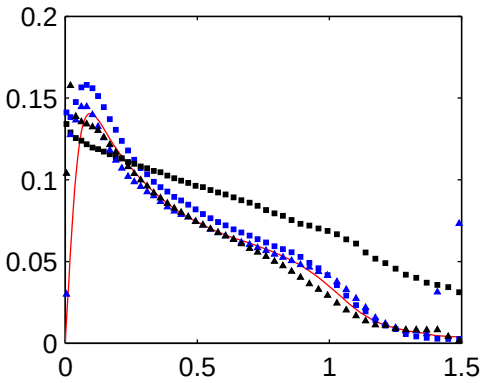

(a) $\overline{x} = 10$

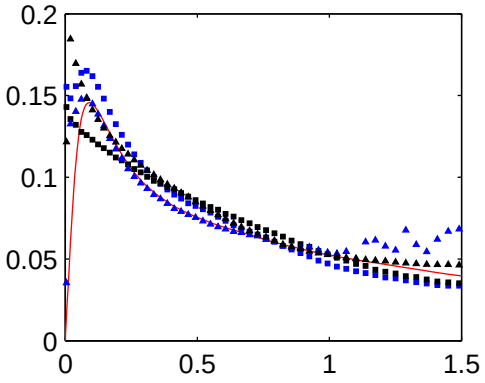

(b) $\overline{x} = 40$

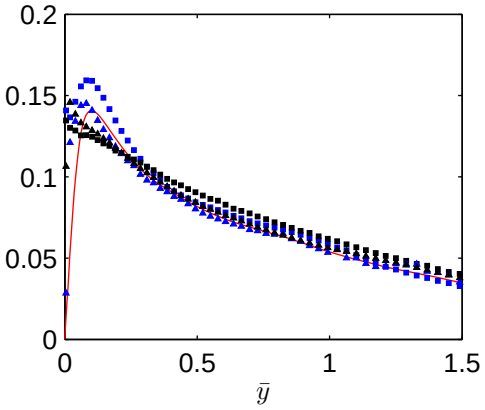

(c) $\overline{x} = 70$

Figure 52. V-TBL: RMS streamwise velocity with gravity.
— $fluid$, △ $no\ coll$, □ $with\ coll$.
$Blue$: $\tau_p^+ = 28$, $Black$: $\tau_p^+ = 112$

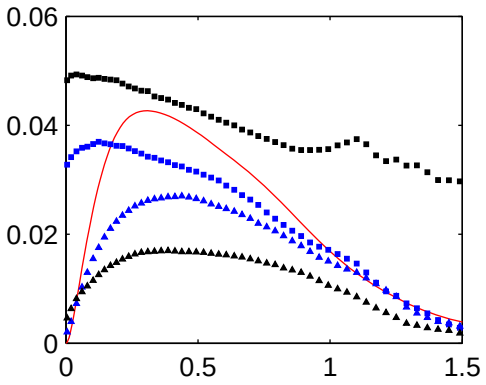

(a) $\overline{x} = 10$

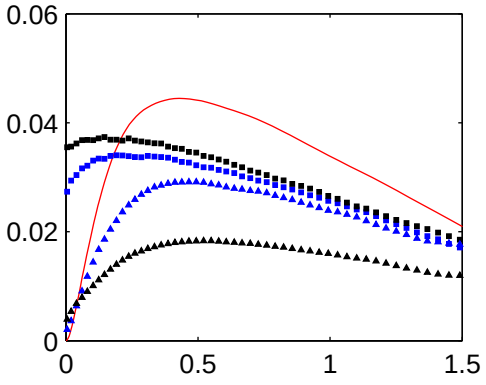

(b) $\overline{x} = 40$

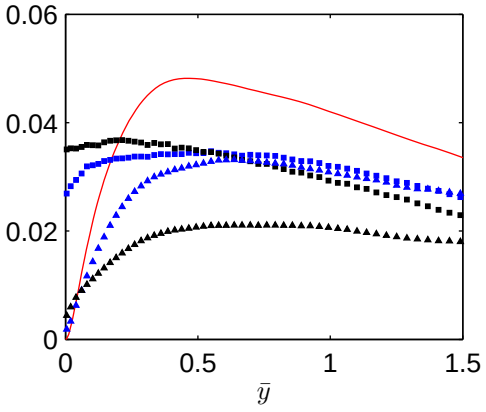

(c) $\overline{x} = 70$

Figure 53. TBL: RMS wall-normal velocity without gravity.
— *fluid*, △ *no coll*, □ *with coll*.
Blue: $\tau_p^+ = 28$, *Black*: $\tau_p^+ = 112$

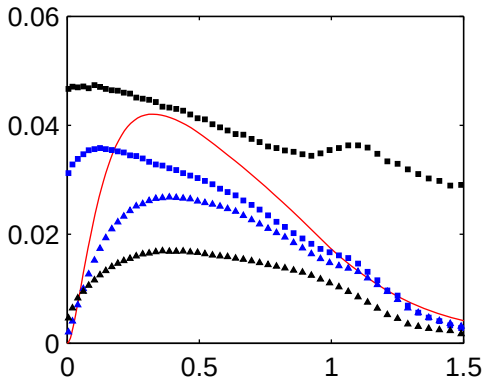

(a) $\overline{x} = 10$

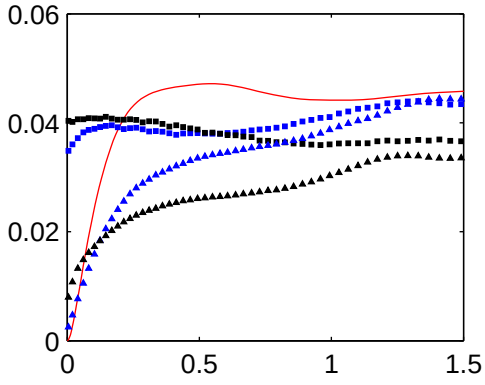

(b) $\overline{x} = 40$

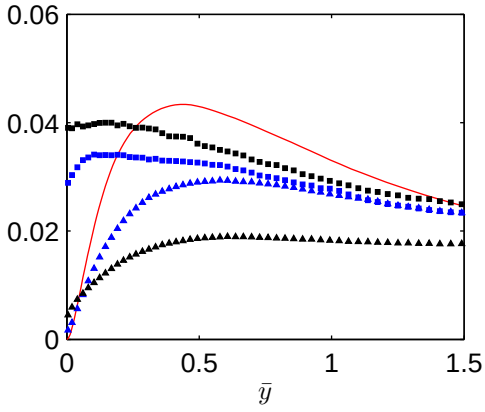

(c) $\overline{x} = 70$

Figure 54. V-TBL: RMS wall-normal velocity without gravity.
— *fluid*, △ *no coll*, □ *with coll*.
Blue: $\tau_p^+ = 28$, *Black*: $\tau_p^+ = 112$

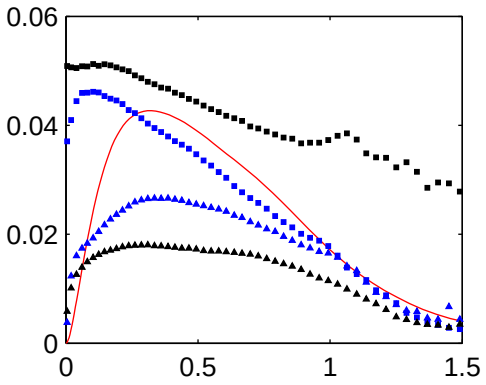

(a) $\overline{x} = 10$

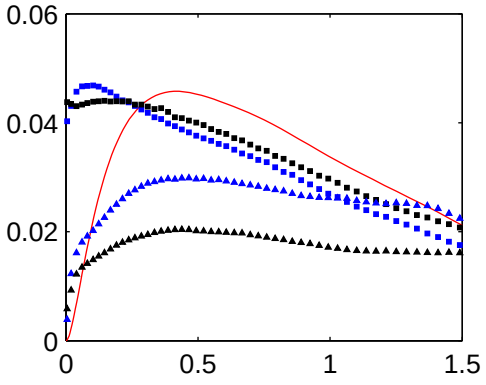

(b) $\overline{x} = 40$

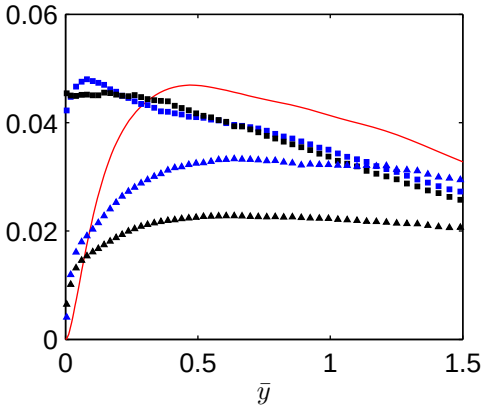

(c) $\overline{x} = 70$

Figure 55. TBL: RMS wall-normal velocity with gravity.
— *fluid*, △ *no coll*, □ *with coll*.
Blue: $\tau_p^+ = 28$, *Black*: $\tau_p^+ = 112$

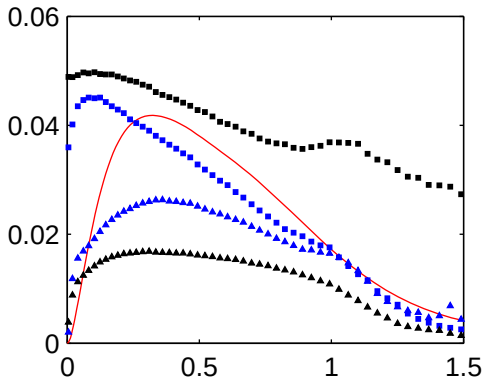

(a) $\overline{x} = 10$

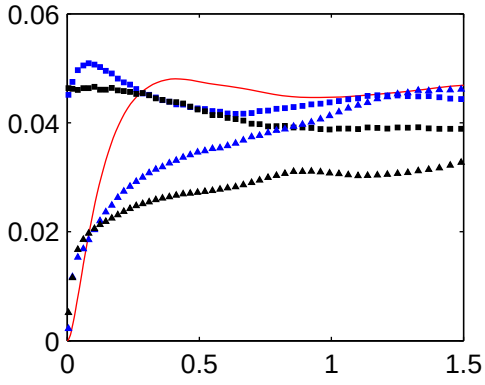

(b) $\overline{x} = 40$

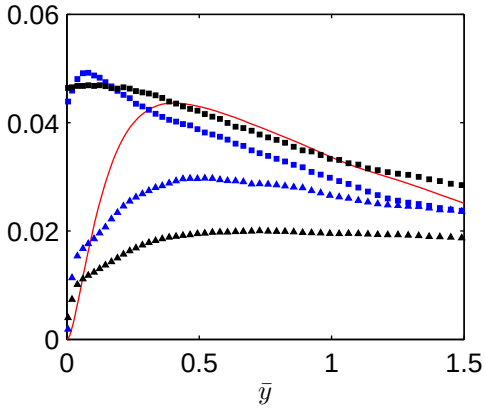

(c) $\overline{x} = 70$

Figure 56. V-TBL: RMS wall-normal velocity with gravity.
— *fluid*, △ *no coll*, □ *with coll*.
Blue: $\tau_p^+ = 28$, *Black*: $\tau_p^+ = 112$

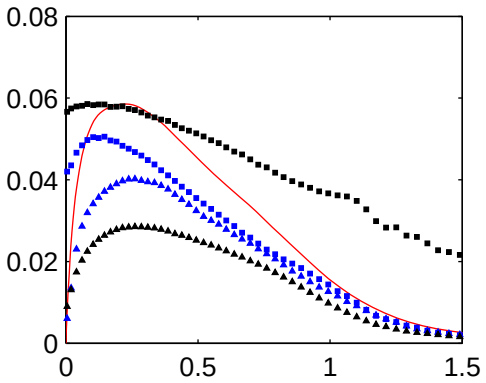

(a) $\overline{x} = 10$

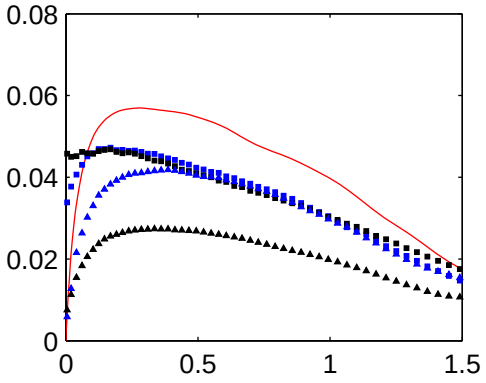

(b) $\overline{x} = 40$

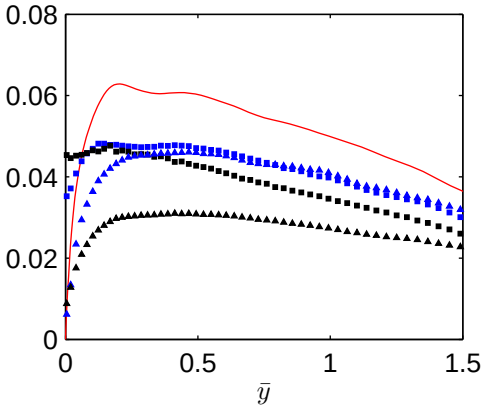

(c) $\overline{x} = 70$

Figure 57. TBL: RMS spanwise velocity without gravity.
— $fluid$, △ $no\ coll$, □ $with\ coll$.
$Blue$: $\tau_p^+ = 28$, $Black$: $\tau_p^+ = 112$

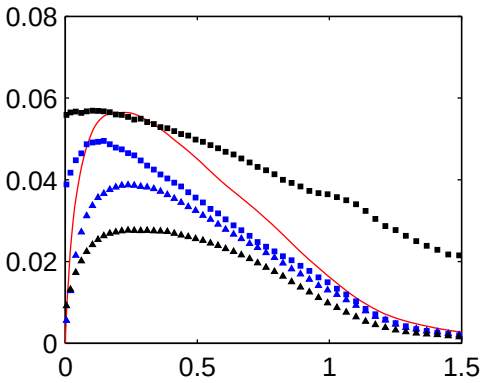

(a) $\overline{x} = 10$

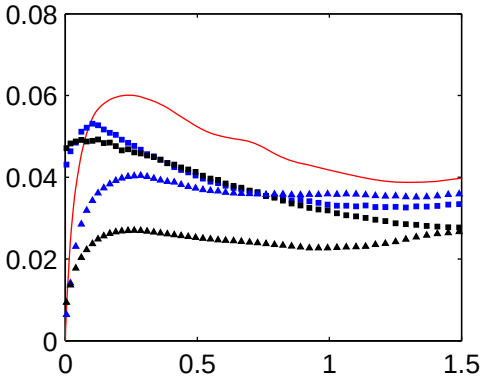

(b) $\overline{x} = 40$

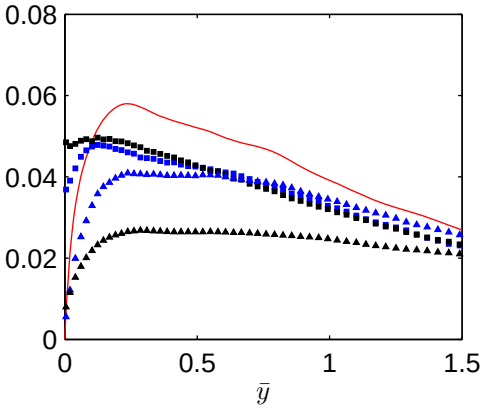

(c) $\overline{x} = 70$

Figure 58. V-TBL: RMS spanwise velocity without gravity.
— $fluid$, △ $no\ coll$, □ $with\ coll$.
$Blue$: $\tau_p^+ = 28$, $Black$: $\tau_p^+ = 112$

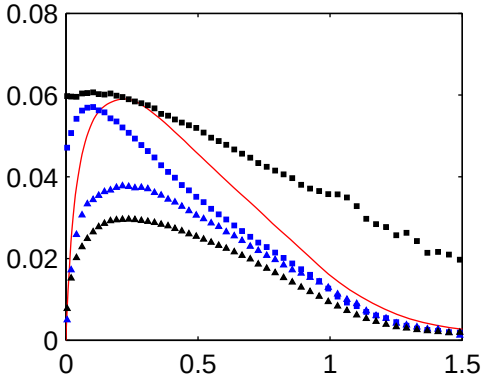

(a) $\overline{x} = 10$

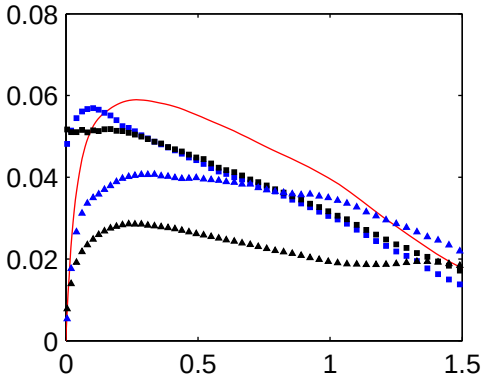

(b) $\overline{x} = 40$

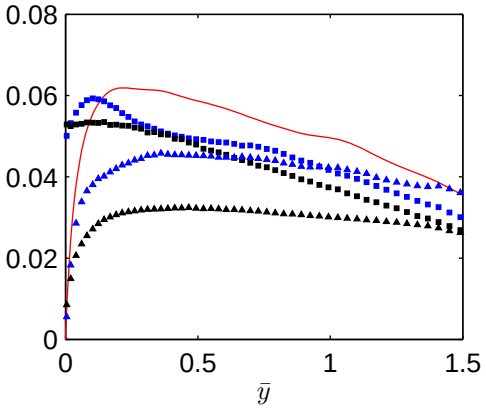

(c) $\overline{x} = 70$

Figure 59. TBL: RMS spanwise velocity with gravity.
— *fluid*, △ *no coll*, □ *with coll*.
Blue: $\tau_p^+ = 28$, *Black*: $\tau_p^+ = 112$

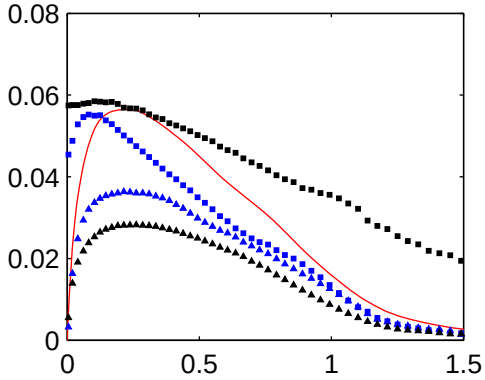

(a) $\overline{x} = 10$

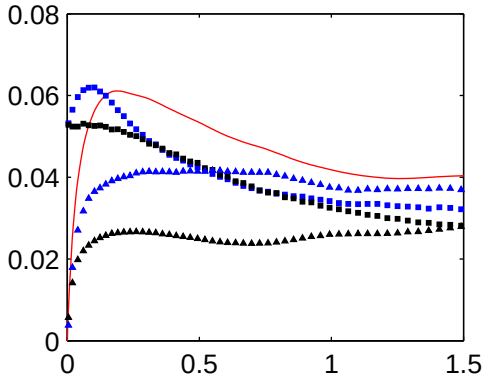

(b) $\overline{x} = 40$

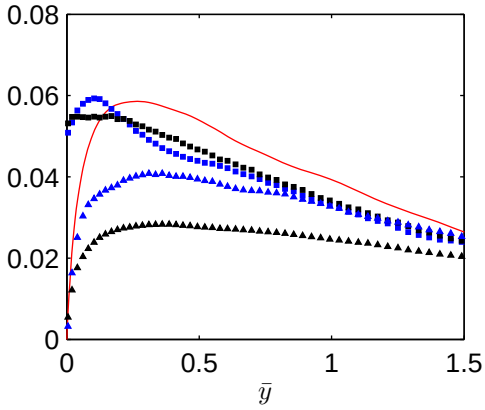

(c) $\overline{x} = 70$

Figure 60. V-TBL: RMS spanwise velocity with gravity.
— *fluid*, △ *no coll*, □ *with coll*.
Blue: $\tau_p^+ = 28$, *Black*: $\tau_p^+ = 112$

Similarly to the fluid, the particles also undergo a reversal to equilibrium conditions as evidenced by Figures (66) and (67). The first set of figures shows the particle Reynolds number without collisions at a variety of wall-normal planes for both flows. At all planes the Re_p increases sharply at $\overline{x} \approx 20$ which is near the point of vortex introduction. The magnitude of the Re_p changes at the different planes as a consequence of the change in the particle relative velocity. The particle relative velocity has a high value near the wall and generally decreases in value away from the wall, however the introduction of the vortex and the subsequent perturbation of the flow field result in a large particle relative velocity. The particles undergo a transition from about, $20 \leq \overline{x} \leq 50$ before reverting to values that are comparable to the flow without the vortex.

Also shown is the streamwise variation of the wall-normal RMS velocity of the fluid and particles at different planes. The behavior is analogous to the particle Reynolds number, however the inclusion of the fluid variation sheds some interesting facts. The fluid is the first to react to the perturbation induced by the vortex, the lighter particles, which tend to follow the fluid more closely are next and finally the denser particles resist the perturbation and take longer to react. The fluid seems to reverse to equilibrium values at around $\overline{x} \approx 45$ with the light particles also reverting to equilibrium at about the same location while the denser particles which are more resistant to changes take longer to reverse to equilibrium conditions. Though not shown, similar plots for cases with particle-particle collisions follow the same trend with some subtle changes to the amplitudes of the curves. Even though the

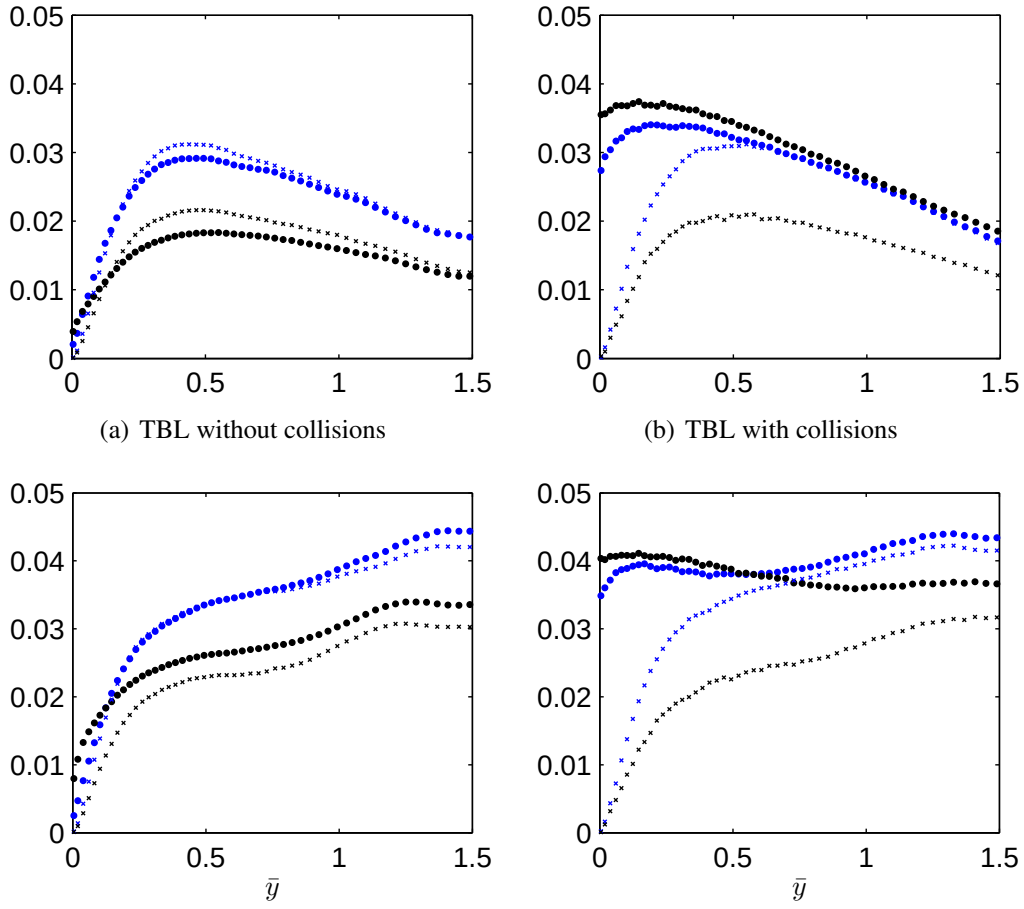

(a) TBL without collisions

(b) TBL with collisions

(c) V-TBL without collisions

(d) V-TBL with collisions

Figure 61. $\langle u_2' v_2' \rangle$ and $\langle v_2' v_2' \rangle$ without gravitational settling, $\overline{x} = 40$.
$\times \langle u_2' v_2' \rangle$, $\circ \langle v_2' v_2' \rangle$.
Blue: $\tau_p^+ = 28$, *Black*: $\tau_p^+ = 112$

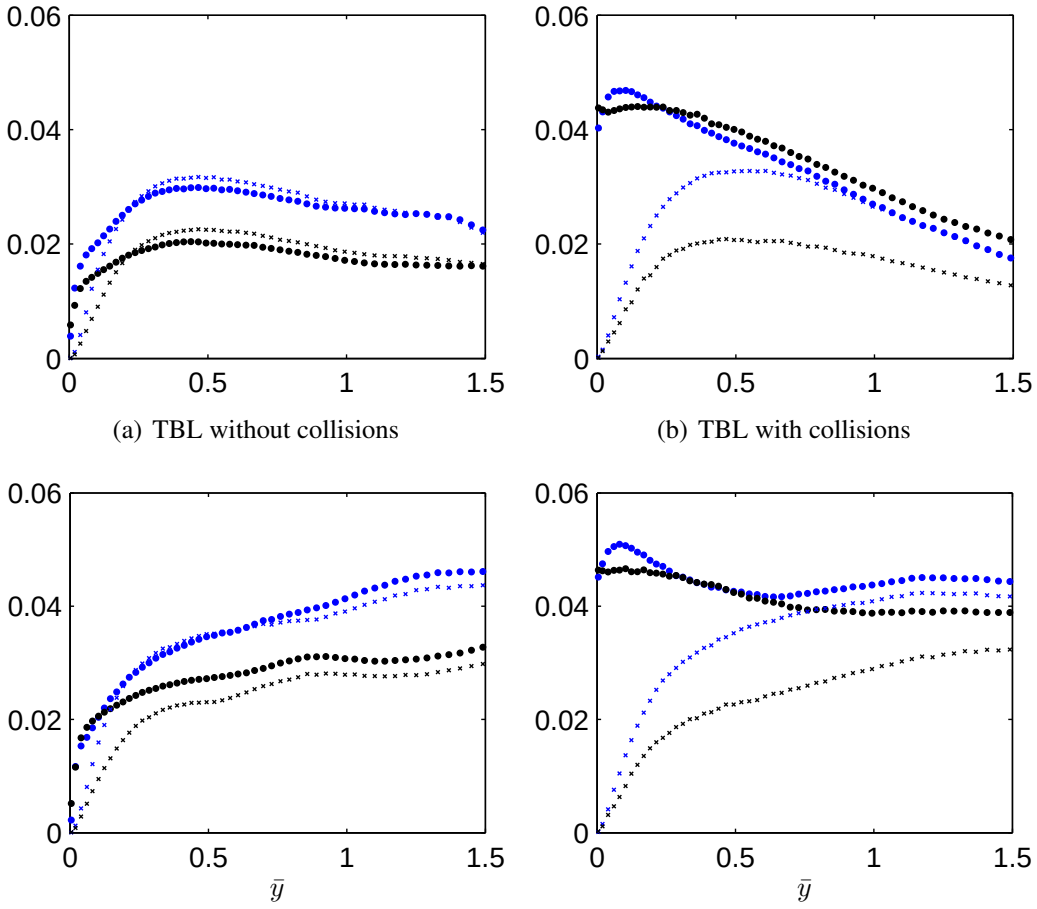

(a) TBL without collisions

(b) TBL with collisions

(c) V-TBL without collisions

(d) V-TBL with collisions

Figure 62. $\langle u_2' v_2' \rangle$ and $\langle v_2' v_2' \rangle$ with gravitational settling, $\overline{x} = 40$.
$\times \langle u_2' v_2' \rangle$, $\circ \langle v_2' v_2' \rangle$.
Blue: $\tau_p^+ = 28$, *Black*: $\tau_p^+ = 112$

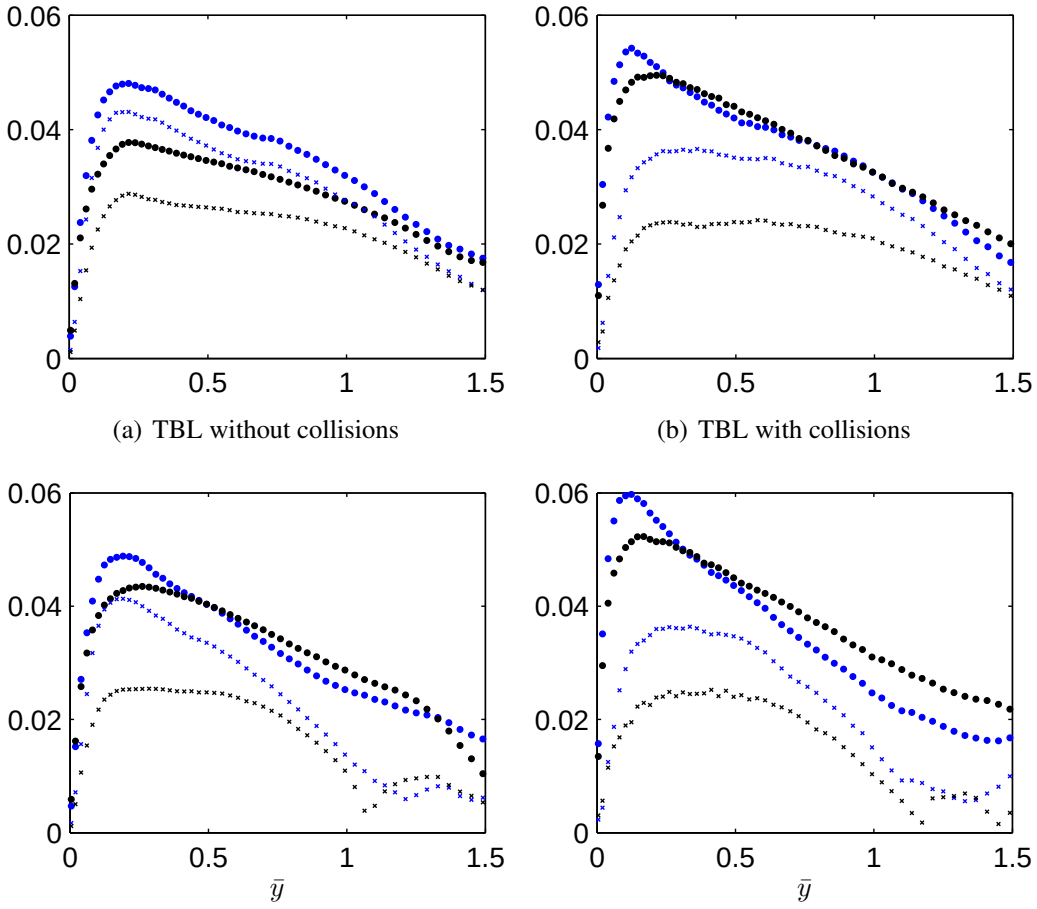

(a) TBL without collisions

(b) TBL with collisions

(c) V-TBL without collisions

(d) V-TBL with collisions

Figure 63. $\langle u_1' v_2' \rangle$ and $\langle v_1' v_2' \rangle$ without gravitational settling, $\overline{x} = 40$.
$\times \langle u_1' v_2' \rangle$, $\circ \langle v_1' v_2' \rangle$.
Blue: $\tau_p^+ = 28$, *Black*: $\tau_p^+ = 112$

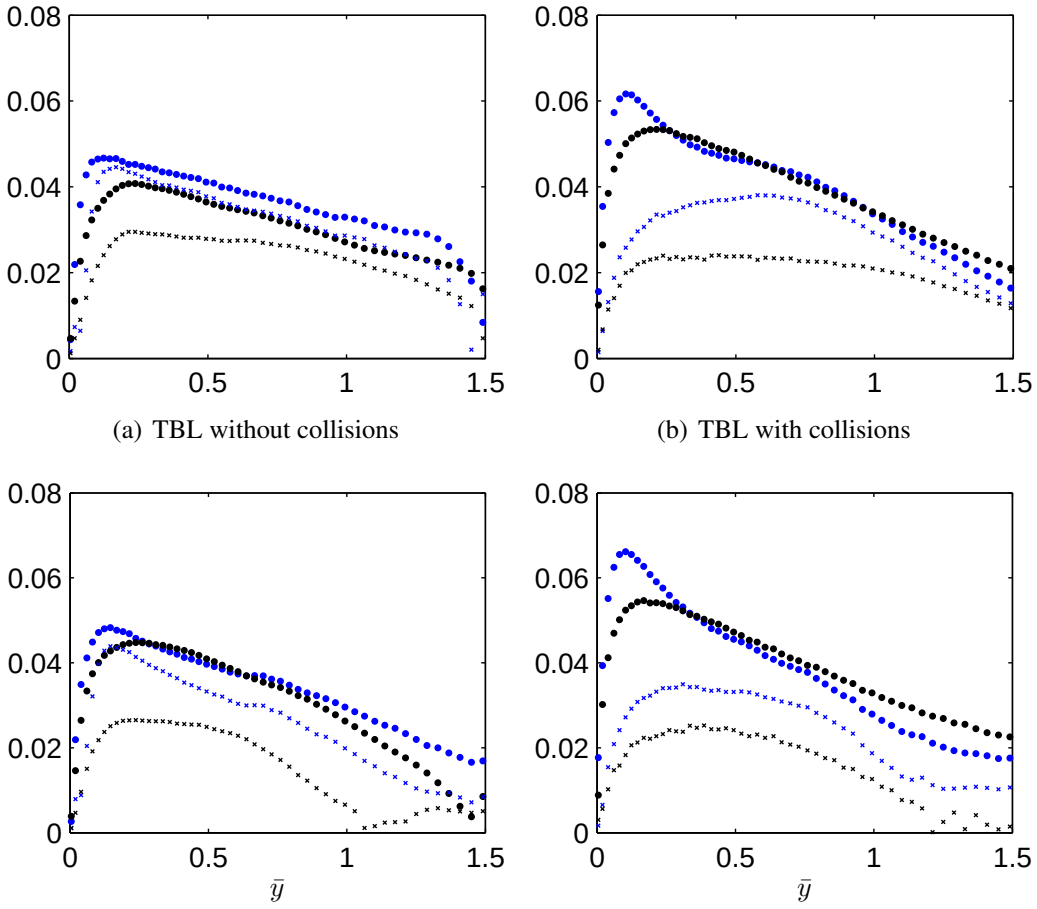

(a) TBL without collisions

(b) TBL with collisions

(c) V-TBL without collisions

(d) V-TBL with collisions

Figure 64. $\langle u_1' v_2' \rangle$ and $\langle v_1' v_2' \rangle$ with gravitational settling, $\overline{x} = 40$.
$\times \langle u_1' v_2' \rangle$, $\circ \langle v_1' v_2' \rangle$.
Blue: $\tau_p^+ = 28$, *Black*: $\tau_p^+ = 112$

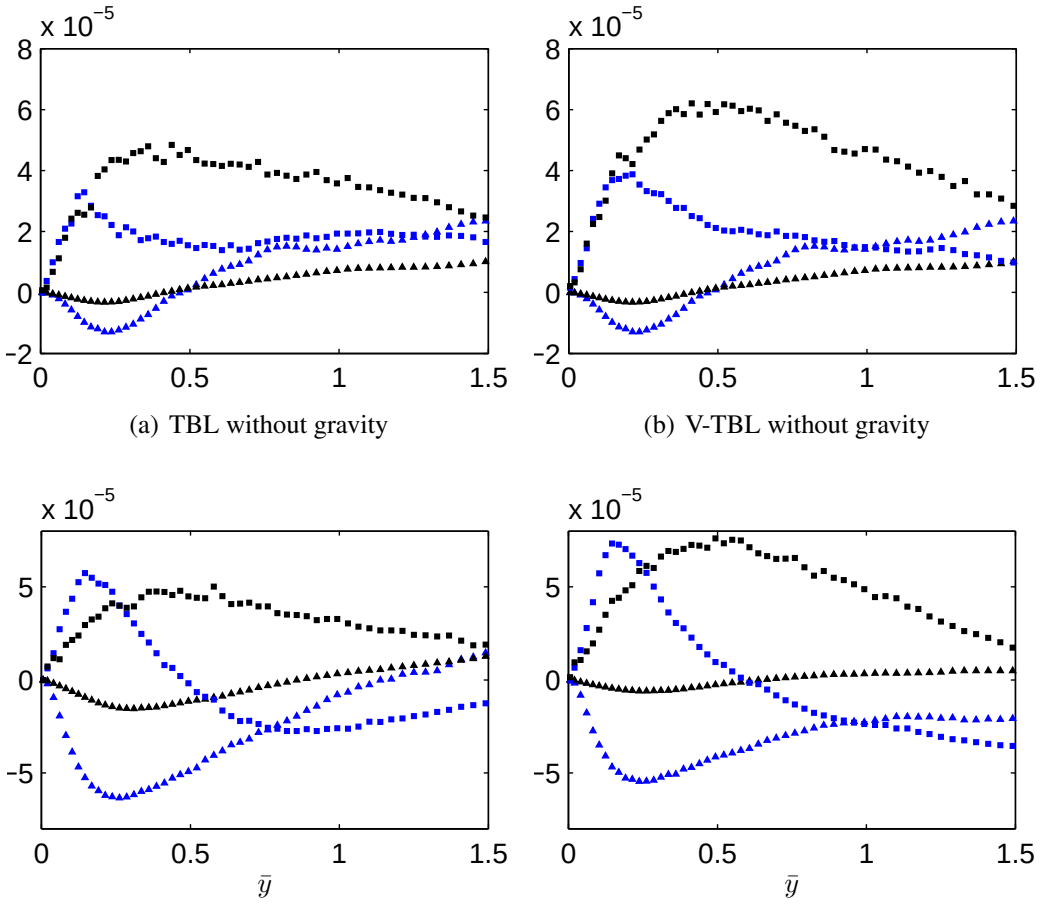

(a) TBL without gravity

(b) V-TBL without gravity

(c) TBL with gravity

(d) V-TBL with gravity

Figure 65. Particle velocity triple correlation $\langle v_2' v_2' v_2' \rangle$, $\overline{x} = 60$.
$\triangle$ *no coll*, $\square$ *with coll*.
Blue: $\tau_p^+ = 28$, *Black*: $\tau_p^+ = 112$

fluid and both particles revert to equilibrium conditions, the return to equilibrium conditions for the particles is sensitive to the particle response time.

In general, the addition of the vortex to the simulations increases particle flux across the wall-normal dimension. The turbulent flow with vortices disperses the particles about twice the distance when compared to the flow without vortices. In addition, the vortex footprint is particularly strong between $25 \leq \overline{y} \leq 50$ and also affects the near wall region as seen on the increased values of the streamwise velocity and the RMS velocity. The effects of inter-particle collisions are strong through the entire domain and not restricted to a specific region of the domain. The effects of collisions are most significant in the near wall region within the boundary layer as seen on the streamwise velocity and the wall-normal and spanwise RMS velocity. The effect of gravity is to increase the particle concentration near the wall and provides more opportunities for collisions with the wall or other particles. Both the inter-particle collisions and the vortex effects are significant but the inter-particle collisions are dominant near the wall while the vortex effects dominate the outer flow particularly in the region where the vortex is introduced.

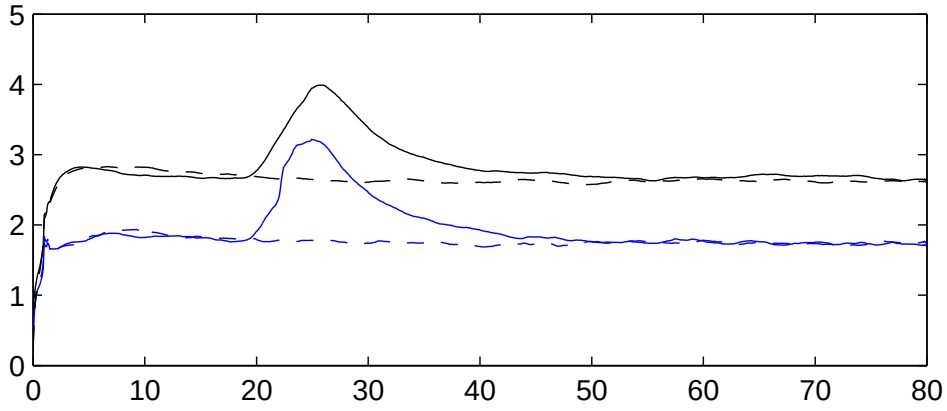

(a) $y^+ \approx 20$

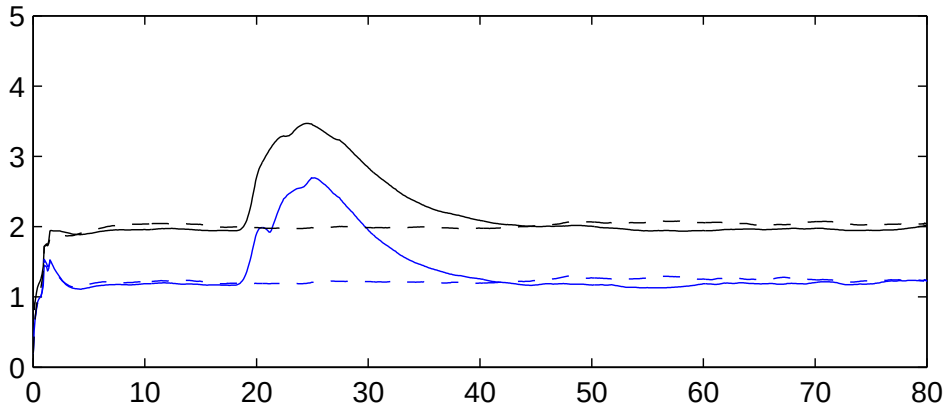

(b) $y^+ \approx 60$

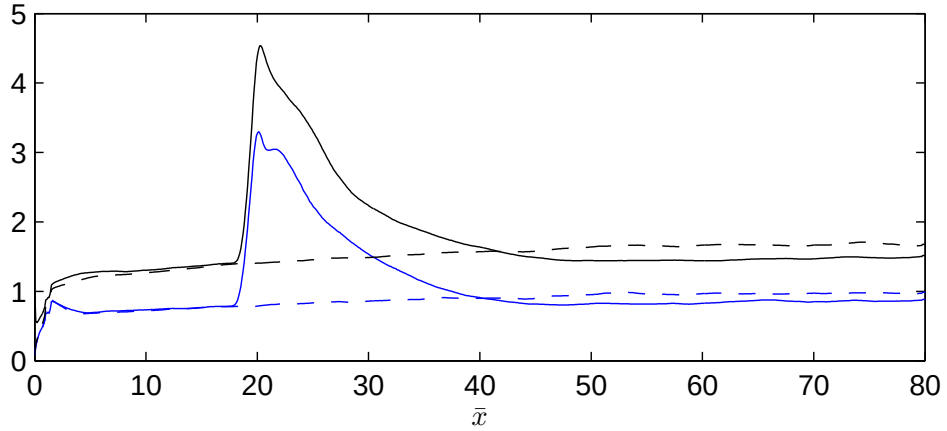

(c) $y^+ \approx 100$

Figure 66. Streamwise variation of particle Reynolds number without collisions.
— V-TBL, - - TBL.
Red: $fluid$, *Blue*: $\tau_p^+ = 28$, *Black*: $\tau_p^+ = 112$

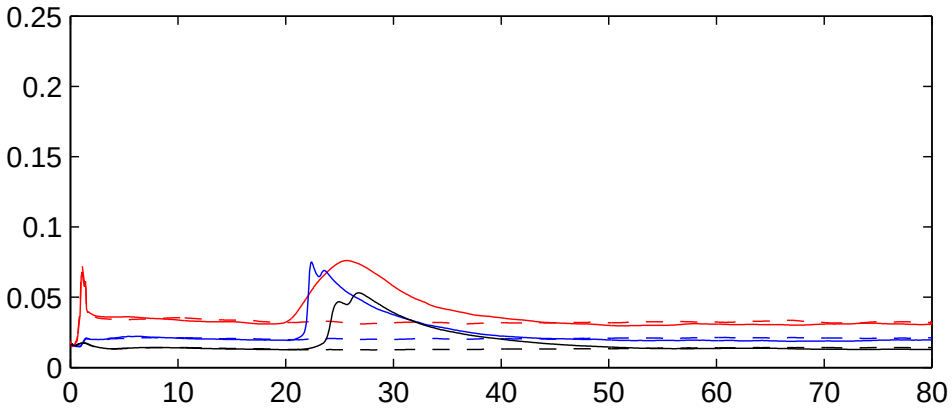

(a) $y^+ \approx 20$

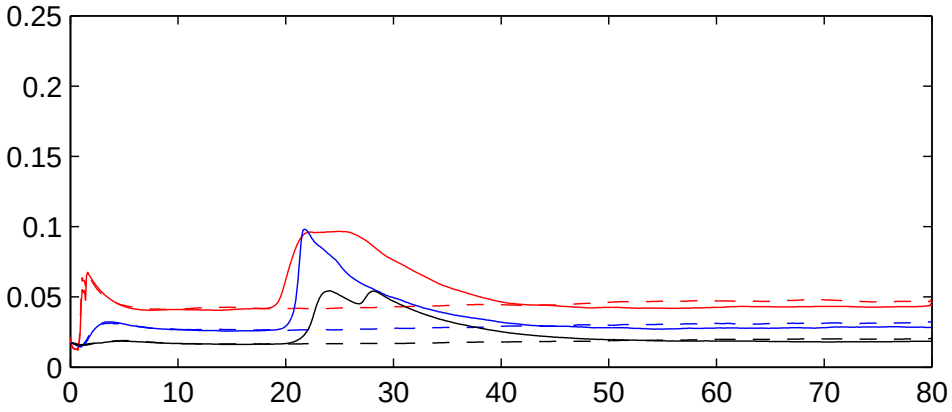

(b) $y^+ \approx 60$

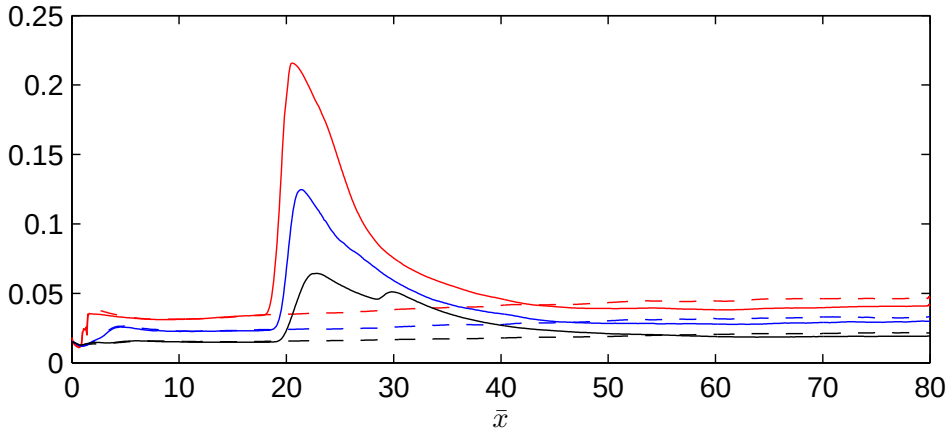

(c) $y^+ \approx 100$

Figure 67. Streamwise variation of wall-normal RMS velocity without collisions.
— V-TBL, - - TBL.
Red: $fluid$, *Blue*: $\tau_p^+ = 28$, *Black*: $\tau_p^+ = 112$

V. Summary

Rotorcraft brownout poses a significant threat to both the personnel operating the aircraft as well as the aircraft. Properly identifying and predicting the evolution of the brownout cloud is complicated due to the abundance of parameters involved. In addition brownout encompasses multiple scales, from the largest which is comparable to the dimensions of the rotorcraft, to the smallest which is comparable to the sediment particle size. This extended range leads to complex effects that influence the processes of entrainment, deposition, and resuspension of the dispersed sediment. Once entrained, sediment particle interactions occur with the coherent wake vortices characterizing the rotor flow, and with the finer scale turbulence generated near the ground. Factors that influence transport characteristics of the resulting two-phase flow include particle-turbulence interactions, particle-particle interactions, and particle interactions with the bed such as entrainment, suspension, and deposition as well as momentum coupling that modifies the carrier flow.

Presently few measurements have been made on full scale rotorcraft, given the complexity of the components, most experiments have been performed on sub-scale rotors. Aside from the measurements, a variety of simulations have also been explored in recent years. The current computational capabilities limit the scope of the simulations and several assumptions become necessary. Assumptions and simplifications in current models that may be dropped as technology evolves and/or knowledge improves include the rotorcraft downwash, momentum exchange between the

two phases, as well as detailed particle entrainment conditions. As the measurements and computing power improves so will the understanding of the boundary conditions on the two-phase flow, specifically regarding the differences between uniform flow and non-uniform flow on particle entrainment.

In order to further the understanding of the fundamental processes that drive the brownout problem, numerical simulations were undertaken. The main effort revolved around numerical simulations to shed light on the near-surface dynamics of particle transport near a sediment bed. The simulations modeled the coherent wake vortices from a rotorcraft interacting with a bed of particles. An Euler-Lagrange approach was employed in which the incompressible Navier-Stokes equations were solved for the gas-phase carrier flow, and a particle equation of motion was solved for each particle in the particulate phase. To segregate contributions of certain aspects of the flow the simulations were carried out with and without streamwise vortices introduced into a turbulent boundary layer. Furthermore, cases with and without particle-particle collisions were also examined to analyze the competing effects between the flow and the particles.

A. Conclusions

The visualizations presented show significant fluid-particle interaction for both particle groups. Even the denser particles are greatly affected by the fluid coherent vortex structures present in the flow. Furthermore the heavier particles are more resistant to the influence of the fluid as seen on the instantaneous particle distribu-

tions. The preferential concentration of particles in regions of low fluid velocity was also an observed effect for simulations without inter-particle collisions. When the particle-particle collisions are allowed the preferential concentration of the particles is reduced dramatically. The number density peaks near the wall for simulations without inter-particle collisions which is a result that has been well documented. The addition of collisions tends to distribute the particles more uniformly across the domain and prevent the collection of very large concentrations near the wall. The addition of gravity forces the particles onto the lower wall increasing the number density for all simulations near the lower wall. The increased number density provides more opportunity for the particles to collide and results in increased RMS and particle-particle values. The inclusion of the vortex disperses the particles further from the wall more effectively populating the computational domain.

The difference between simulations with and without collisions is apparent in the streamwise velocity and the wall-normal and spanwise RMS velocity plots. The streamwise RMS velocity was not significantly affected by the inclusion of inter-particle collisions or gravity. The inclusion of collisions results in a significant increase for both particle groups in both the streamwise velocity and RMS velocity as previously reported in the literature. Furthermore the particle-particle correlations are also sensitive to the effects of collisions. The addition of the vortex, result in interesting effects that are most significant in the outer flow and also in regions close to the vortex introduction location, $25 \leq \overline{x} \leq 50$. The effects of particle-particle collisions are dominant in the near wall region , $0 \leq \overline{y} \leq 1$, while the

vortex efficiently mixes the particles at distances further than one boundary layer thickness from the wall. The inclusion of gravity increases the concentration of particles near the wall which in turn results in more collisions effectively increasing the wall-normal and spanwise RMS velocity as well as the particle correlations. Furthermore at distances away from the vortex introduction, the flow and particles reverse back to an undisturbed state, although the particle return to equilibrium is sensitive to the particle response time.

B. Future Work

There are several areas of the simulation which merit further study. The single phase flow can be improved to more accurately reflect the downwash of the rotorcraft. Rather than just appearing onto the flow, the downwash can be developed to impinge on the ground and develop into a vortex ring that radially expands. Improving the flow solver to account for the evolution from impinging jet to radially expanding vortex is complex and not viable with the current computing capacity. More immediate changes to the flow solver would be to incorporate an LES scheme with an appropriate turbulence model to possibly extend the focus from near-surface interactions to a full two-phase dusty gas simulation that tracks the brownout cloud. Also the current pressure solver utilized in the flow solver is limited to 32 processors due to the distribution of the spanwise grid points. Improvements to the single phase flow will result in more realistic models of rotorcraft downwash and will also bring simulations closer to achieving a full rotorcraft flow

simulation.

The particulate phase would also benefit from advancements to the flow field, since the characterization of the flow by the particles would be more adequate. Nevertheless, the dispersed phase solver also has several areas of possible improvements and additions. The next step for the particulate phase would be the addition of uplift and deposition models, which would control the flux of particles in and out of the lower wall. Currently the dispersed phase simulation does not enforce any type of particle entrainment condition and the particles do not have to overcome some threshold condition for transport. From the measurements on particle entrainment exposed to non-uniform flow adequate boundary conditions can be extracted and enacted on the numerical simulations. Also, currently the lower wall is treated as a smooth wall which can be modified into a rough wall to reflect actual conditions encountered in nature. Aside from physical characteristics of the particles that can be improved, the virtual computation of the dispersed phase can also be improved. The decomposition of the domain for particle computations is currently one-dimensional, however it could potentially be improved to two-dimensional domain decomposition. The modification would not be trivial and issues with load balancing and interfacing between multiple processors would have to be resolved. The modification would allow for more robust parallel computation and even larger particle ensembles that are necessary for a macroscopic brownout simulation.

References

[1] Lee, T. E., Leishman, J. G., and Ramasamy, M., "Fluid Dynamics of Interacting Blade Tip Vortices with a Ground Plane," 64th Annual Forum of the American Helicopter Society, Montreal, Canada, 29 April-1 May, 2008.

[2] Chien, N. and Wan, Z., *Mechanics of Sediment Transport*, American Society of Civil Engineers Press, 1801 Alexander Bell Dr. Reston, VA 20191-4400, 1999.

[3] Johnson, B., *Mechanisms of Sediment Entrainment and Transport in Rotorcraft Brownout*, Master's thesis, University of Maryland, 2009.

[4] Sabbagh, L., "Flying Blind in Iraq: U.S. Helicopters Navigate Real Desert Storms," Popular Mechanics, October 3, 2006.

[5] Leishman, J. G., "Rotorcraft Brownout: Advanced Understanding, Control, and Mitigation," Progress Report for AFOSR Grant FA9550-08-1-0406, University of Maryland, College Park, MD 20742-2115, 2008.

[6] Wadcock, A. J., Solis, E., Potsdam, M., Ewing, L. A., and Rajagopalan, G., "Rotorcraft Downwash Flow Field Study to Understand the Aerodynamics of Helicopter Brownout," American Helicopter Society Southwest Region Technical Specialists' Meeting, Grapevine, TX, 15-17 October, 2010.

[7] Johnson, B., Leishman, J. G., and Sydney, A., "Investigation of Sediment Entrainment in Brownout Using High-Speed Particle Image Velocimetry," 65th Annual Forum of the American Helicopter Society, Grapevine, TX, 27-29 May, 2009.

[8] Nathan, N. D. and Green, R. B., "Measurements of a Rotor Flow in Ground Effect and Visualization of the Brownout Phenomenon," 64th Annual Forum of the American Helicopter Society, Montreal, Canada, 29 April-1 May, 2008.

[9] Haehnel, R. B., Moulton, M. A., Wenren, W., and Steinhoff, J., "A Model to Simulate Rotorcraft Induced Brownout," 64th Annual Forum of the American Helicopter Society, Montreal, Canada, 29 April-1 May, 2008.

[10] Phillips, C. and Brown, R. E., "Eulerian Simulation of the Fluid Dynamics of Helicopter Brownout," 64th Annual Forum of the American Helicopter Society, Montreal, Canada, 29 April-1 May, 2008.

[11] Phillips, C., Kim, H. W., and Brown, R. E., "The Flow Physics of Helicopter Brownout," 66th Annual Forum of the American Helicopter Society, Phoenix, AZ, 11-13 May, 2010.

[12] Squires, K. D. and Eaton, J. K., "Particle response and turbulence modification in isotropic turbulence," *Physics of Fluids A*, Vol. 2, 1990, pp. 1191–1203.

[13] Rouson, D. W. I. and Eaton, J. K., "On the preferential conentration of solid particles in turbulent channel flow," *Journal of Fluid Mechanics*, Vol. 428, 2001, pp. 149–169.

[14] Marchioli, C. and Soldati, A., "Mechanisms for particle transfer and segregation in a turbulent boundary layer," *Journal of Fluid Mechanics*, Vol. 468, 2002, pp. 283–315.

[15] Picciotto, M., Marchioli, C., and Soldati, A., "Characterization of near-wall accumulation regions for inertial particles in turbulent boundary layers," *Physics of Fluids*, Vol. 17, 2005, pp. 098101.

[16] Fessler, J. R., Kulick, J. D., and Eaton, J. K., "Preferential concentration of heavy particles in a turbulent channel flow," *Physics of Fluids*, Vol. 6, 1994, pp. 3742–3749.

[17] Vance, M. W., Squires, K. D., and Simonin, O., "Properties of the particle velocity field in gas-solid turbulent channel flow," 5th International Conference on Multiphase Flow, 2004.

[18] Yamamoto, Y., Pothoff, M., Tanaka, T., Kajishima, T., and Tsuji, Y., "Large eddy simulation of turbulent gas-particle flow in a vertical channel: effect of considering inter-particle collisions," *Journal of Fluid Mechanics*, Vol. 442, 2001, pp. 303–334.

[19] Sommerfeld, M., "Analysis of collision effects for a turbulent gas-particle flow in a horizontal channel: Part i. particle transport," *International Journal of Multiphase Flow*, Vol. 29, 2003, pp. 675–699.

[20] Syal, M., Govindarajan, B., and Leishman, J. G., "Mesoscale Sediment Tracking Methodology to Analyze Brownout Cloud Developments," 66th Annual Forum of the American Helicopter Society, Phoenix, AZ, 11-13 May, 2010.

[21] Wachspress, D. A., Whitehouse, G. R., Keller, J. D., Yu, K., Gilmore, P., Dorsett, M., and McClure, K., "A High Fidelity Brownout Model for Real-Time Flight Simulations and Trainers," 65th Annual Forum of the American Helicopter Society, Grapevine, TX, 27-29 May, 2009.

[22] D'Andrea, A., "Numerical Analysis of Unsteady Vortical Flows Generated by a Rotorcraft Operating on Ground: A First Assessment of Helicopter Brownout," 65th Annual Forum of the American Helicopter Society, Grapevine, TX, 27-29 May, 2009.

[23] Naqavi, I. Z. and Piomelli, U., "Large Eddy Simulation of Boundary Layers with Embedded Spanwise Vortices," *International Journal of Computational Fluid Dynamics*, Vol. 24, 2010, pp. 467–477.

[24] Bagnold, R. A., *The Physics of Blown Sand and Desert Dunes*, Chapman and Hall Ltd, 11 New Fetter Lane, London EC4P 4EE, 1973.

[25] Gyr, A. and Hoyer, K., *Sediment Transport a Geophysical Phenomenon*, Springer., P.O. Box 17, 3300 AA Dordrecht, The Netherlands, 2006.

[26] Hutter, K., "Geophysical granular and particle-laden flows: review of the field," *Philosophical Transactions of the Royal Society A*, Vol. 363, 2005, pp. 1497–1505.

[27] Saffman, P. G., "The Lift on a Small Sphere in a Shear Flow," *Journal of Fluid Mechanics*, Vol. 22, 1965, pp. 385–400.

[28] Wang, Q., Squires, K. D., Chen, M., and McLaughlin, J. B., "On the Role of the Lift Force in Turbulence Simulations of Particle Deposition," *International Journal of Multiphase Flow*, Vol. 23, 1997, pp. 749–763.

[29] Kaftori, D., Hetsroni, G., and Benerjee, S., "Particle Behavior in the Turbulent Boundary Layer. I. Motion, Deposition, and Entrainment," *Physics of Fluids*, Vol. 7, 1995, pp. 1095–1106.

[30] Nino, Y. and Garcia, M. H., "Experiments on Particle-Turbulent Interactions in the Near Wall Region of an Open Channel Flow: Implications for Sediment Transport," *Journal of Fluid Mechanics*, Vol. 326, 1996, pp. 285–319.

[31] Rashidi, M., Hetsroni, G., and Benerjee, S., "Particle-Turbulence Interaction in a Boundary Layer," *International Journal of Multiphase Flow*, Vol. 16, 1990, pp. 935–949.

[32] Sumer, B. M. and Oguz, B., "Particle Motions Near the Bottom in Turbulent Flwo in an Open Channel," *Journal of Fluid Mechanics*, Vol. 86, 1978, pp. 109–127.

[33] Sutherland, A., "Proposed Mechanism for Sediment Entrainment by Turbulent Flows," *Journal of Geophysical Research*, Vol. 72, 1967, pp. 191–198.

[34] Williams, J. J., Butterfield, G. R., and Clark, D. G., "Aerodynamic Entrainment Threshold: Effects of Boundary Layer Flow Conditions," *Sedimentology*, Vol. 41, 1994, pp. 309–328.

[35] van Rijn, L. C., "Sediment Transport, Part II: Suspended Load Transport," *Journal of Hydraulic Engineering*, Vol. 110, 1984, pp. 1613–1641.

[36] Nino, Y., Lopez, F., and Garcia, M., "Threshold for Particle Entrainment into Suspension," *Sedimentology*, Vol. 50, 2003, pp. 247–263.

[37] Haehnel, R. and Dade, W. B., "Physics of Particle Entrainment Under the Influence of an Impinging Jet," Army Science Conference, Orlando, FL, 1-4 December, 2008.

[38] Haehnel, R. and Dade, W. B., "Particle Entrainment by Non-Uniform Eolian Flow," Army Science Conference, Orlando, FL, 1-4 December, 2010.

[39] Mulinti, R. and Kiger, K., "Two-Phase PIV Measurements of Particle Suspension in a Forced Impinging Jet," 63rd Annual Meeting of the APS Division of Fluid Dynamics, Long Beach, CA, 21-23 November, 2010.

[40] Geiser, J. and Kiger, K., "A Simplified Analog for a Rotorcraft-in-Ground-Effect Flow Using a Forced Impinging Jet," 63rd Annual Meeting of the APS Division of Fluid Dynamics, Long Beach, CA, 21-23 November, 2010.

[41] Panton, R. L., *Incompressible Flow*, John Wiley and Sons Inc., Hoboken, New Jersey, 3rd ed., 2005.

[42] Lund, T. S., Wu, X., and Squires, K. D., "Generation of Inflow Data for Spatially Developing Boundary Layer Simulations," *Journal of Computational Physics*, Vol. 140, 1998, pp. 233–258.

[43] Orlanski, I., "A Simple Boundary Condition for Unbounded Hyperbolic Flows," *Journal of Computational Physics*, Vol. 21, 1976, pp. 251–269.

[44] Fadlun, E. A., Verzicco, R., Orlandi, P., and Mohd-Yudof, J., "Combined Immersed-Boundary Finite-Difference Methods for Three-Dimensional Complex Flow Simulations," *Journal of Computational Physics*, Vol. 161, 2000, pp. 35–60.

[45] Maxey, M. R. and Riley, J. J., "Equation of motion for a small rigid sphere in a nonuniform flow," *Physics of Fluids*, Vol. 26, 1983, pp. 883–889.

[46] Schiller, L. and Nauman, A., "A drag coefficient correlation," *Z. Ver. Deutsch. Ing.*, Vol. 77, 1935, pp. 318–320.

[47] Cheng, N., "A simplified settling velocity formula for sediment particle," *Journal of Hydraulic Engineering*, Vol. 123, 1997, pp. 149–152.

[48] MPI Forum, *MPI: A Message-Passing Interface Standard*, 2009.

[49] Vance, M. W., *On the Effects of Inter-Particle Collisions in Turbulent Channel Flow*, Ph.D. thesis, Arizona State University, 2008.

[50] Fevrier, P., Simonin, O., and Squires, K. D., "Partitioning of Particle Velocities in Gas-Solid Turbulent Flows into a Continuous Field and a Spatially Uncorrelated Random Distribution: Theoretical Formalism and Numerical Study," *Journal of Fluid Mechanics*, Vol. 533, 2005, pp. 1–46.

[51] Eaton, J. K. and Fessler, J. R., "Preferential Concentration of Particles by Turbulence," *International Journal of Multiphase Flow*, Vol. 20, 1994, pp. 169–209.

[52] Li, Y., McLaughlin, J. B., Kontomaris, K., and Portela, L., "Numerical simulation of particle-laden turbulent channel flow," *Physics of Fluids*, Vol. 13, 2001, pp. 2957–2967.